2013-05-28

An Investigation on the Production of Water-Stable, Porous Metal-Organic Materials

Reid, Margaret Elizabeth

UNIVERSITY OF CALGARY

An Investigation on the Production of Water-Stable, Porous Metal-Organic Materials

by

Margaret Elizabeth Reid

A THESIS

SUBMITTED TO THE FACULTY OF GRADUATE STUDIES

IN PARTIAL FULFILMENT OF THE REQUIREMENTS FOR THE

DEGREE OF MASTER OF SCIENCE

DEPARTMENT OF CHEMISTRY

CALGARY, ALBERTA

MAY 2013

Abstract

Two mechanisms of increasing the water and structural stability of metal-organic frameworks (MOFs) were investigated. Two carboxylate MOFs, Mg-MOF-74 and HKUST-1, were post-synthetically modified with silica to increase structural stability while retaining the originally high zero-loading heats of adsorption, 65.4 kJ/mol and 32.2 kJ/mol, respectively. The modified materials were characterized by NMR, IR, SEM/EDX, PXRD, TGA, and adsorption of CO_2 and N_2. The silicated HKUST-1 showed remarkably high water stability, whereas the silicated Mg-MOF-74 did not. A second approach to stability was investigated using a novel phosphonate ligand, 2,7-bis(ethylphosphono)fluorene, yielding hollow microspheres upon hydrothermal reaction with cobalt (II) nitrate. The microspheres were thermally stable to $450^{o}C$, and were stable to sonication in water. The mechanism of formation, structure and chemical stability were investigated and will be discussed.

Dedication

To my Family

Table of Contents

List of Tables

List of Figures and Illustrations

List of Symbols, Abbreviations and Nomenclature

Symbol	Definition
BDC	1,4-benzenedicarboxylate
BET	Brunauer-Emmett Teller model
BTC	1,3,5-benzenetricarboxylate
CALF	Calgary Framework
CALF-B	Calgary Framework Ball
DMSO	Dimethylsulfoxide
DOBDC	1,4-dioxo-2,5-benzenedicarboxylate
DSC	Differential scanning calorimetry
EA	Elemental Analysis
EDX	Energy-dispersive X-ray spectroscopy
Et_2H_2BPF	2,7-bis(ethylphosphono)fluorene
Et_4BPF	2,7-bis(diethylphosphono)fluorene
H_4BPF	2,7-bisphosphonofluorene
HKUST-1	$Cu_3(BTC)_2$
HOA	Heat of adsorption
IR	Infra-red
MCM-41	A mesoporous silica
Mg-MOF-74	$Mg_2(dobdc)$
MOF	Metal-organic framework
MOP	Metal-organic polyhedra
NMR	Nuclear magnetic resonance
PSM	Post-synthetic modification
PXRD	Powder x-ray diffraction
$-Q_{st}$	Zero-coverage heat of adsorption
RH	Relative humidity
SBU	Secondary Building Unit
SEM	Scanning electron microscopy
TEA	Triethylamine
TEOS	Tetraethyl orthosilicate
TGA	Thermogravimetric analysis
THF	Tetrahydrofuran
TMOS	Tetramethyl orthosilicate
TMP	Trimethyl phosphate
UV-Vis	Ultraviolet-visible
ZIF	Zeolitic Imidazolate Framework
ZIF-8	$Zn(2-methylimidazolate)_2$
DMF	Dimethylformamide
DNA	Deoxyribonucleic acid
MOF-5	$Zn_4O(BDC)_3$

MOF-177 $Zn_4O(1,3,5\text{-benzenetribenzoate})_2$
MOF-210 $Zn_4O(4,4',4''\text{-[benzene-1,3,5- triyl-tris(ethyne-2,1-diyl)]tribenzoate})_{4/3}(\text{biphenyl-4,4'-dicarboxylate})$

Chapter One: **Introduction**

1.1 Supramolecular Chemistry

Supramolecular chemistry is a necessary tool for the creation of complex materials. This class of chemistry revolves around the use of favoured states to form an ordered material from self-assembled reagents. Often the term "self-assembly" draws biological connotations, due to the specificity of many biological molecules and processes. Deoxyribonucleic acid (DNA), the backbone controlling all complex organisms, is a classic example of a supramolecular material. DNA has a highly ordered structure, composed of four different nucleosides which complement each other through hydrogen bonds. These hydrogen bonds also allow DNA to be a reversible structure in which the strands can be separated to copy the information onto a new DNA strand. The replication process is coupled with an error-checking ability to minimize defects. The information coded in DNA uniquely allows it to dictate information to its surroundings, making it a highly functional material. These four main properties, order, reversibility, error-checking and function, are embodied by supramolecules both inside and outside of biological systems. Supramolecular chemistry requires materials to be highly reversible in nature in order to result in highly ordered structures. Hydrogen-bonded networks and polymers are thus classically discussed materials with respect to supramolecularity. If proper conditions are used, however, supramolecular materials can be made with coordination bonds. Solubility and temperature controls are both ways in which material with stronger bonds can be made reversible. Once formed in equilibrium, these architectures are extremely thermodynamically stable and can be used for their unique functionality.

1.2 Self Assembly of Discrete Molecules

Discrete hollow metal-organic clusters, molecular cages, and capsules can be formed through self assembly and have been used to image proteins, as catalytic vessels, and as specific recognition sites. These materials have a wide array of assembly-specific functionality due to the reversible nature of the material in synthesis, as well as the range of shapes and sizes of assemblies that can be designed. Discrete ordered architectures are possible through careful choice of metals and ligands. An excellent example of this is illustrated by a series of discrete capsules formed by Fujita and coworkers.[1–4] These clusters were formed using a variety of different ligands, such as (**1**) 2,4,6-tri(pyridin-4-yl)-1,3,5-triazine, (**2**) 2,4,6-tri(pyridin-3-yl)-1,3,5-triazine, and (**3**) 2,4-di(pyridin-3-yl)-6-(pyrimidin-5-yl)-1,3,5-triazine, pictured below in Figure 1.1. Ligands (**1**), (**2**), and (**3**) were reacted with a capped square-planar palladium (II) starting material to yield a capsule with (**1**), a bowl with (**2**), and either a capsule or a bowl with (**3**). The choice of metal allowed for selective binding with a L-M-L angle of 90° that targets specific square, capsule and "bowl" morphologies.
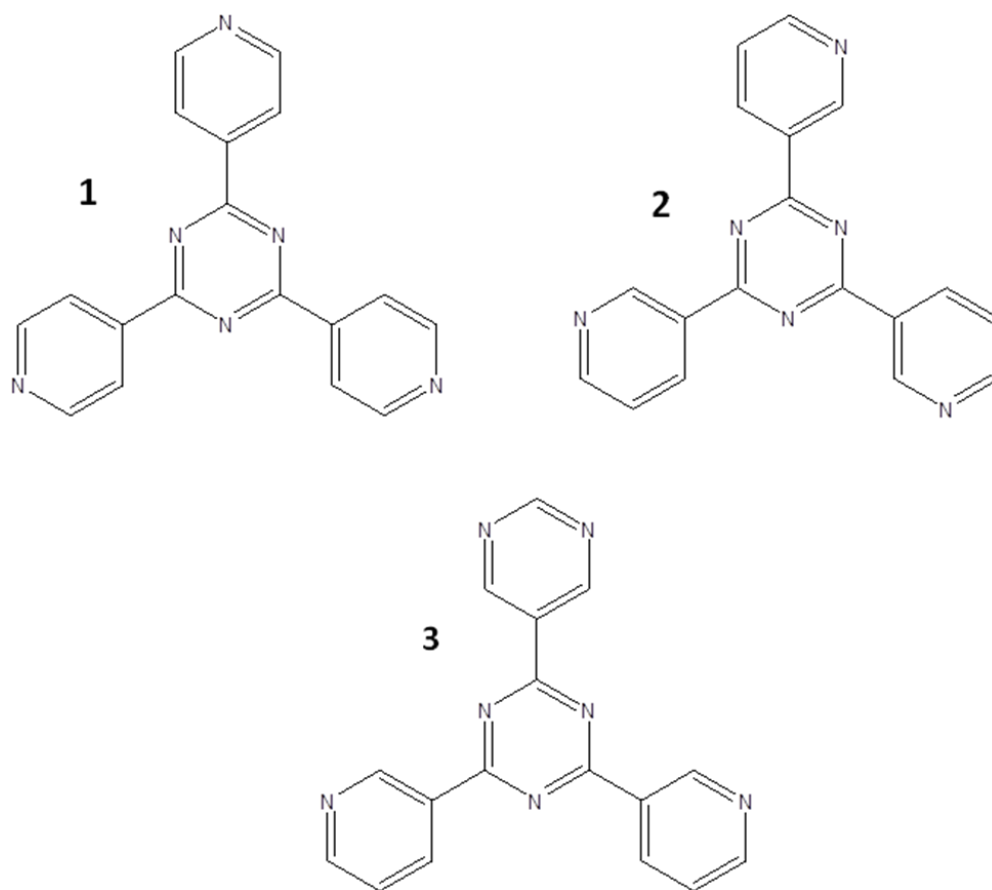
Figure 1.1. Ligands (1), (2), and (3), used in the formation of different cage and bowl structures.[1]

The ligands used in this example also direct the dimensionality of the resulting products, ranging from a flat, 2D square complex formed by linear linkers, to a variety of 3D cages that are capable of incorporating substrates. The guest molecules present in these examples can also influence the thermodynamically favoured structure.[1] In the case of ligand (**3**), two different structures are possible with the same metal to ligand ratio, a larger open bowl structure and a smaller capsule. The open bowl was favoured in the presence of larger guests, while the capsule was favoured in the presence of smaller guests. This property is indicative that the presence of the guests influences the thermodynamic stability of the system.

1.3 Self-Assembly of Frameworks

Three-dimensional architectures can be formed using the same principles of supramolecular chemistry. Metal-organic frameworks (MOFs) are a class of extended porous materials composed of metal clusters joined by robust multitopic organic ligands. A wide variety of both metals and multitopic ligands can be used. One of the main synthetic advantages of these materials is that they are able to form infinite networks in one, two and three dimensions, producing ordered materials that can easily be characterized by x-ray diffraction. Carboxylates are most commonly used as ligands; however, phosphonates, azolates and sulfonates and combinations thereof have also been used in the past.[5–8] Structural possibilities are endless with the number of potential metal-ligand combinations.

Structurally, one of the differences between MOFs and discrete clusters is the possibility of three-dimensional connectivity through both the ligand and the metal centre. The capsules described above involve a capped metal with a terminal ligand, with a multitopic linker. On the other hand, the metals and linkers in MOFs are selected such that their connectivities can be infinitely repeated. A theoretical example of this would be a metal cluster with an overall octahedral structure, which can be linearly connected to other metal clusters via linear ditopic ligands. MOF-5 is a well-known microporous MOF composed of a zinc (II) oxide cluster, connected by 1,4-benzenedicarboxylate (BDC).[9] The overall formula for MOF-5 is $Zn_4O(BDC)_3$.

1.4 Factors Influencing MOF Synthesis

The metal clusters within MOFs can be thought of as vertices in a net, while the ligands of varying connectivity can be thought of as either edges, or edges with vertices, depending on whether the ligand extends in one or two dimensions. The common metal clusters are commonly known as secondary building units (SBUs), and can be classified into the number of connecting sites each offers. The analysis of common SBUs is a large prediction tool within the MOF community, and is used for reticular synthesis. Reticular synthesis is the act of predicting new MOF structures by connecting known SBUs through different ligands to obtain different theoretical net structures. This tool is often used in conjunction with ligands for which the coordination modes are well-known and predictable, such as carboxylate ligands. This is, however, a very rudimentary tool, as multiple metal clusters are sometimes possible within a given system. With MOF synthesis, solubility of the starting materials and temperature of the synthesis are large determining factors in the resulting product, yet careful control may still yield mixed phases depending on the favourability of the desired product.

MOFs are very versatile due to the infinite number of available combinations of metals and ligands. The metals and ligands present can dictate the type of framework, size of pores, and pore shape, among other properties. There are many potential applications of MOFs due the wide range of MOF structures that can be made. Potential applications include gas storage and separation, proton conduction, catalysis, drug delivery, and molecular separation.

1.5 Porosity

Arguably, the most characteristic property of MOFs is their porosity. Porosity in terms of MOF chemistry is defined as an opening that is accessible from more than one face of the

material, and that remains when solvent is removed or evacuated. The diameter of the pores can be divided into three different classes: micropores (< 2 nm), mesopores ($2 - 50$ nm), and macropores (> 50 nm). The size of the pore can play a large role in the function of a given MOF. For example, size selectivity can allow certain molecules to pass through a pore, yet exclude larger molecules. The pore size also plays a smaller role in the available surface area and functional sites per amount of material. Pores that span in two or three dimensions are more accessible than one-dimensional pores, due to the orientation-related blocking effects. Upon decomposition, one-dimensional pores tend to lose accessible surface more quickly than pores with greater dimensionality due to complete pore blocking upon decomposition. These factors can be important in many applications of MOFs.

1.6 Surface Area

Another important feature of MOFs is their high accessible surface, holding records that surpass those of other porous materials, including zeolites and mesoporous silicas. One MOF known for its high surface area of 1800 m^2/g and accessible metal centres is Mg_2(1,4-dioxido-2,5-benzenedicarboxylate) (Mg-MOF-74),[10] a material that will be further examined in the second chapter.   The record for greatest surface area has been increasing at a rapid rate with new activation techniques, such as the use of supercritical CO_2. This technique removes adsorbed solvent without the drastic changes in temperature that lead to particle agglomeration and pore blocking.[11] Another factor in the rapid increase of high-surface area MOFs in the literature also stems from reticular synthesis and enhanced ligand design. Reticular synthesis can be coupled with ligand design to predict and subsequently create new high surface area MOFs. For example, the act of replacing aryl linkers with acetylene linkers was first reported by Furukawa

and coworkers.[12] A series of new MOFs were based off the ligand design of MOF-177, $Zn_4O(1,3,5$-benzenetribenzoate$)_2$, with the already high surface area of 4 500 m^{2}g^{-1}.[13] The new linkers employed lead to MOF-210, $Zn_4O(4,4',4''$-[benzene-1,3,5- triyl-tris(ethyne-2,1-diyl)]tribenzoate$)_{4/3}$(biphenyl-4,4'-dicarboxylate), which has a reported BET surface area of 6 420 m^{2}g^{-1}.[12]

1.7 Coordination Interactions in MOFs

The metal clusters found within MOFs offer a unique site of reactivity that is not found in other porous materials. Unlike other high surface area porous materials, such as zeolites, mesoporous silicas and activated carbons, MOFs are held together with coordination bonds. The coordination bonds in MOFs offer a highly polarizing surface with which an adsorbate can interact. The metal clusters in a MOF are very important towards the resulting MOF structure and the chemical properties of the MOF.

1.7.1 Nature of the Metal

In terms of structure, metal valence can play a large role in the metal ligand bond. In phosphonate MOFs, for example, the metal itself can make a large difference in MOF crystallinity and structural stability. With increasing charge on the metal, the binding strength increases and thus the reversibility of the interaction decreases. This plays a large role in the process of crystallization.[14, 15]
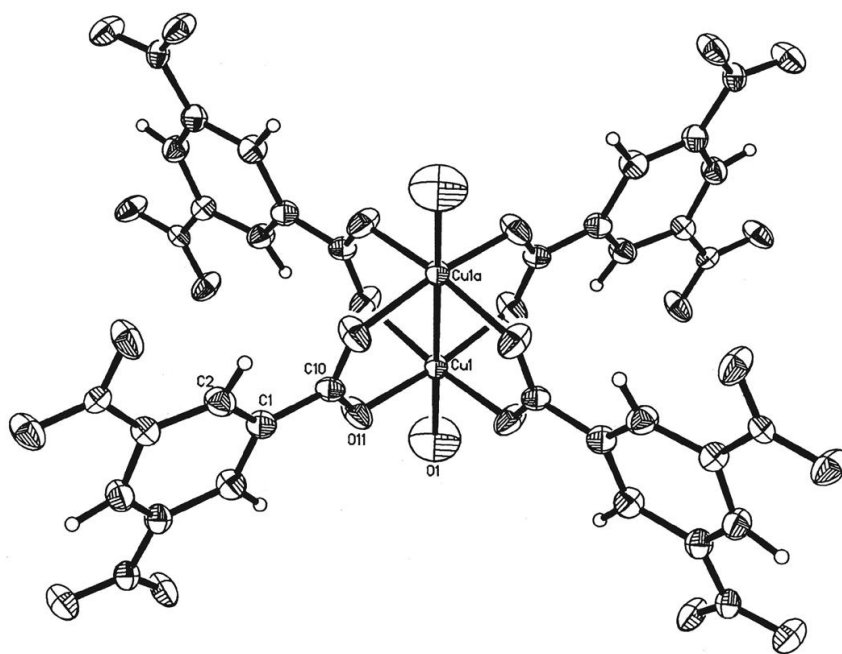
Figure 1.2. SBU of HKUST-1, showing copper-paddlewheel structure. From (Chui, S. S.-Y.; Lo, S. M.-F.; Charmant, J. P. H.; Orpen, A. G.; Williams, I. D. Science 1999, *283*, 5405, 1148-1150). Reprinted with permission from AAAS.[16]

Specific metals can also induce characteristic clusters, such as the copper paddlewheel SBU which is a key structural component of Cu_2(1,3,5-benzenetricarboxylate, BTC)$_3$, a MOF commonly known as HKUST-1 that will be discussed further in the second chapter. The valence of the metals used can also dictate interactions with non-ligand materials. For example, the increased M-L bond strength induced by M^{III} and M^{IV} metals reduces the ability of water to break apart the framework once formed.[17]

1.7.2 Nature of the Ligand

MOF stability to water is also greatly influenced by the nature of the ligand used. The ligand-metal bond strength relies on the ligand functionalization as much as it does the type of

metal in the cluster. Many of the common MOFs made with carboxylate linkers, such as MOF-74, MOF-5, and HKUST-1, are known to be susceptible to degradation with water exposure.[18–20] On the other hand, phosphonate and azolate ligands form more robust frameworks that are more water stable.[21, 22] Size and shape together play important roles in the potential structure formation of the resulting MOFs, and are directly related to the ligands selected. An increase in ligand size increases the distance between metal clusters which gives a larger resulting pore size. This type of preparation is known as isoreticular chemistry. An example of this is a series of Mg-MOF-74-based frameworks made by Deng and coworkers.[23] Linkers of increasing size were used to create frameworks with ligand lengths ranging from 7 to 50 Å. However, this technique is not universally applicable. For many MOFs, if the inter-cluster spacing is too large, it would be thermodynamically favourable to decrease the void space of the pore if the framework allows for it. In order to do so, resulting structures are often interpenetrated, having two or more intertwined but separate networks running within each other and decreasing the pore size and space. In order to prevent this phenomenon, the geometry of the linker can be taken into account.

1.8 Ligand Types

The chemical nature of the ligand itself is used as a means of classifying different types of MOFs, and can be a large determining factor in the nature of the MOF itself. As mentioned before, carboxylate-based ligands are fairly common in MOF literature for their availability, and low-cost. Carboxylate ligands have formed MOF structures with some of the greatest surface areas. MOF structures based on imidazoles, pyrazoles and triazoles, have led to another set of unique materials. These azolate-based MOFs are charged frameworks that have high thermal

and water stabilities. Another class of highly stable MOFs is that of phosphonate MOFs. The phosphonic acid that comprises these ligands has two potential sites of deprotonation, allowing it to form stronger bonds than an acid with one site of deprotonation, such as carboxylic acids.[15] Unlike carboxylic acids, the phosphonic acid group extends in three dimensions, which allows it to undergo a variety of different coordination modes. This makes structure prediction with phosphonates more difficult, as phosphonates do not favour discrete metal cluster or SBU formation. Phosphonate ligands favour the formation of layers of bridged metal centres (M-O-P-O-M) connected by stacked phosphonate ligands.[24] Isolated clusters reported often require use of a chelating phosphonate and a chelating or capping secondary ligand in order to make cluster formation favourable.[24–26]

Formation of open frameworks with phosphonates involves a careful choice of ligand. Linear bisphosphonate linkers will often form dense materials as they facilitate a dense layered structure. Two-dimensional and three-dimensional ligands, conversely, can promote the formation of porous materials. The ligands (**4**) and (**5**), pictured in Figure 1.3, are two examples of phosphonate ligands that have successfully been used to form open frameworks.
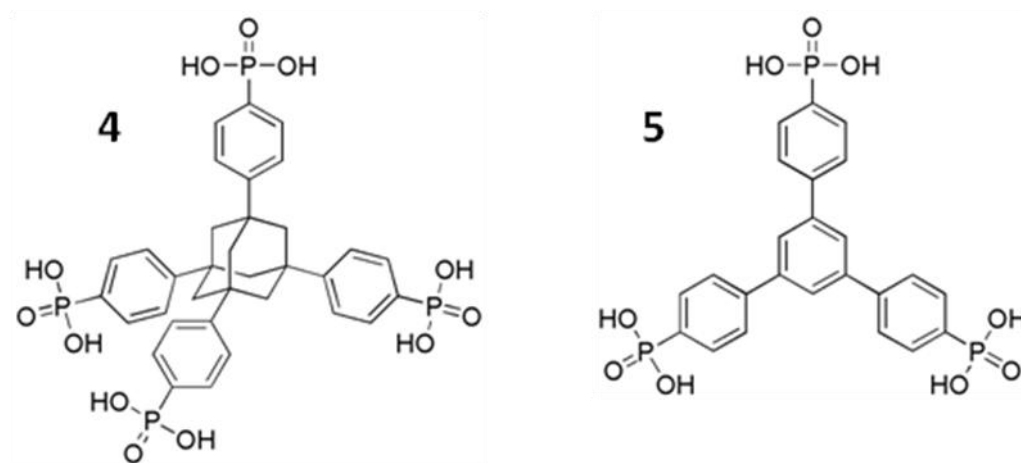
Figure 1.3. Phosphonate ligands that extend in three and two dimensions, respectively.

The adamantane-based ligand pictured in Figure 1.3, (**4**) 1,3,5,7-tetrakis(4-phenylphosphonic acid)adamantane, is an example of a three-dimensional ligand. It forms an interpenetrated diamond net when coordinated to copper (II), with a BET surface area of 198 m^2g^{-1}.[27] The second ligand pictured, (**5**) 1,3,5-(4-phosphonophenyl) benzene, produced a two-fold interpenetrated net with strontium (II) composed of alternating stacked layers in which the aryl linker would occupy the pore space between each layer. The three-fold symmetry of this ligand was able to drive the structure away from a typical layered model, creating a material with a 146 m^2g^{-1}.[28] In both of the above examples, the interpenetrated nets arose due to the symmetry of the ligand matching the symmetry of the metal cluster vertices (tetrahedral and trigonal planar, respectively). One of the major weaknesses of the aforementioned ligands is through their synthetic routes. Preparation of phosphonate ligands with two- and three-dimensional connectivities are typically multi-step reactions that often use the Michaelis-Arbuzov reaction to create a carbon-phosphorous bond.[29] This reaction, however, often requires high synthetic

11

temperatures and high-boiling organic solvents to reach the temperatures, which is disadvantageous to ligand production for industrial purposes.

1.9 Research Objective

This thesis presents two different methods which can be employed to create water-stable functional materials at a low cost. Chapter Two will discuss a method of post-synthetic modification using silica, while Chapter Three revolves around a low-cost, non-linear bisphosphonic acid ligand.

Chapter Two: **Silicated Metal-Organic Frameworks**

2.1 Introduction

2.1.1 Water Stability in MOFs

Water stability is a very important property for any commercial material, and this is no different for MOFs. MOFs are a relatively new class of materials which are of commercial interest for a variety of applications, including but not limited to catalysis, proton conductivity and gas capture.[7, 30–32] The water stability of MOFs has thus become of great interest, as it is crucial for many of the commercial applications. With respect to post-combustion carbon dioxide capture, a flue gas stream contains 5 to 7% water.[33] This seemingly small amount of water can pose a large challenge with prolonged exposure to a MOF. As the adsorption-desorption cycle occurs, water may bind to the most favourable sites, decreasing the amount of available surface for CO_2 adsorption. Prolonged water exposure can lead to framework decomposition at the metal centre.[20] Framework decomposition causes an overall decreased gas uptake via either blocked pores or structural collapse.[34]

There are varying needs for water stability in MOFs due to the variety of possible applications. Even within the carbon capture area, different possible scenarios arise. Most importantly, the material must be stable to water at room temperature for use in any commercial carbon capture application at a reasonable cost. Of secondary importance is the stability of the MOF to water under changes in temperature or pressure. Currently, there is no set standard for defining a MOF as "water stable". The literature on MOF water stability is sparse, and only recently have systematic studies started to emerge on some common MOFs.[19, 20, 34]

2.1.2 Quantization of Water Stability

Water stability can be quantified in three different ways. PXRD can be used to determine the overall structural change post exposure, which is useful for major degradation. Nitrogen uptake, though more time-consuming, can be used to quantify water-induced defects with more precision. A decreased gas uptake will highlight external structural collapse that blocks the pores but is not large enough in scale to affect average long range order and the overall powder pattern.   Both of these methods require a comparison to the raw material in order to quantify a change in the data. Another technique that is less common due to access to measurement facilities is water sorption. Water sorption isotherms can be used to classify the affinity between water and a material. This can be a good comparison alongside CO_2 isotherms for a better understanding of what the system will do when exposed to a flue gas stream. In practice, combinations of the three techniques give the most useful representation of a given system. There are a few factors that govern water stability in MOFs. The metal-ligand bond strength is one of the major characteristics that dictate water stability. Ligands that have a higher pKa or are chelating will produce stronger metal-ligand bonds, which in turn will increase the resistance of

the material for further reaction with water.[20, 34, 35] The coordination sphere around the metal is

another factor that can dictate if a material will be susceptible to degradation. One example of

this is the difference in stability between different metal-analogues within the MOF-74 family.

Different coordination strengths between metals and ligands cause slightly different responses in

each MOF, causing Mg-MOF-74 to be more water stable than its nickel (II) analogue.[5, 18, 34]

2.1.3 Post-Synthetic Modification

Post-synthetic modification is used to change the chemical nature of a MOF to create a

more desirable material. A number of different types and examples of PSM appear in the

literature, though can be grouped into three main categories. First is chemical functionalization,

in which mild reaction conditions are used to change or modify existing functional groups

located on the ligands.[36, 37] This method changes the chemical composition of the MOF in order

to modify interactions with potential adsorbates. Another type of PSM involves the replacement

of anions or cations in the framework, such as the exchange of Zn(II) for Cu(II) in carboxylate-

based MOFs.[38] In the case of charged frameworks, anion replacement is also possible.[39] Due to

the large surface area of MOFs, it is also possible to deposit materials on or inside the surface.

This technique is frequently used in the case of platinum-loaded MOFs for catalysis.[40] An

example of silication of MOFs conducted by Uemura and coworkers claimed to have formed

silica nanoparticles within HKUST-1.[41] They demonstrated that there is an increased interaction

between the HKUST-1 and water post silication, however there was no report on resulting water

stability.

2.1.4 Modification of MOFs with Silica

We were interested in determining whether post-synthetic modification of the MOF pore surface could change the water stability of the material. We theorized that silica would be able to form within MOF pores and potentially change the chemical dynamics within the MOF itself. Aside from water stability, there was interest in also improving the thermal stability, as well as using this as a proof of concept for possible further functionalization of MOFs.

Silica was chosen as the modifying material for three reasons. Our primary reason was that silica is a relatively easy-to-produce and versatile material, and the silication reagents are widely available at low cost. Silica is also a very thermally stable material. MCM-41, a mesoporous silica, is stable up to $1010^{o}C$ in inert atmosphere and $900^{o}C$ in the presence of oxygen, which is a large contrast to the stability of many MOFs.[42] This guarantees that silicated materials will function at the operating temperatures required for MOFs. Finally, silica is NMR-active, which can be used as an extra verification for loading.

2.1.5 Mg-MOF-74

Mg-MOF-74, also known as CPO-27-Mg, is a microporous MOF made up of the DOBDC linker with one-dimensional 12 Å hexagonal pores.[5] The edges of the pores contain Mg-clusters that, when fully activated, expose bare metal sites. The structure, shown in Figure 2.1, was first reported by Dietzel and coworkers in 2008.[5] Mg-MOF-74 isostructural with nickel, zinc and iron DOBDC frameworks. Out of all of the MOFs in this series, Mg-MOF-74 has the strongest initial adsorption interaction with CO_2, indicated by its high -Q_{st} value (47 kJ/mol).[43] Mg-MOF-74 has a reported BET surface area of 1800 m^2/g.[44]
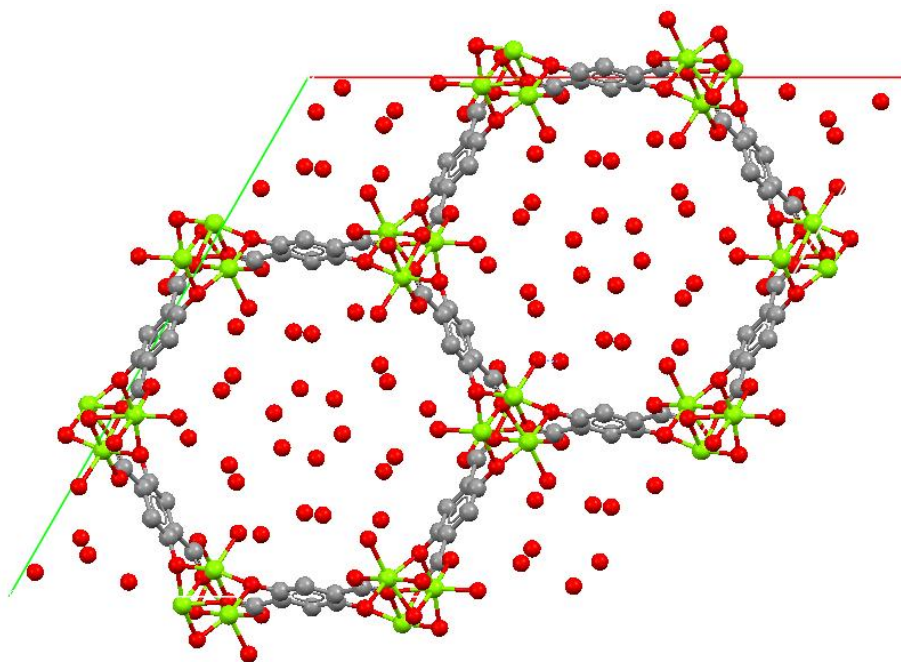
Figure 2.1. Crystal structure of Mg-MOF-74, depicting one-dimensional 12 Å pores.[5] Mg – green, C – grey, O, red.

2.1.6 HKUST-1

HKUST-1 is another common MOF with bare metal sites, composed of copper (II) metal clusters linked by BTC to form a porous framework that propagates in three dimensions. First described by Chui and coworkers, this framework has a bimodal pore distribution, with both 9 Å and 6 Å pore diameters, as seen in Figure 2.2.[16, 45] Similar to MOF-74, it has a strong interaction with CO_2 due to the presence of bare metal sites, indicated by its –Qst value (35 kJ/mol).[46]
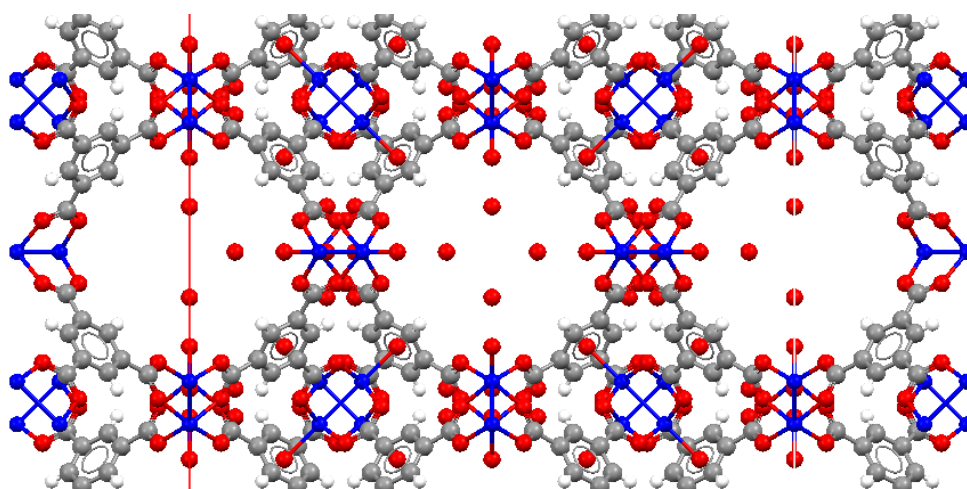
Figure 2.2. Crystal structure of HKUST-1, depicting bimodal pore system.[16] **Cu – blue, C – grey, O – red, H – white.**

2.2 Experimental

2.2.1 Instrumentation

All reagents were obtained from Sigma-Aldrich and used without further purification, unless otherwise stated.

SEM-EDX: samples were analyzed on a Zeiss Sigma VP SEM coupled with an EDX. INCA EDX processing software was used to capture and process EDX information. Samples were heated overnight under vacuum at 100°C prior to imaging. Samples were then cooled and loaded dry on carbon tape attached to aluminum sample holders. SEM-EDX for samples MOF-74-A, A1, A2, and A3: these samples were analyzed on a FEI XL30, 30 kV SEM and EDX data was processed by Genesis EDAX32 EDX processing software. Samples were prepared by grinding then were suspended (dilute) in MeOH and loaded wet onto carbon tape. Prior to analysis, samples were gold-plated.

Powder PXRD patterns of the samples were obtained on a Rigaku Miniflex X-ray diffractometer using a Cu Kα beam source. Samples were prepared by pre-grinding and were run on a glass zero-background plate. Scans were conducted between $2\theta = 3$ and 60^0, with a scan speed of 4.00^o/min and a sampling width of 0.02^o.

TGA-DSC data was obtained on a NETZSCH STA 409 PC TGA/DSC. For low temperature runs ($< 500^oC$), 3 to 10 mg of sample was ground then placed in a tared aluminum sample pan. For high temperature runs up to 1000^oC, an aluminum oxide pan was used. Samples were heated at 2^oC per minute.

Solid-state NMR data was obtained on a Bruker AMX 300 and processed using Bruker TopSpin software.

IR data was collected on KBr pellets of the given samples using a Varian 7000 Ft-IR Spectrometer.

All gas adsorption analysis was conducted on a Micrometrics Accelerated Surface Area & Porosity (ASAP) 2020 system under inert atmosphere using ultrahigh purity N_2 (99.999%) and CO_2 (99.999%). Typical activation on the degas side of the ASAP instrument involved a dual-stage heating, in which the temperature was ramped to 60^oC then held for 1 hr prior to increasing to the selected activation temperature. The pore size distribution of samples was measured using the Hybrid Density Functional Theory model provided on the Micrometrics ASAP 2020 software. Fits were conducted using the model for cylindrical pores in a pillared clay. Heat of adsorption for CO_2 was calculated using the Virial model to fit isotherms. The Virial equation was used to fit the isotherms. The Clausius Clapyron equation was then used to calculate –Qst.

2.2.2 Reference Silica Sample

A reference silica sample was prepared to compare to silicated MOFs. TMOS (0.4 mL) and water (0.005 mL) were added to a vial and stirred. While stirring, $NaOH_{(aq)}$ (0.002 mL, 1 M) was added to the vial. A cloudy, white precipitate formed.

2.2.3 Synthesis of Mg-MOF-74 (MOF-74-A)

Procedure adapted from literature synthesis.[5] Sixteen clean, dry 35 mL Chemglass glass hydrothermal vessels were obtained. Stock solutions of the base and two reagents were prepared. A stock solution of the metal was produced by dissolving $Mg(NO_3)_2 \cdot 6H_2O$ (6.485 g, 0.025 mol) in deionized water (50 mL). A stock solution of the ligand was produced by dissolving 2,5-dihydroxyterephthalic acid (2.398 g, 0.012 mol) in THF (160 mL). Finally, a solution of the base, TEA (8.4 mL, 0.060 mol) was prepared in THF (51.6 mL). To each glass vessel, the ligand stock solution (9.0 mL, 0.076 M) and a stir bar were added. While stirring, the base stock solution was added (2.3 mL). After the appearance of a white precipitate, the metal stock solution (2.7 mL, 0.5 M) was added to each vessel. Stirring was continued until the precipitate disappeared. The stir bar was then removed, and each vessel was capped and placed in the oven (2 h ramp, 72 h hold at 110°C, no cool down). The vessels were removed from the oven, and combined solutions were filtered using a medium frit, and rinsed with THF, water and methanol until the filtrate ran colourless. The yellow-green solid was allowed to dry on the filter and was then weighed (3.319 g, 125%, due to included solvent in the structure). Product was verified by PXRD and stored wet in methanol until use.

2.2.4 Alternate Synthesis of Mg-MOF-74 (MOF-74-B)

An alternate synthesis of Mg-MOF-74 was attempted, following a literature procedure reported by Dietzel and coworkers.[47] Although this synthesis results in a good yield of pure Mg-MOF-74, the use of DMF as a solvent resulted in residual effects on the silicated material that will be discussed in section 2.3.7. To a 150 mL beaker, Mg(OAc)$_2$·4H$_2$O (3.219 g), and 2,5-dihydroxyterephthalic acid (1.489 g) were added. N-methylpyrrolidone (90 mL) and water (10 mL) were then added and mixture was stirred until homogeneous. Mixture was distributed into 10 x 20 mL glass vials. Obtained product (2.200 g, 120% yield, due to included solvent) was collected by filtration, rinsing with methanol.

2.2.5 Synthesis of Silicated Mg-MOF-74

2.2.5.1 Sample A1 – Vapour Diffusion with TEA

A clean, dry H-cell was obtained. MOF-74-A was activated by Soxhlet in dry MeOH prior to use. A sample of MOF-74-A (approximately 100 g) was loaded wet in MeOH into an H-cell and activated at room temperature overnight. TMOS (2.4 mL, 0.016 mol) was added to the other arm of the cell. The H-cell was pump-purged to expose to vacuum, allowing the atmosphere to equilibrate in between pumps. The H-cell was then left under reduced pressure for 5 days to allow TMOS to diffuse into the sample. After 5 days, TMOS was removed by pipette and then TEA (2.0 mL) and water (4.6 mL) were added to the now empty arm of the H-cell. H-cell was pump-purged with indirect vacuum, then sealed at a reduced pressure for 5 days. Collected product was microscopically inhomogeneous, with large clumps of silica mixed in with the green MOF-74 powder.

2.2.5.2 Sample A2 – Vapour Diffusion without TEA

A sample of MOF-74-A was activated by soxhlet in dry MeOH prior to use then dried by vacuum filtration and loaded into an H-cell and activated at room temperature overnight. Sample was accidentally exposed to water during activation. H-cell was backfilled and weighed to determine the mass of the MOF-74 used (0.371 g, 1.5 mmol). TMOS (5.0 mL, 0.033 mol) was added to the other arm of the cell and the cell was pump-purged to allow TMOS to diffuse into the sample, while the MOF-74 was agitated by magnetic stirrer to ensure an even distribution of silica. After 6 days, TMOS was then removed by pipette and product was collected. Figure 2.3 offers a schematic on this method of silication, while contrasting it to A3.
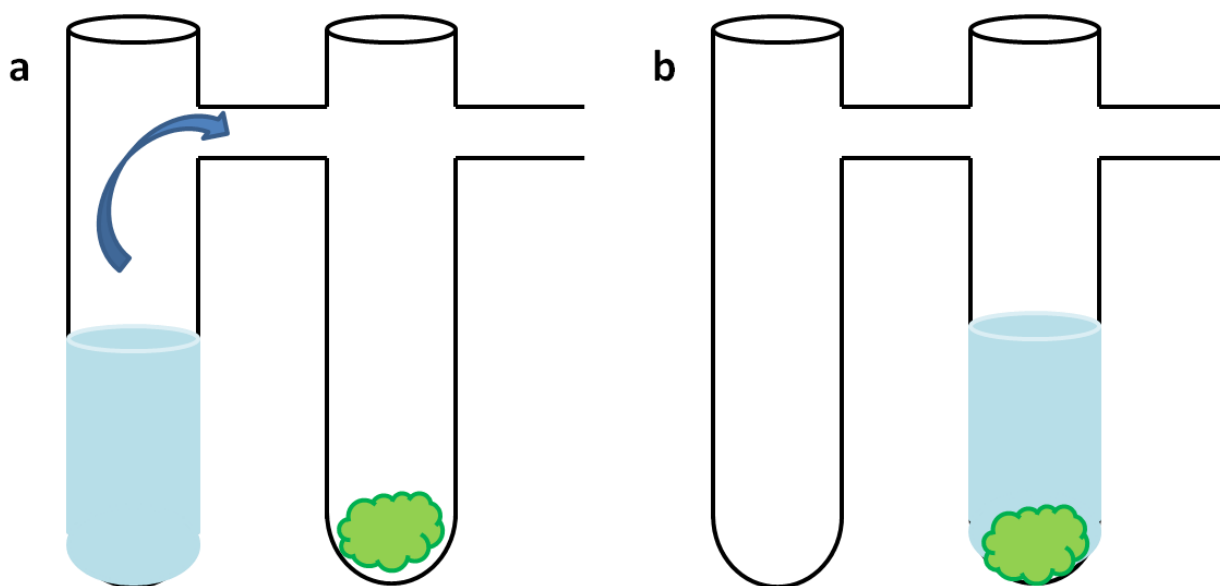
Figure 2.3. A schematic depicting the addition of TMOS to MOF-74 in (a) Sample A2 and (b) Sample A3.

2.2.5.3 Sample A3 – Immersion and Rinse

A sample of activated, wet MOF-74-A was partially dried by vacuum filtration and placed in a pre-weighed H-cell and activated at room temperature under vacuum overnight. The H-cell was then removed from vacuum, backfilled with argon and weighed in order to determine the mass of MOF-74 used (0.420 g, 1.7 mmol). Water (1.0 mL, 0.055 mol) was placed in the empty arm of the H-cell and the apparatus was sealed and placed under mild vacuum overnight. Water was then removed and TMOS (3.0 mL, 0.020 mol) was poured over the MOF and left for 10 days. Excess TMOS was removed by vacuum filtration, rinsing with hexanes over a base bath to quench unreacted TMOS.

2.2.5.4 Sample A4 – Using MOF-74-B

Sample A4 was prepared by Kyle Deakin.[48] The preparation procedure used was as follows:

As-synthesized MOF-74-B was placed in a disposable test tube (0.855 g, 3.5 mmol). TMOS (approx. 1 mL) was then added via pipette to the test tube until the meniscus of the TMOS was approximately one millimeter above the solid MOF-74. Let each test tube stand for 1 week. A homogeneous green solid was obtained.

2.2.5.5 Sample A5 – Time Dependant Loading and Water Stability

As-synthesized MOF-74-A was ground, filtered, weighed (1.413 g, 5.8 mmol) then placed in an H-cell and exposed to high vacuum overnight for two days to remove non-coordinated moisture. The partially activated MOF-74 was then submerged in TMOS (3.00 mL, 20 mmol) and left for a total period of 7 days. Small samples of the reaction were filtered for

EDX after 1, and 3 days of TMOS exposure. After 7 days, the reaction was vacuum filtered over

a base bath, rinsing with hexanes, to collect a yellow-green powdery solid (1.275 g). Analytical

calculated based on the molecular formula $Mg_2C_8O_4H_6$, 244.7 g/mol: C 39.26%, H 1.65%.

Actual: C 25.84%, H 4.62%. The discrepancy in values is likely due to coordinated water.

2.2.6 Preparation of MOF-74 for Adsorption Isotherms

Samples of silicated MOF-74 for gas adsorption experiments were pre-activated on the

Schleck line at 250^oC for between 24 and 48 hours, to ensure complete removal of potential

unreacted TMOS. Samples were then re-activated on the degas side of the ASAP instrument for

24 hours or until sample outgas levels reached a minimum (< 3 µbar/min). Samples were

backfilled with nitrogen and weighed prior to measurement.

2.2.7 Synthesis of HKUST-1

HKUST-1 was synthesized based on a literature procedure.[49] Four clean 20 mL Teflon

acid digestion vessels were used. EtOH (6 mL) and H_3BTC (0.73 g, 3.4 mmol) were added to

each reaction vessel and mixed by magnetic stirrer and sonication until a homogeneous white

suspension was formed. While stirring, aqueous solutions of $Cu(NO_3)_2{\cdot}2.5H_2O$ (1.7 g, 7.3

mmol) in water (6 mL) were prepared and added to the vessels. Vessels were allowed to until a

homogeneous turquoise gel was formed (approx. 4 hours). Vessels were sealed and heated for

15 h at 85^oC. Product was collected by vacuum filtration, rinsing with hot EtOH until blue

opaque gel was washed away. Deep blue crystals were obtained (3.765 g, 109% yield). In the

HKUST samples used for water stability tests, room temperature EtOH was used as a rinse. This

lead to the inclusion of trace amounts of $Cu(OAc)_2$ in the final product, due to a impurity of

acetic acid ($< 5\%$) in the H_3BTC reagent. This impurity was visible and sublimed upon activation of the post-water stability B2 sample, but did not affect the pre-water stability isotherm of the silicated material. Product was removed from other samples prior to analysis via a quick rinse with hot EtOH (~ 500 mL). The differences can be seen by TGA, demonstrated in Figure 2.25.

2.2.8 Synthesis of Silicated HKUST-1

2.2.8.1 Sample B1 – Mild Vacuum Dried HKUST-1

Sample B1 was prepared by Kyle Deakin.[48]

Non-activated HKUST-1 was filtered then placed in a disposable test tube (0.998 g, 16.4 mmol). TMOS (approx. 1 mL) was then added via pipette to the test tube until the meniscus of the TMOS was approximately one millimeter above the solid MOF-74. Let each test tube stand for one week. A blue crystalline sample was obtained.

2.2.8.2 Sample B2 – High Vacuum Dried HKUST-1

As-synthesized HKUST-1 was ground, filtered, weighed (2.035 g, 3.3 mmol) then placed in an H-cell and exposed to high vacuum overnight to remove non-coordinated moisture. Bumping of the solid occurred due to residual moisture on the surface of the powder, causing a mass loss. The partially activated HKUST-1 was then submerged in TMOS (2.00 mL, 13 mmol) and left for a total period of 7 days. Small samples of the reaction were filtered for EDX at 1,. After 7 days, the reaction was vacuum filtered over a base bath, rinsing with hexanes to collect a deep blue powdery solid (2.082 g). Analytical calculated based on the molecular formula

$Cu_3(C_9H_3O_6)_2$, 604.87 g/mol: C 35.7%, H 1.00%. Actual: C 26.54%, H 2.70%. The discrepancy in values is likely due to coordinated water and the presence of $Cu(OAc)_2$ as an impurity.

2.2.9 Preparation of HKUST-1 for Adsorption Isotherms

Samples of silicated HKUST-1 for gas adsorption experiments were pre-activated on the Schlenck line at 225°C for 24 hours, to ensure complete removal of potential unreacted TMOS. Silicated HKUST-1 from Method A was pre-activated at 250°C for 48 h, which resulted in a slight burnt brown-black colour in some of the sample, indicative of partial decomposition. Samples were then re-activated on the degas side of the ASAP instrument for 24 hours or until sample outgas levels reached a minimum. Samples were backfilled with nitrogen and weighed prior to measurement.

2.2.10 Water Stability Experiment

2.2.10.1 Setup

A glove bag was setup to contain samples in an enclosed atmosphere. A nitrogen gas tank was hooked up in series to an oil bubbler and water bubbler fitted with a stone bubbling chip which fed into the glove bag. The outlet of the glove bag was connected to an oil bubbler to control back pressure in the bag.

2.2.10.2 Preparation of Solutions to vary Relative Humidity

Saturated aqueous salt solutions were prepared and placed in the water bubbler to humidify the gas stream. Percent relative humidity was based on literature-reported values.[50] A list of the different solutions used and their RH values can be found below in Table 2.1.

Table 2.1. Salt solutions used along with corresponding percent relative humidity.

Salt Solution	% RH at Room Temperature[50]
$K_2CO_{3(aq)}$	43.17
$NaNO_{3(aq)}$	72.75
$BaCl_{2(aq)}$	89.80

2.2.10.3 Preparation of Samples

Prior to the experiment, Mg-MOF-74-A, HKUST-1, A5, and B2 were ground, placed in aluminum sample holders and heated to 150°C overnight in a vacuum oven to activate. Samples were left at 43% RH for 24 h, then the salt solution was interchanged and PXRDs of the samples were taken. The same samples were then left at 73% RH for 48 h and finally 90% RH for 72 h. Samples were monitored throughout by PXRD. When finished, samples were solvent exchanged under MeOH prior to further analysis.

2.3 Results and Discussion

2.3.1 Possible Outcomes of Silication

There are four different possible outcomes of silication, demonstrated by Figure 2.4. First, the sample can be enclosed or mixed in with bulk silica, in which a majority of the material is silica. This could happen if the silica reacts too quickly with the MOF surface. The second scenario depicted is the possibility of a thin silica layer enclosure, in which the external surface of a given particle is covered by only a thin layer of silica. This could occur if the silica selectively adheres to the surface, making reactions to cover the entire surface of the MOF more

26

favourable than diffusion within the MOF pores. In the third scenario depicted, silica could build up and completely fill the inside of the MOF prior to reacting with the outside. This scenario would occur if the diffusion of TMOS into the MOF is kinetically favourable, and occurs more rapidly than the silication reaction itself. The first three scenarios described would yield either nonporous materials, or materials in which the pores are inaccessible from the surface, which would not be favourable for CO_2 capture. If, however, the material can be silicated such that remaining pore space remains, there are two possibilities. First, the TMOS has the potential to preferentially orient itself within the framework around the metal centers, since MOFs with bare metal sites are highly polarizable materials.[51] In this case, decreases in uptake would selectively occur at either the low pressure or the high pressure region of the isotherm. The final possibility is to have randomly-oriented silica within the pores.
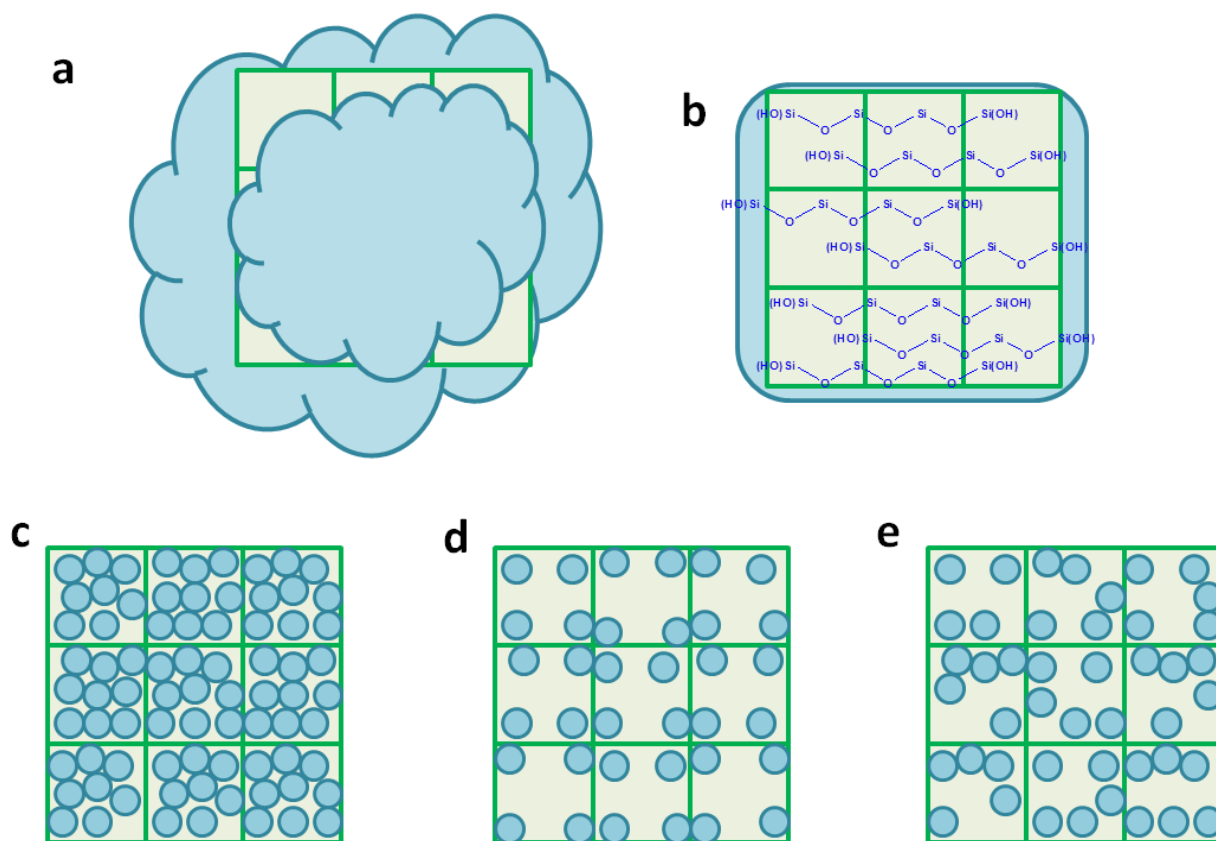
Figure 2.4. Possible outcomes of silication: (a) sample surrounded by silica, (b) thin monolayer production around sample, (c) completely filled pores, (d) preferred orientation within MOF pores, and (d) random orientation within MOF pores

2.3.2 Reference Silica Sample

The synthesized silica reference was used as a comparison for IR and solid-state ^{29}Si NMR. The solid-state NMR of silica contained one peak at -101 ppm, which corresponds to $[Si(OSi)_3(OR)_1]$.[52–56]

28

2.3.3 Reference MOF-74-A

MOF-74-A was used as a reference sample of comparison to determine the effect of silica on the sample. Various data presented in this section will be referred to throughout the report as a comparison.

2.3.3.1 SEM-EDX

Images of Mg-MOF-74 taken by SEM, shown in Figure 2.5, were used as a visual comparison for sample morphology, as Mg-MOF-74 sample is not very macroscopically crystalline and appears inhomogeneous under the microscope. EDX measurements, tabulated in Table 2.2, were taken as a comparison to ensure no silica was present in the un-loaded MOF. Measurements were taken using an area-averaged EDX on the SEM sample.

Table 2.2. Relative ratios of Mg to Si in sample MOF-74-A based on an area-averaged EDX measurement.

	Mg	Si
Average Weight %	95.75	4.23
Average Atomic %	96.3	3.7

HV	Mag	WD	Spot	Det	Tilt	Pos X	Pos Y	
20 kV	10000 x	9.3 mm	3.9	SE	0 °	14.9548 mm	-8.8415 mm	——5 µm——
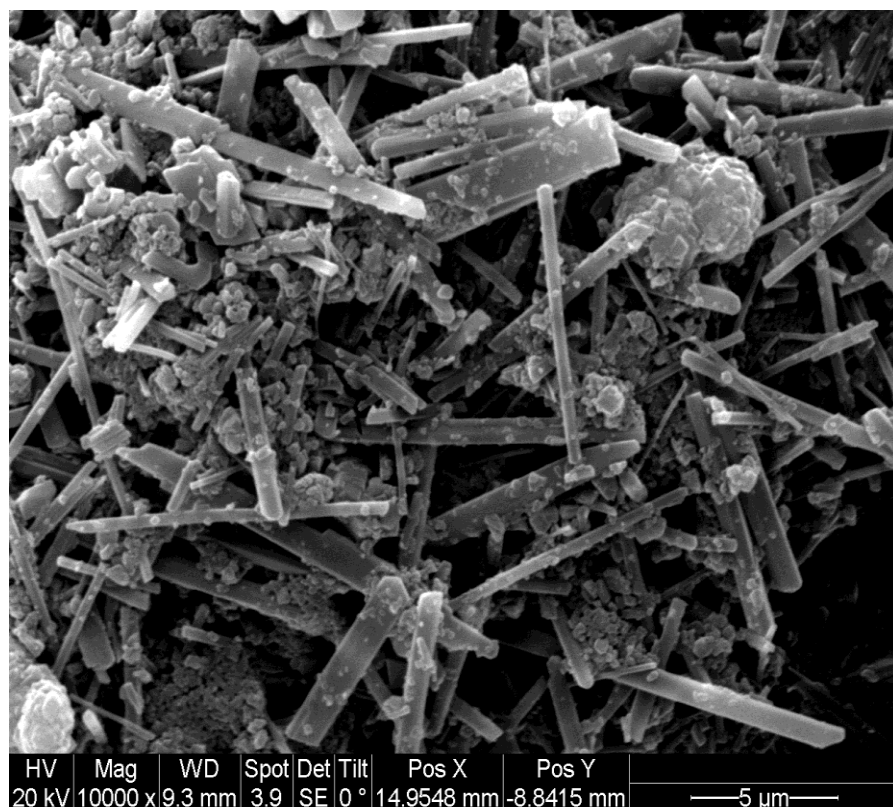
Figure 2.5. SEM image demonstrating the homogeneity of a sample of MOF-74-A.

2.3.3.2 Solid-State NMR

Solid-state ^{13}C NMR was conducted on Mg-MOF-74 as a comparison to ensure reaction completion in silicated samples of MOF-74. ^{13}C NMR (solid state) chemical shifts in ppm: δ 245.87, 227.77, 198.06, 179.50, 161.39, 131.66, 113.12, 95.00, 65.32, 54.19. The peak at 54.9 may correspond to MeOH.

2.3.3.3 Adsorption Isotherms

A nitrogen adsorption isotherm was taken as a comparison, shown in Figure 2.15. The overall uptake of MOF-74-A was 16.5 mmol/g and a calculated pore size of 12 Å.

2.3.4 Sample A1

The methods used resulted in drastically different macroscopic results. With A1, the resulting material was visibly covered in bulk silica, which could be seen with both the naked eye and under the microscope. The polymerization of TMOS can either be acid or base catalyzed.[57] Mg-MOF-74 was observed to be acid-soluble, however, making base catalysis the only viable option. TEA was selected as a catalyst since it is used in the MOF-74-A synthesis, implying the MOF would be stable to the catalytic amount used. Typical silication reactions can be either base or acid catalyzed, as TMOS alone reacts very slowly with water. The lack of homogeneity in this sample was caused by the excess accumulation of TMOS on the surface. When base catalysis is used to form aerogels, it leads to a material with an increased number of crosslinks, as opposed to acid catalysis, which leads to a silica with increased microporosity.[57] On top of this, kinetics of the one-dimensional pores in MOF-74 would have meant that a reaction would occur on the surface prior to within the MOF, as more time would be required for both the TEA and water to diffuse into the MOF.

2.3.4.1 SEM-EDX

The sample homogeneity was examined by EDX. SEM images, shown in Figure 2.6 and Figure 2.7, were taken of the sample and area-averaged EDX was taken at two different spots on each image. Atomic ratios from each are tabulated in Table 2.3. These atomic ratios indicate inhomogeneous loading, and large concentrations of silica in the sample. The amount of silica in the sample equates to approximately 6 Si atoms per Mg.

Table 2.3. Atomic % Mg and Si ratios in sample A1 determined by area-averaged EDX to show homogeneity.

	Mg	Si
Figure 2.6	30.18	69.82
Figure 2.6	25.05	74.95
Figure 2.7	0.51	99.49
Figure 2.7	0.57	99.43
Average Atomic %	14.08	85.92

HV	Mag	WD	Spot	Det	Tilt	Pos X	Pos Y	
20 kV	100 x	8.7 mm	4	SE	0 °	13.9073 mm	9.6675 mm	——500 µm——
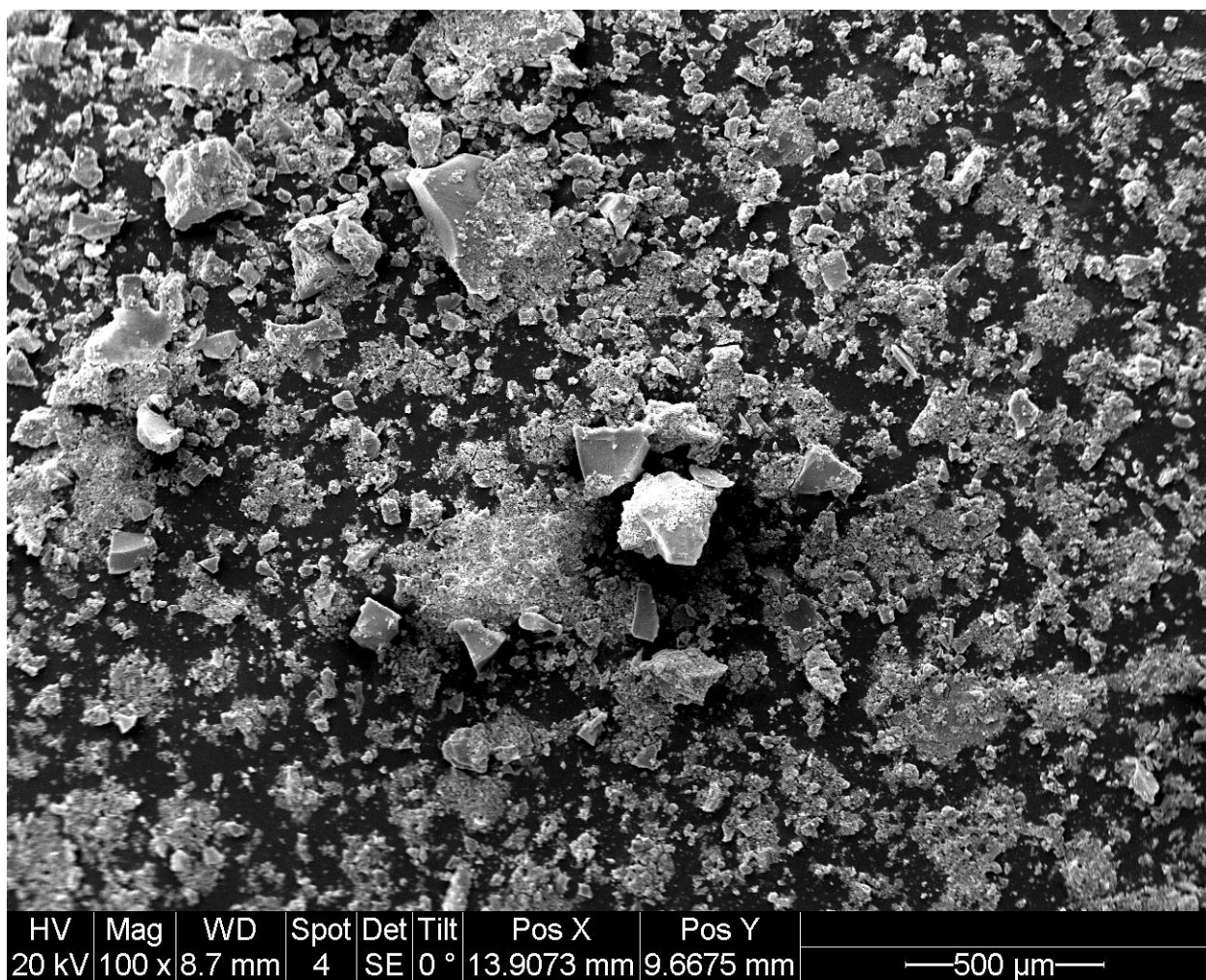
Figure 2.6. SEM image depicting homogeneity of sample A1.

HV	Mag	WD	Spot	Det	Tilt	Pos X	Pos Y	
20 kV	10000 x	8.7 mm	3.9	SE	0 °	13.8398 mm	9.7025 mm	⊢——5 µm——⊣
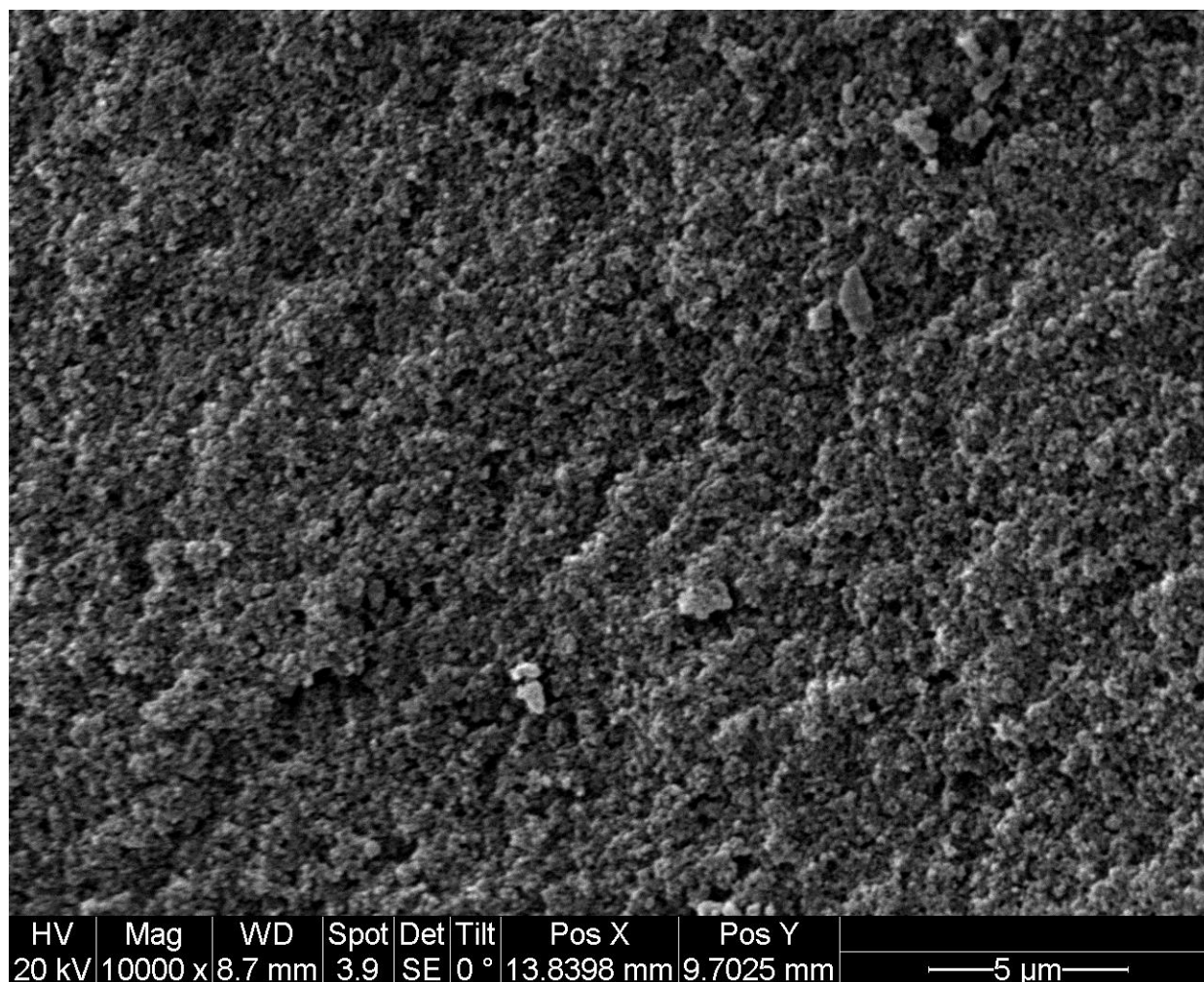
Figure 2.7. SEM image depicting homogeneity of sample A1.

2.3.5 Sample A2

In A2, water was accidentally added to the MOF prior to silication. The silication procedure was continued without TEA, in order to see if the TMOS had reacted. Filtration removed excess unreacted TMOS, yet there still remained questions about homogeneity on the microscopic level. Visually, the material appeared homogeneous after silication.

2.3.5.1 SEM-EDX

The imaged sample in Figure 2.8 showed no overall difference in appearance when compared to MOF-74-A. EDX values, listed in Table 2.4, demonstrated that this sample, A2, was more homogeneously loaded than A1, however there was still a large amount of variation between sections tested. Point tests were also conducted as a comparison tu further validate homogeneity. The amount of silica in the sample equates to 0.26 Si atoms per Mg.

Table 2.4. Atomic % ratios of Mg to Si in sample A2, determined using various area-averaged EDX measurements.

	Mg	Si
Sample Area 1	87.06	12.94
Sample Area 2	78.58	21.42
Sample Area 3	69.06	30.94
Sample Area 4	82.97	17.03
Average	79.42	20.58

HV	Mag	WD	Spot	Det	Tilt	Pos X	Pos Y	
20 kV	10000 x	9 mm	4	SE	0 °	-1.2588 mm	16.6048 mm	——5 µm——
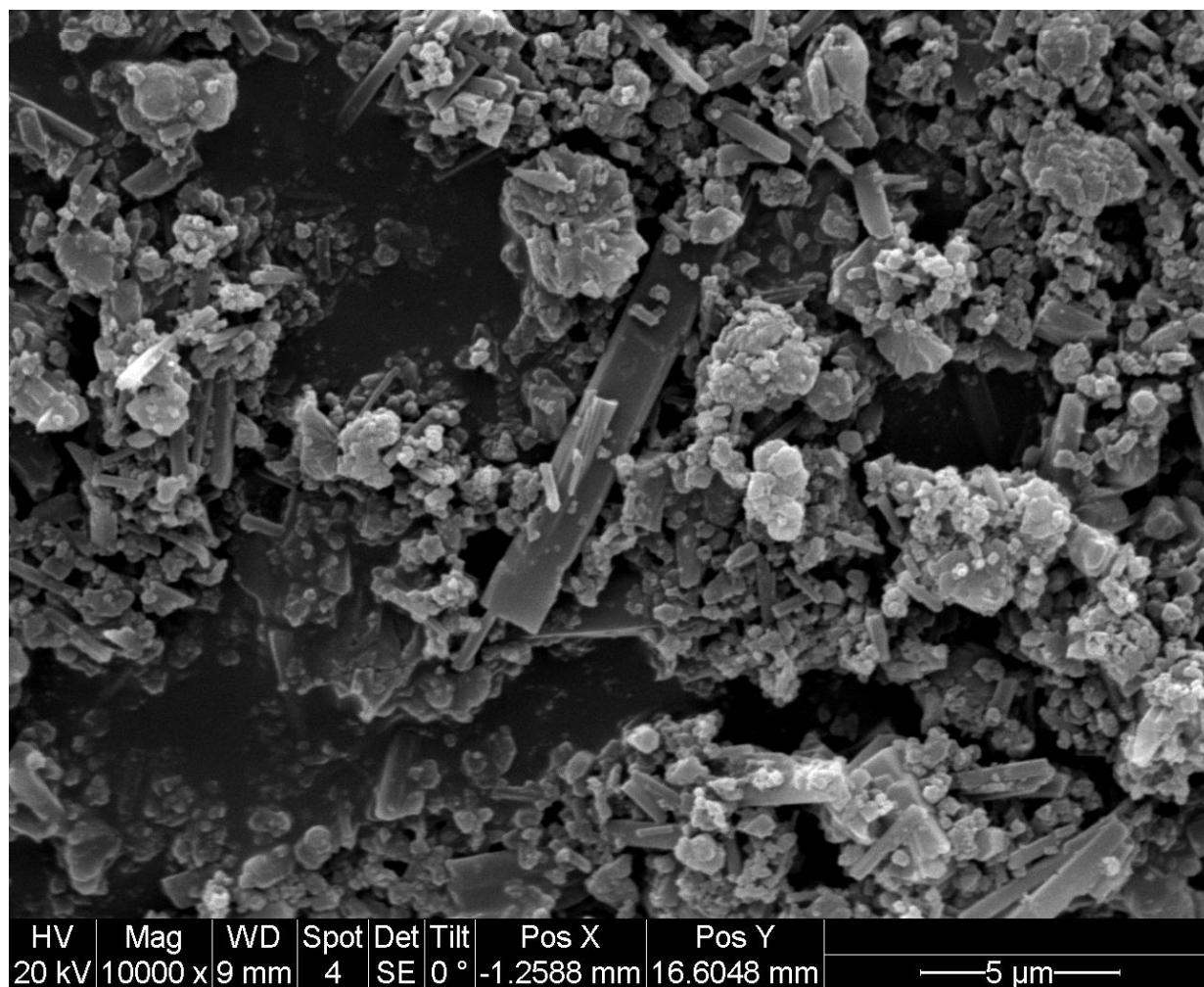
Figure 2.8. SEM image depicting homogeneity of Sample A2.

2.3.5.2 Solid-State NMR

Solid-state ^{29}Si NMR was used in order to determine whether the TMOS was fully

reacted. ^{29}Si-NMR resulted in two peaks of approximately equal area at -103 ppm and -94 ppm.

These peaks are indicative of $[Si(OSi)_3(OR)_1]$ and $[Si(OSi)_2(OR)_2]$, respectively, however the

^{29}Si NMR is indiscriminate of R-group.[52–55]

2.3.5.3 Infrared Spectroscopy

An IR of the silicated sample was compared to Mg-MOF-74 and raw silica. The broad peak from silica at 1084 cm^{-1} is visible in the MOF trace as seen in Figure 2.9. This band is due to an Si-O-Si asymmetrical stretching vibration.[58]
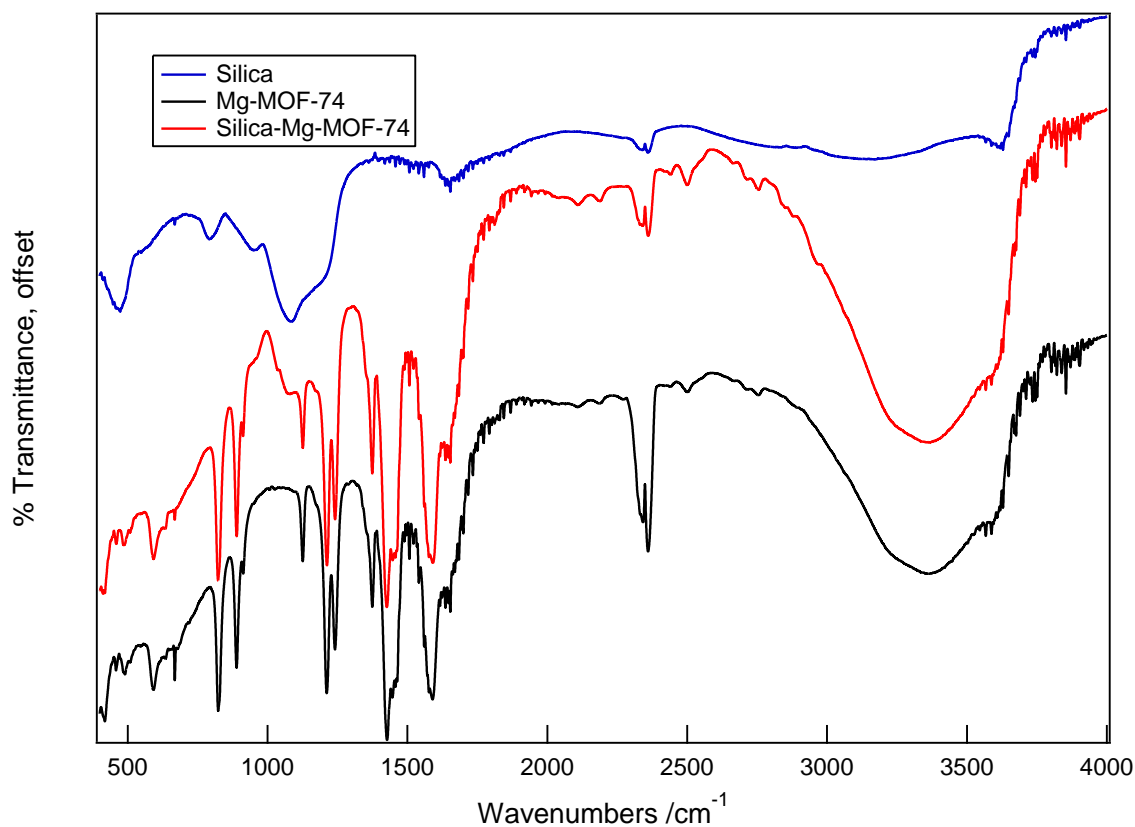
Figure 2.9. IR of Sample A2 (red), compared to MOF-74-A (black) and silica (blue).

2.3.6 Sample A3

With sample A3, water was added prior to TMOS, similar to sample A2. The main difference in this sample from A2 was the immersion of the MOF in TMOS rather than the use of vapour diffusion. The rinse with hexanes was intended to remove both bulk and surface

TMOS. This sample appeared to be a homogeneous green powder under an optical light

microscope. The difference in the addition of TMOS to the MOF is demonstrated in Figure 2.3.

2.3.6.1 SEM-EDX

    Images of the sample, shown in Figure 2.10 and Figure 2.11, resembled those of MOF-

74-A. Obtained EDX values, shown in Table 2.5, demonstrated that A3 was more homogeneous

than the previous two samples, though the Mg:Si ratio was similar to that of A2. A combination

of point EDX and area-averaged EDX was conducted on this sample. The data from Sample

Point 3 was determined to be an anomaly, based on the close values between the other points

obtained. The amount of silica equates to 0.43 Si atoms per Mg.

Table 2.5. Atomic % ratios of Mg to Si in sample A3, determined using various point and area-averaged EDX measurements.

	Mg	Si
Figure 2.10 Area 1	78.89	21.11
Figure 2.10 Area 2	76.03	23.97
Figure 2.10 Point 3	54.72	45.28
Figure 2.11 Area 4	70	30
Average	69.91	30.09

HV	Mag	WD	Spot	Det	Tilt	Pos X	Pos Y	
20 kV	20000 x	9.3 mm	4	SE	0 °	-16.2408 mm	7.38 mm	——2 µm——
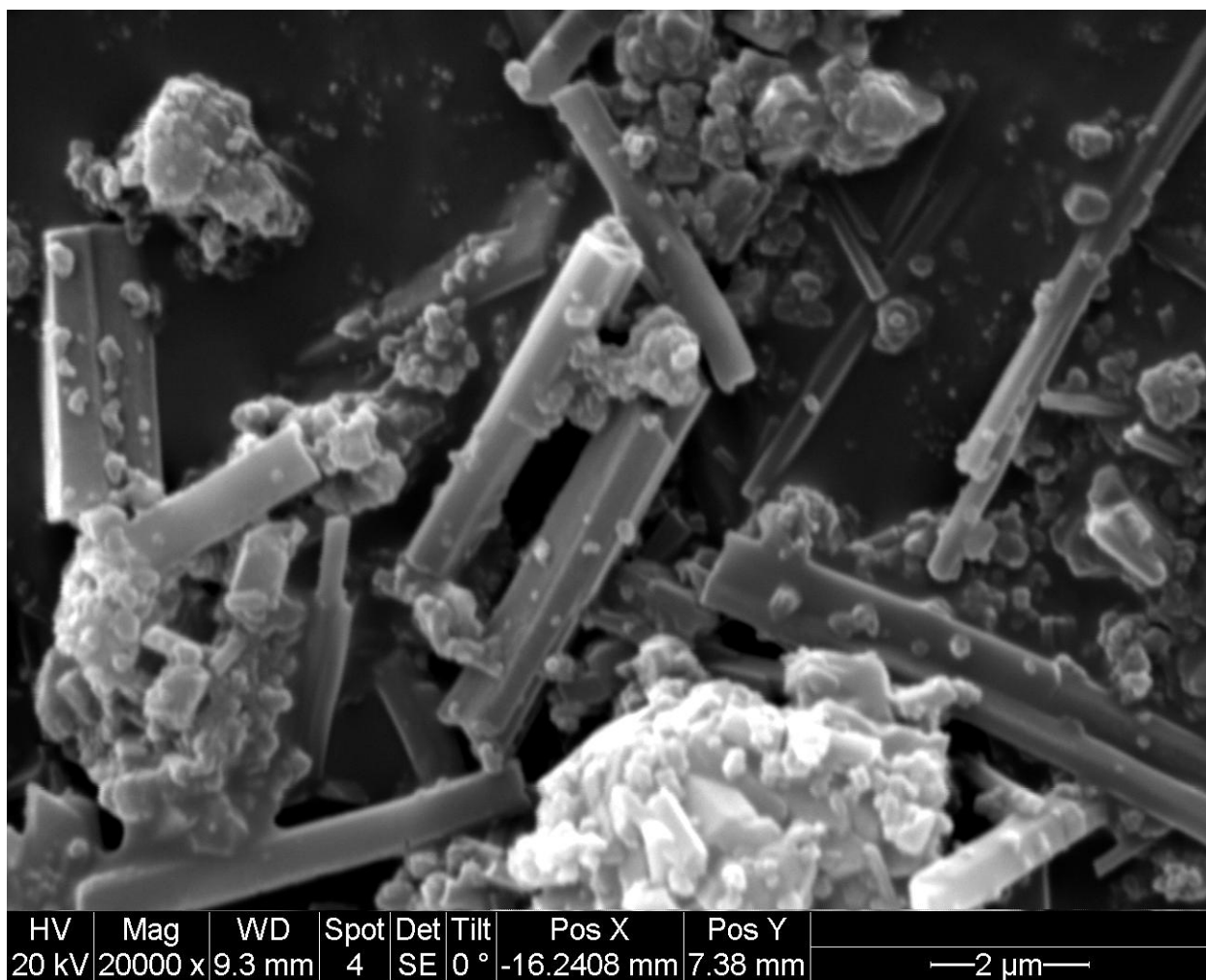
Figure 2.10. SEM image depicting homogeneity of Sample A3.

HV	Mag	WD	Spot	Det	Tilt	Pos X	Pos Y	
20 kV	20000 x	9.3 mm	4	SE	0 °	-16.2293 mm	7.3635 mm	——2 μm——
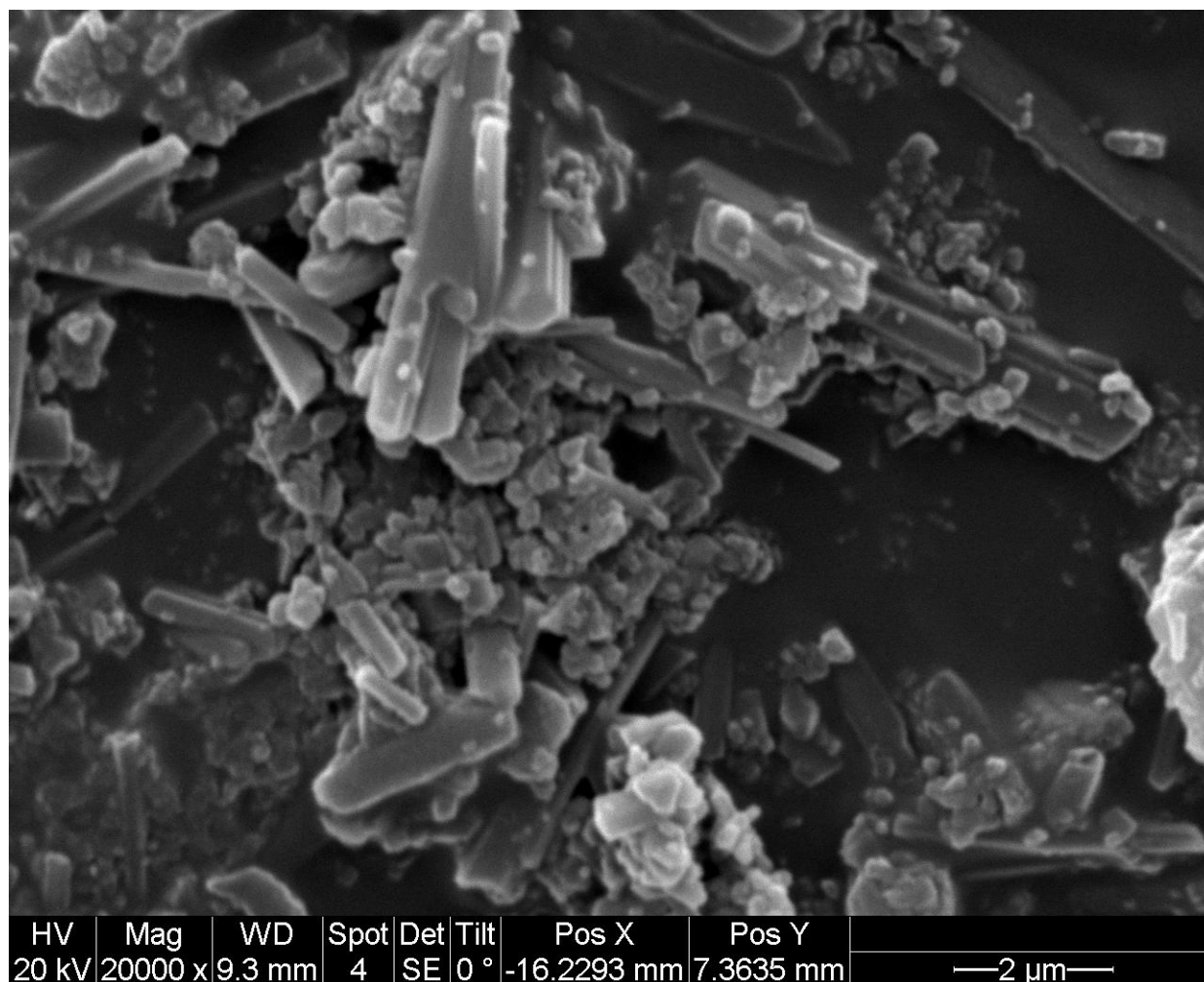
Figure 2.11. SEM image depicting homogeneity of Sample A3.

2.3.6.2 Solid-State NMR

The solid-state ^{29}Si NMR of sample A3 gave two broad peaks (-102 ppm and -94 ppm). These values closely matched those of A2, indicating that the silica loading was reproducible. Since solid-state ^{29}Si NMR is indiscriminate between hydroxyl and methoxyl functional groups, a solid-state ^{13}C NMR was taken as well. The ^{13}C solid-state NMR was compared to that of

40

MOF-74-A (listed in section 2.3.3.2) in order to verify the lack of silica in the sample. The two

NMRs matched perfectly, which is a good indication that TMOS and methoxy silane groups

were not present, although there is the possibility of the signal from TMOS overlapping with the

peak at 54.19 ppm, which is most likely caused by adsorbed MeOH in both frameworks. The

NMR and EDX data available was used to derive a theoretical molecular formula of

$[Mg_2(DOBDC)] \supset [SiO_3H_2]_{0.08}[SiO_{1.5}H]_{0.08}$.

2.3.7 Sample A4

Sample A4 was prepared with a MOF-74-B. Non-activated samples were used prior to

silication, which did not result in a usable product, based on characterization. The solvent

system used in MOF-74-B was indicated by Dietzel and coworkers to be detrimental to the

porosity of Mg-MOF-74 unless the solvent is completely removed by activation.[47]

2.3.7.1 SEM-EDX

Both the SEM images and accompanying EDX traces indicated a sample with

comparable homogeneity to A2. The Mg:Si ratio (75:25) is close in value to that of A2 and A3.
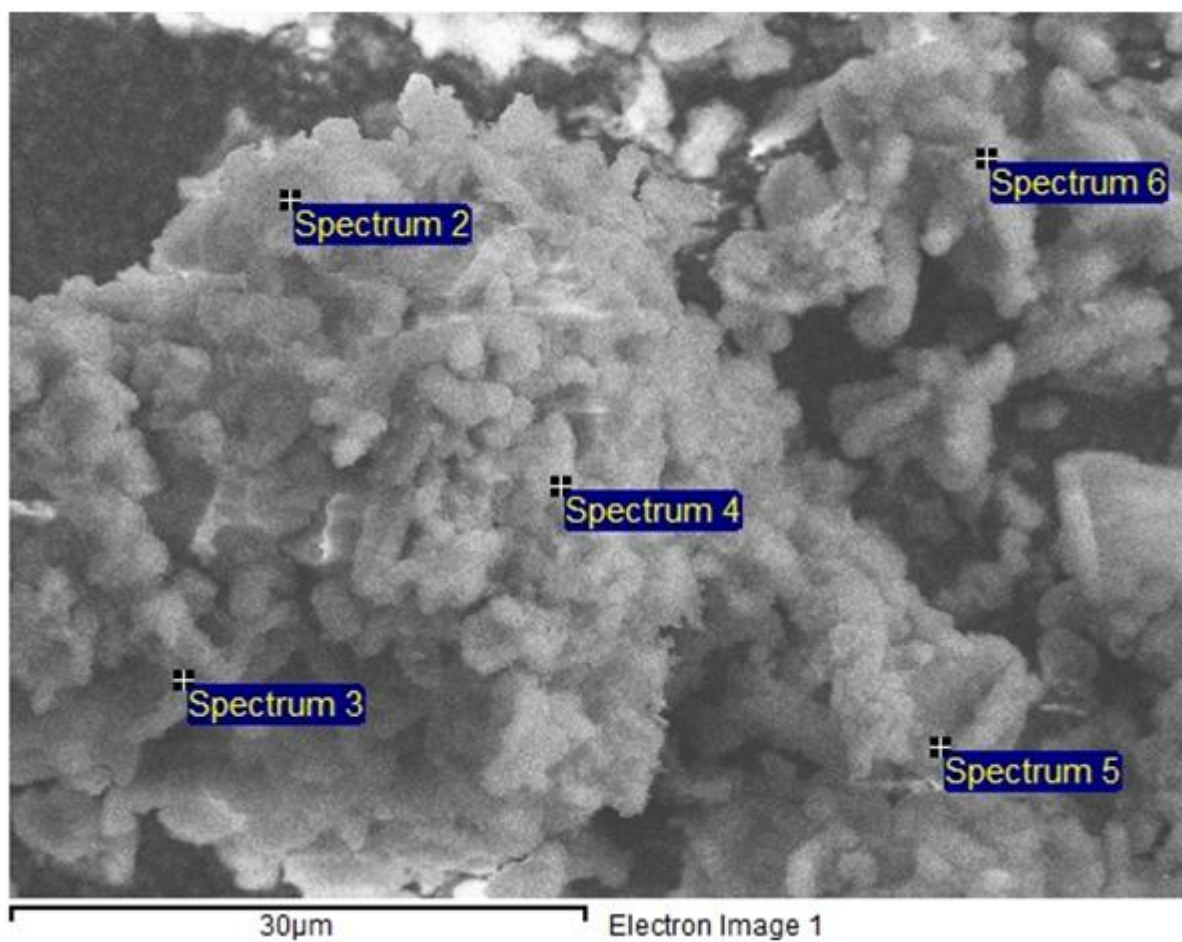
Figure 2.12. SEM image depicting homogeneity of Sample A4.

Table 2.6. Atomic % ratios of Mg to Si in sample A4, determined using various point and area-averaged EDX measurements.

	Mg	Si
Spectrum Area 1	68.6	31.4
Spectrum Point 2	73.62	26.38
Spectrum Point 3	87.53	12.47
Spectrum Point 4	90.67	9.33
Spectrum Point 5	72.75	27.25
Spectrum Point 6	71.99	28.01
Average Atomic %	77.64	22.36

2.3.7.2 Solid-State NMR

The solid-state ^{29}Si NMR of sample A4 had one broad peak with a maximum at -111 ppm, but appeared to overlap with a second peak at -101 ppm. These values indicate that the major component of silica in this sample is of the form of $[Si(OSi)_4]$.[54] The major implication of this is that the sample is most likely pore-blocked, since the one dimensional nature of the pores would prevent silica from propagating in three dimensions.

2.3.7.3 Nitrogen Adsorption

The blocked and partially-blocked pores of this sample combined with the use of N-methylpyrrolidone, a high boiling point solvent, lead to a very low uptake in the nitrogen adsorption isotherm (Figure 2.15 and Figure 2.16), with a pore size distribution indicating blocked pores, shown in Figure 2.17.

2.3.8 Sample A5

The preparation of sample A5 is similar to that of A3. In order to determine if time dependent loading occurred with the silication procedure, EDX values were used to measure the ratio of Mg to Si. As seen in Table 2.7, there is a steady increase in loaded silica over time. The presence of 4.21% Si after one day of exposure is indicative of a rapid uptake of the TMOS by the MOF. Worth noting, however, is the fact that a lot less silica was present in A5 than in previous samples. This is likely caused by the fact that the sample was not activated using the same method as previous samples. Rather than running a soxhlet in dry MeOH, the sample for A5 was prepared by room temperature vacuum to remove solvent. As Mg-MOF-74 is difficult to activate by high vacuum alone due to the kinetics of a one-dimensional porous system, this is likely a large influence on the resulting loading.

Table 2.7. Atomic % ratios of Mg to Si in sample A5, determined using EDX mapping.

	Mg	Si
Average 1 day	95.79	4.21
Average 3 days	93.71	6.29
Average 7 days	88.91	11.09

2.3.9 MOF-74 Sample Comparison

2.3.9.1 Crystallinity

All samples retained their crystallinity post-silication, as shown in Figure 2.13. This indicates that the silica does not have a preferential orientation within the MOF-74 unit cell, as well as demonstrating that the samples are chemically stable to the silication process.
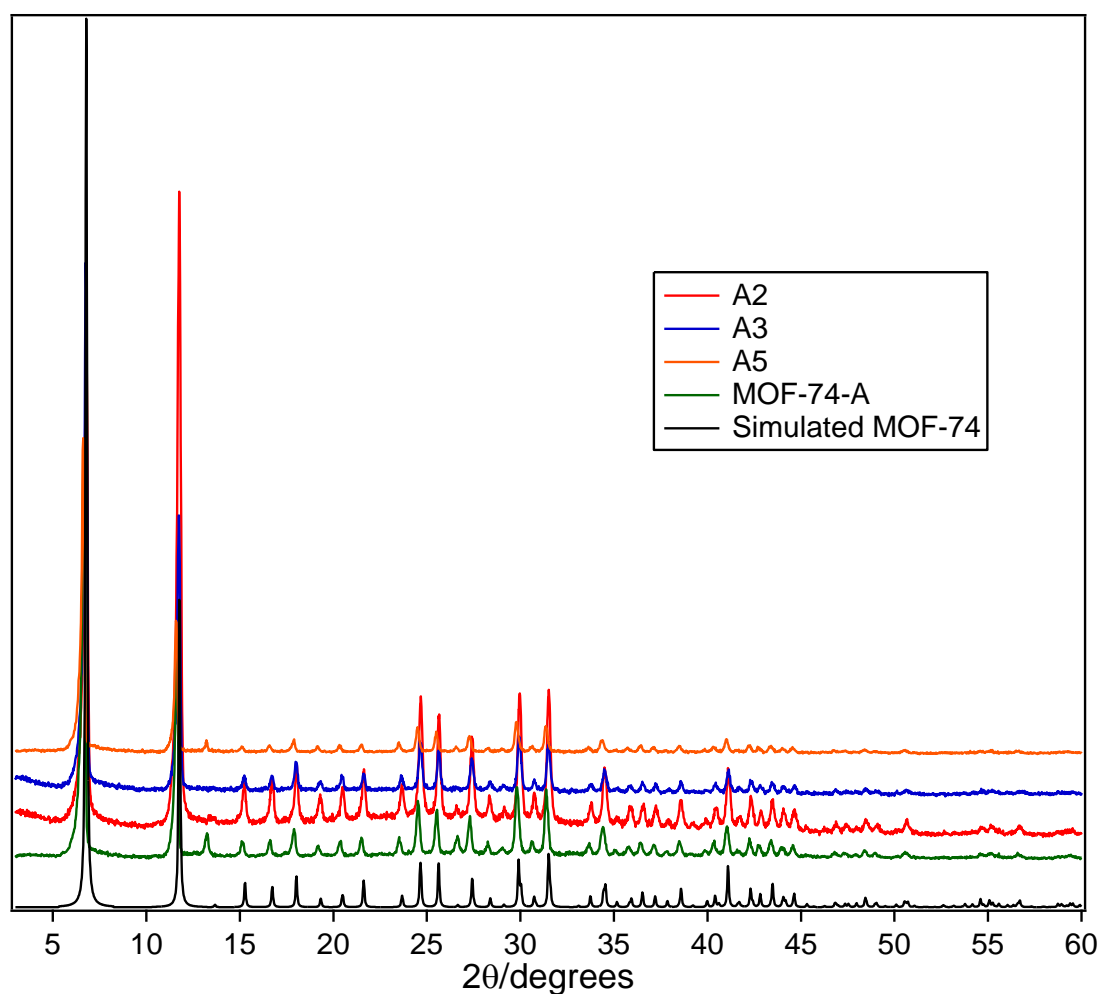
Figure 2.13. PXRD comparison of MOF-74-A to Samples A2, A3, and A5. Simulated pattern obtained from literature crystal structure.[5]

45

2.3.9.2 Thermal Stability

Silicated MOF samples A3, A4 and A5 were compared to MOF-74-A and MOF-74-B, shown in Figure 2.14. For sample A3 and A5 relative to MOF-74-A, the decomposition temperature of the framework was lowered upon silication by approximately $10^{o}C$. This indicates that the silica has a negative influence on the thermal stability of the framework. In the case of MOF-74-B relative to MOF-74-A, the decomposition of the former occurs at a lower temperature by a difference of approximately $50^{o}C$, while sample A4 is about $150^{o}C$ less stable than MOF-74-A. This could either indicate a decrease in thermal stability, or that the removal of adsorbed solvent occurs close to the temperature of framework decomposition.
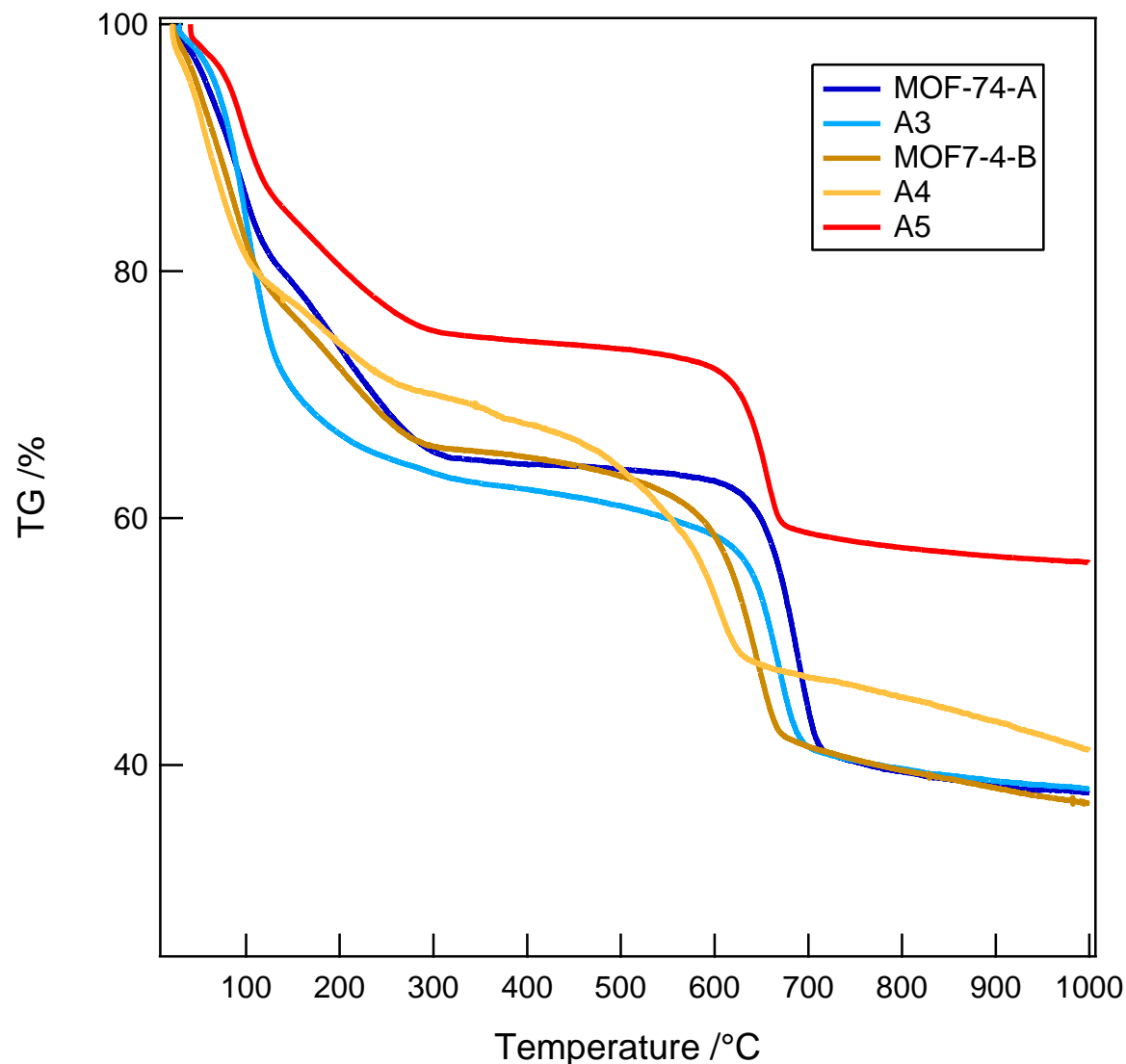
Figure 2.14. TGAs depicting thermal stability of MOF-74-A, MOF-74-B, A3, A4 and A5.

2.3.9.3 Nitrogen Adsorption

Nitrogen isotherms of Mg-MOF-74, shown in Figure 2.15, are typical type I isotherms of a microporous material with strong interactions.[59]   There is a very abrupt low pressure uptake, with a sharp knee leading to a plateau. In the logarithmic plot of the isotherm, Figure 2.16, a two-tiered uptake is visible due to the high-energy metal sites available. In all cases of silicated Mg-MOF-74, the overall uptake was decreased in the silicated MOFs due to the presence of

silica in the pores. The nitrogen adsorption isotherm of A3 relative to MOF-74-A showed a uniform decrease in uptake at both the low pressure region of the isotherm and at the plateau, which indicates that there was little to no preferential orientation of the silica relative to the bare metal sites. The pore size distribution of A3 showed a uniform decrease in pore size from 12 Å to 7 Å. This coincides with a partially filled pore. The overall nitrogen uptake of A3 was half that of MOF-74-A, with calculated BET surface areas of 758.1479 m²/g and 1547.5696 m²/g, respectively.

The calculated pore size distributions of the varying MOF-74 materials are further evidence of the homogeneity of loading of samples A3 and A5. Samples A3 and A5 both have a reduced pore size, however some 12 Å pore space remains. This indicates that the silica does not coat the entire inner surface of the MOF, although the reduction of pore size is indicative that silica is present. Notably the initial sample of MOF-74-A appears to have 6 Å pores. This is likely due to partial pore blocking synthesis, combined with partial collapse of the pores upon activation.[60] A less destructive activation technique is the use of supercritical CO_2 to remove solvent without the abrupt temperature and pressure change that causes partial pore collapse. Sample A4 was confirmed to be mostly pore-blocked, due to the lack of large pores in the material.
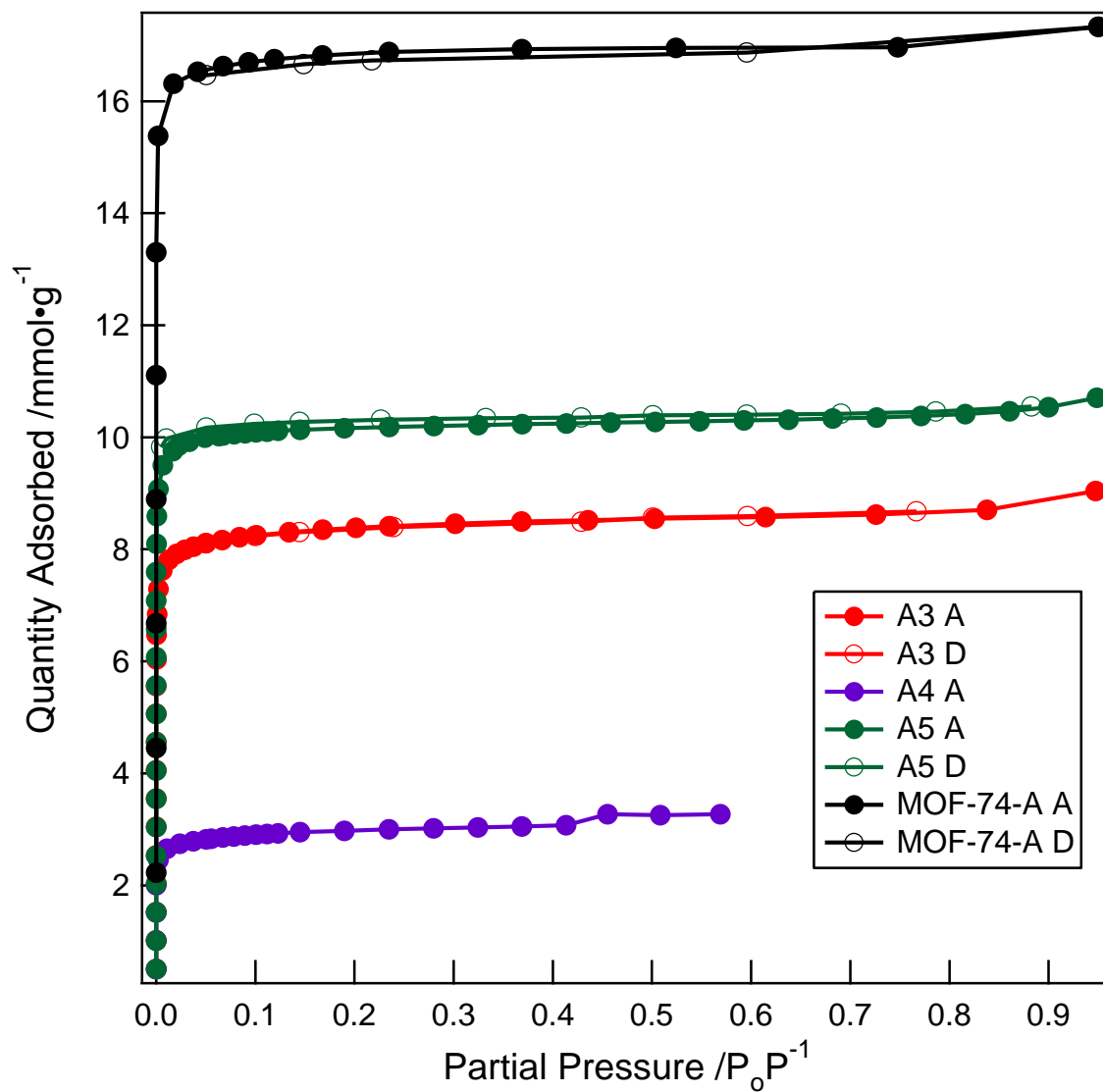
Figure 2.15. Linear nitrogen isotherm plot at 77 K comparing MOF-74-A to samples A3, A4, and A5. A – adsorption; D – desorption.
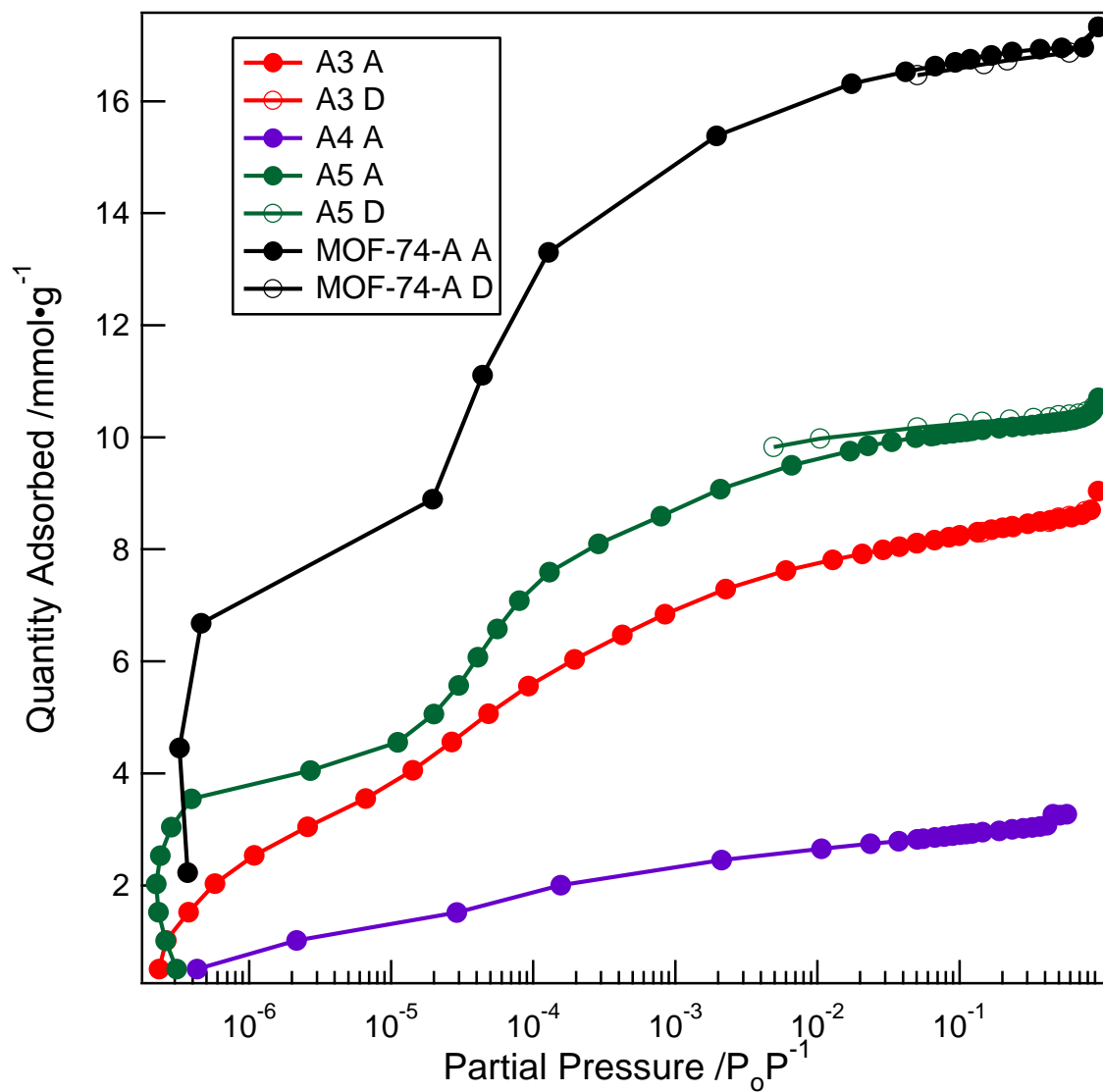
Figure 2.16. Logarithmic nitrogen isotherm plot at 77 K comparing MOF-74-A to samples

A3, A4, and A5. A – adsorption; D – desorption.
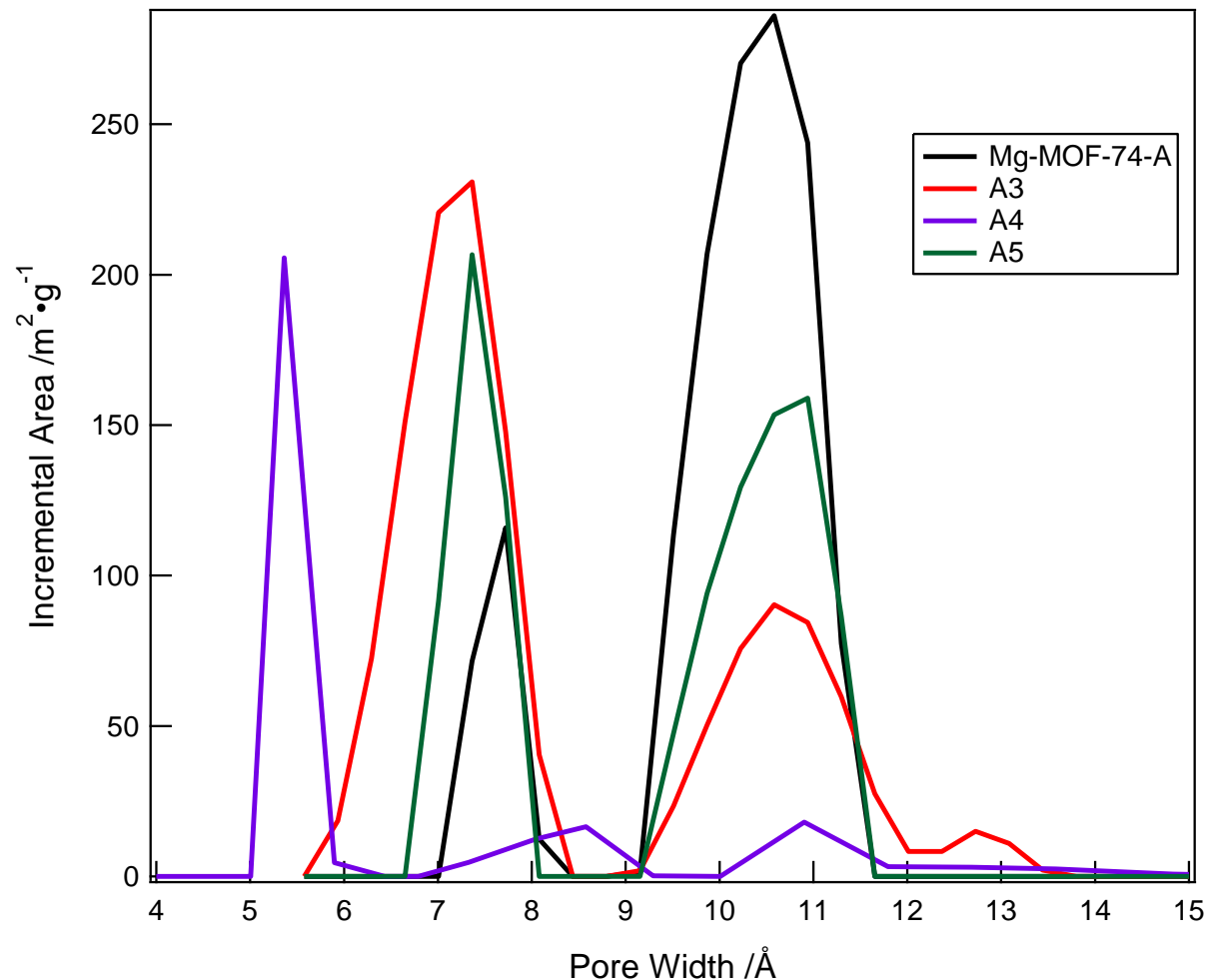
Figure 2.17. Calculated pore size distribution plot, comparing MOF-74-A to samples A3, A4, and A5.

2.3.9.4 Carbon Dioxide Adsorption

Carbon dioxide adsorption isotherms of A3, taken at 263 K and 273 K, were used to calculate the heat of adsorption, shown in Figure 2.18. The calculated $-Q_{st}$ (65.4 kJ/mol) is significantly greater than the literature value for MOF-74, while the heat of adsorption rapidly drops off.
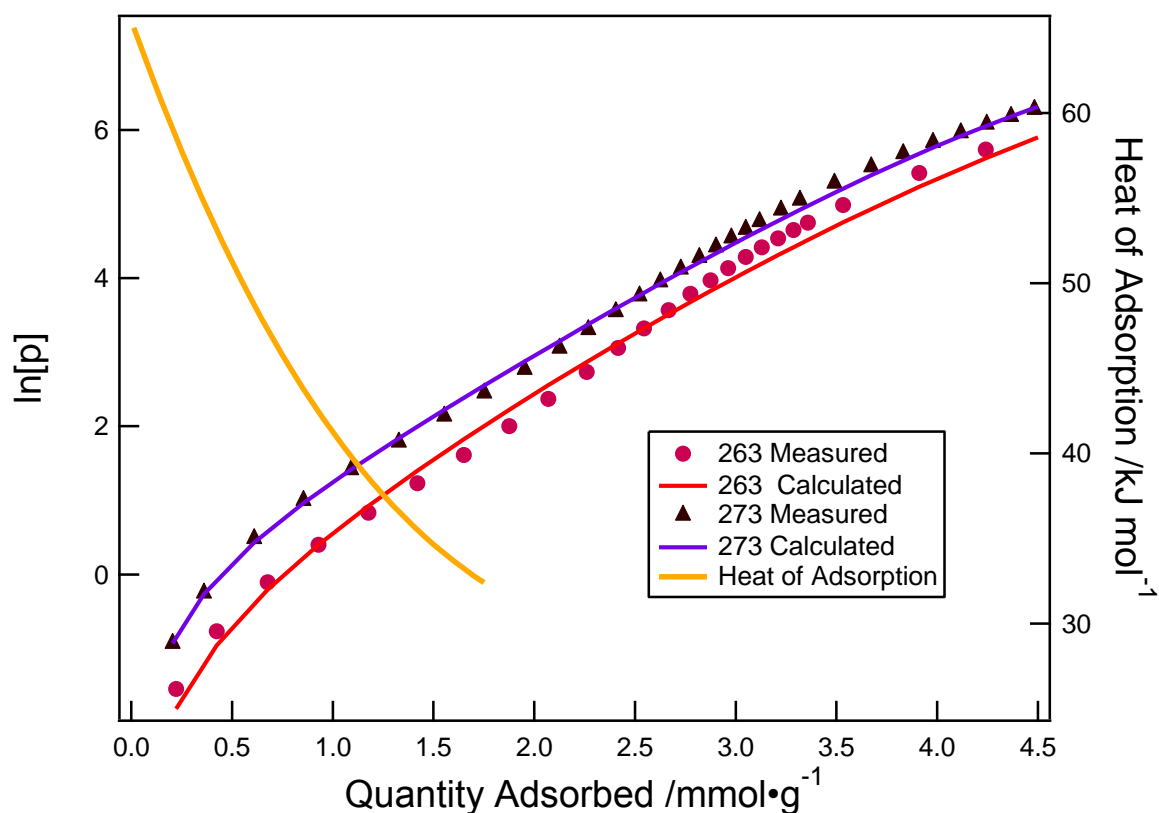
Figure 2.18. Carbon dioxide adsorption isotherms of sample A3 at 263 K (red) and 273 K (violet) and the HOA (orange), fitted using a virial model.

There could be two factors contributing to the high value. First, the silica could be acting as a polarizing surface for carbon dioxide, however, this would not correspond with the $-Q_{st}$ of CO_2 onto porous silicas such as MCM-41 (25 kJ/mol).[61]

It is also possible that the framework itself retained its high heat of adsorption; however there may be a larger error in the fitting of the first few points of the isotherm. This second explanation coincides with the findings of McDonald and coworkers while loading an extended Mg-MOF-74 framework with aminated ligands; two separate Langmuir−Freundlich equations were used to separately model the isotherm.[37] Contrary to the silicated samples, however, the

aminated ligands created very strong interactions with the adsorbed CO_2 gas which caused a

prominent step in the low pressure region. With sample A3, the Virial has difficulty fitting the

curve at both the low and the high pressure regions of the isotherm, especially evident at 263 K.

2.3.9.5 Reproducibility of Silication

Of all of the samples tested, A3 and A5 yielded the best results for homogeneous silica

loading. These samples showed consistent ratios of Mg to Si, on top of demonstrating high

nitrogen uptakes and homogeneous samples. Based on the NMR analysis of A3, it is evident that

a catalyst is not needed for the functionalization of MOF-74 with silica. We deduced from this

that the Lewis acidity of the bare magnesium metal sites may offer enough driving force for the

reaction to proceed. The silica, however, appears to be independently oriented relative to bare

metal sites based on nitrogen adsorption data, which indicates that this could not have been the

only driving force. Another possibility is that the confined space of a 12 Å pore may have driven

the reaction further. Overall, a fairly reproducible method of loading silica into MOF-74 has

been presented.

2.3.9.6 Water Stability Experiment

MOF-74-A and sample A5 were monitored by PXRD over the course of the water

stability experiment. PXRD patterns, shown in Figure 2.19 for MOF-74-A and Figure 2.20 for

sample A5, remain unchanged over the course of the humidity treatment. This indicates that

overall long-range order is not lost in the sample. The nitrogen sorption isotherm in Figure 2.21

and Figure 2.22 of sample A5, however, does not have any low-pressure uptake. The knee of

this isotherm is also no longer sharp, and the concave inflection at the higher end of the isotherm

is indicative of surface condensation on a non-porous sample.[59] Thus, it can be concluded that

the silicated sample A5 is not stable to the humidity treatment given.

Figure 2.19. PXRD patterns comparing MOF-74-A over the course of the water stability experiment.
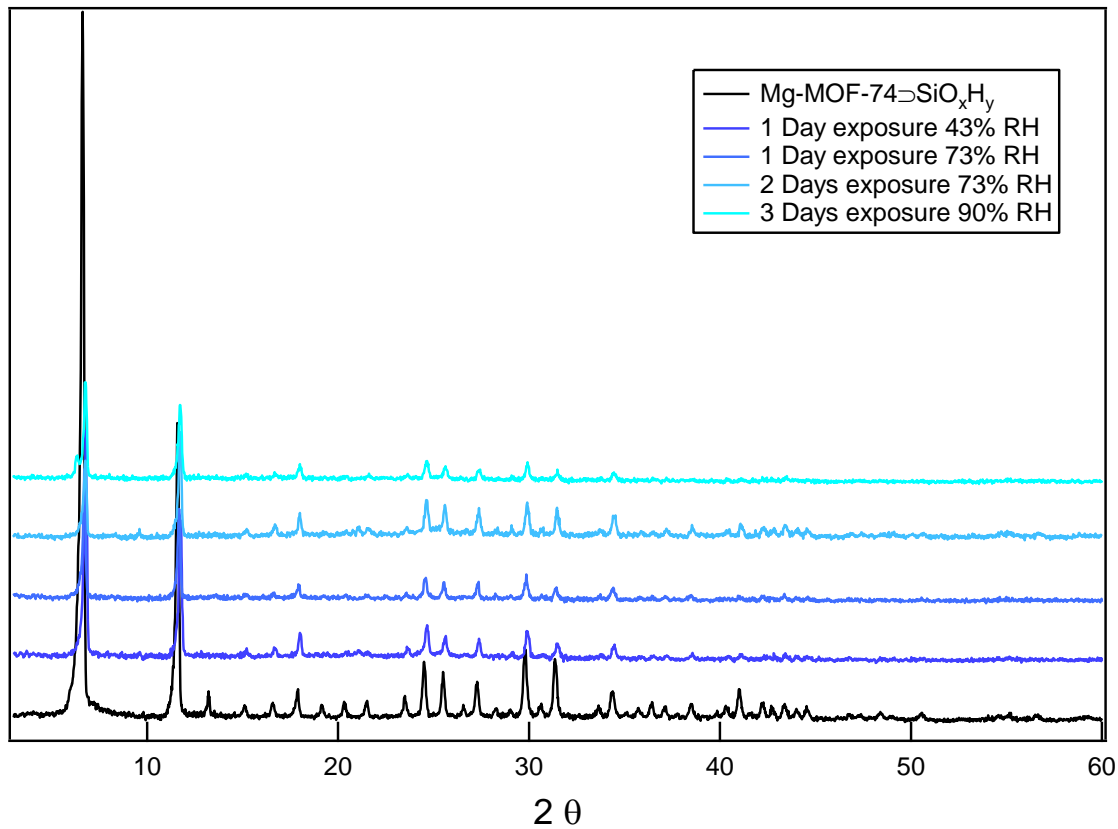
Figure 2.20. PXRD patterns comparing sample A5 over the course of the water stability experiment.
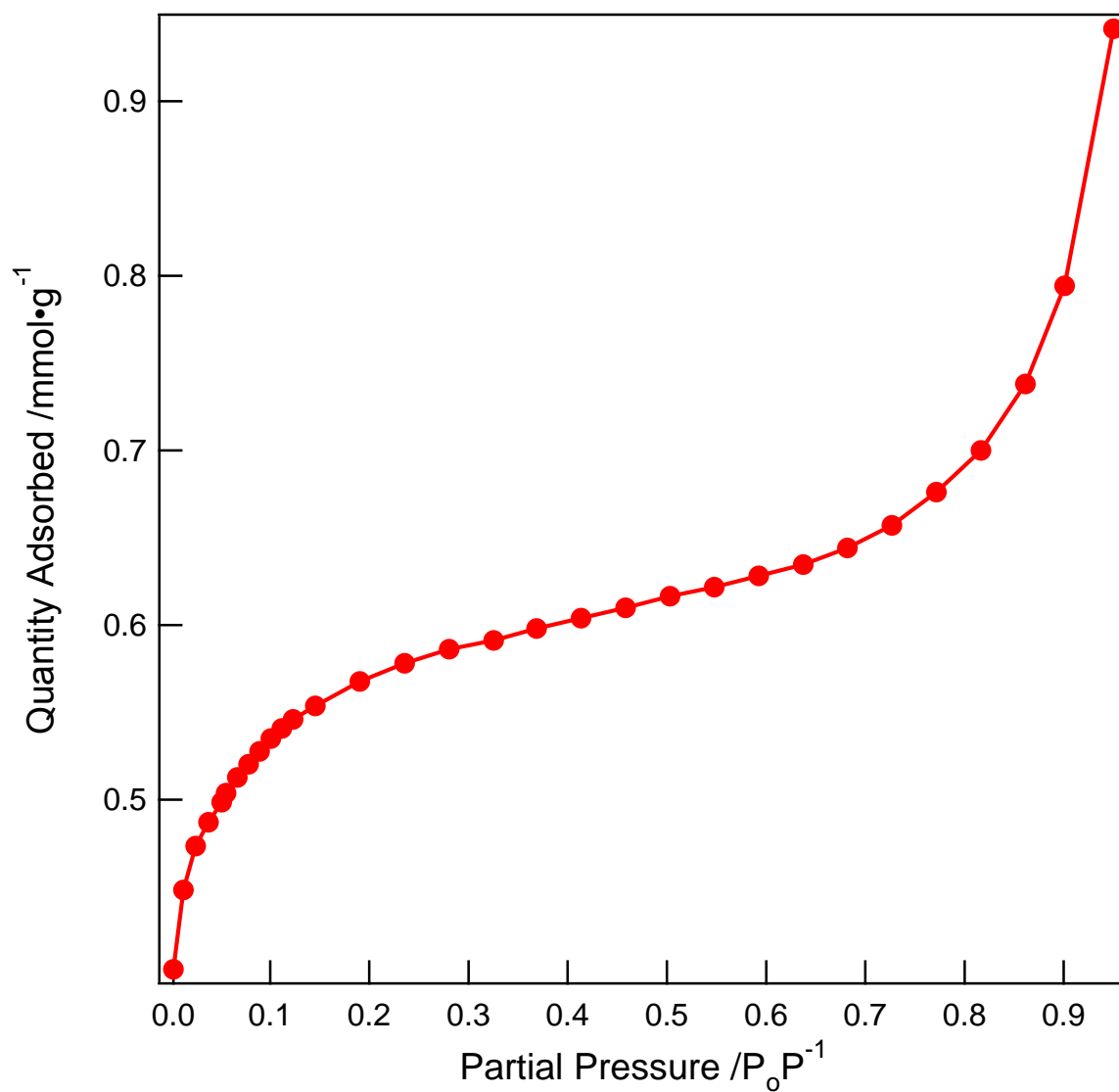
Figure 2.21. Linear nitrogen adsorption isotherm at 77 K for sample A5 post-humidity treatment.
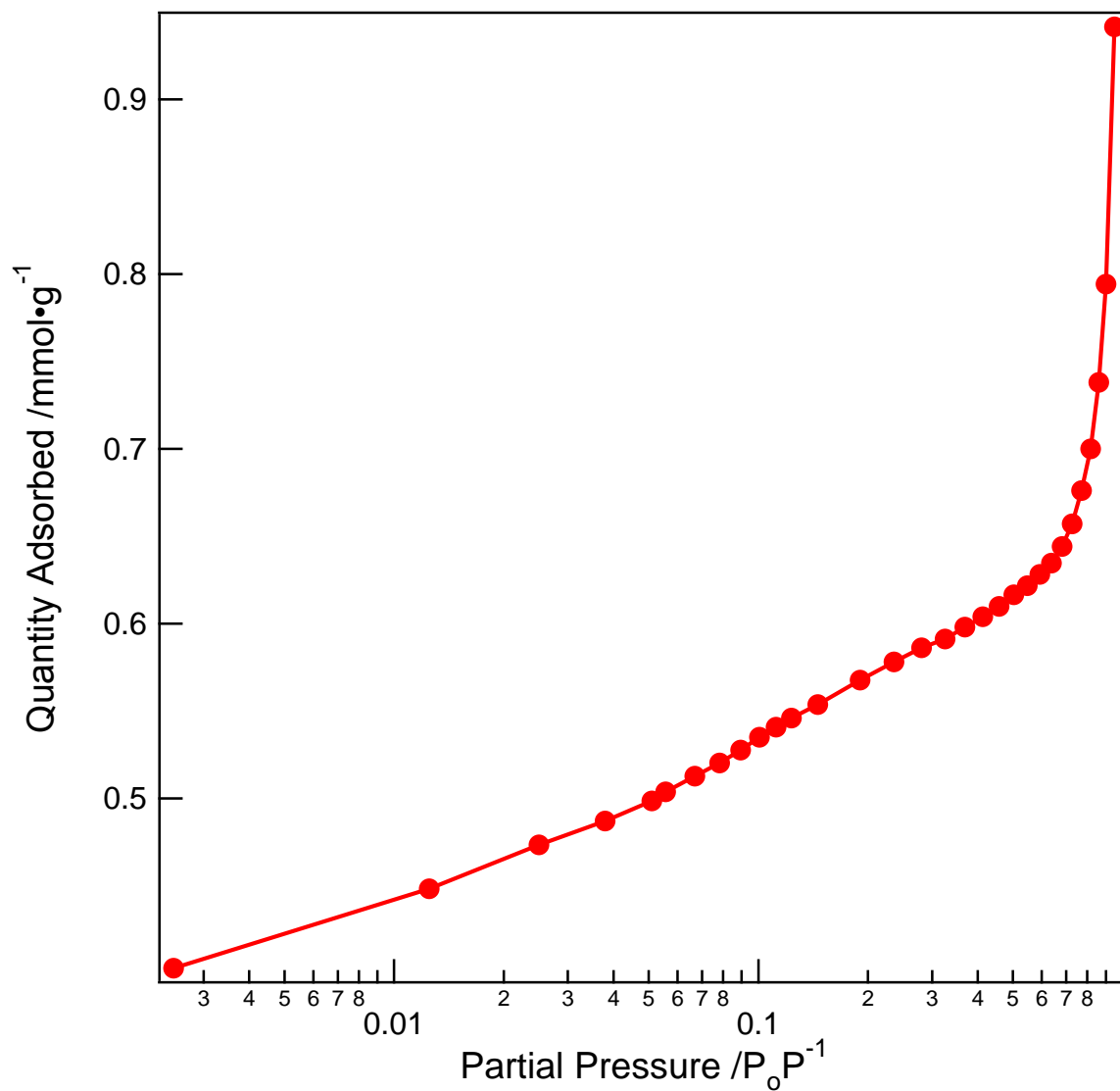
Figure 2.22. Logarithmic nitrogen adsorption isotherm at 77 K for sample A5 post-humidity treatment.

2.3.10 Sample B1

2.3.10.1 SEM-EDX

A Cu:Si loading ratio for sample B1 was determined to be 76:24, which is comparable to the values found for the MOF-74 samples. Results, summarized in Table 2.8, indicate a loading of 0.70 Si per Cu.

Table 2.8. Atomic % ratios of Cu to Si in sample B1, determined using various point and area-averaged EDX measurements.

	Cu	Si
Spectrum 1	58.39	41.61
Spectrum 2	59.37	40.63
Average Atomic %	58.89	41.11
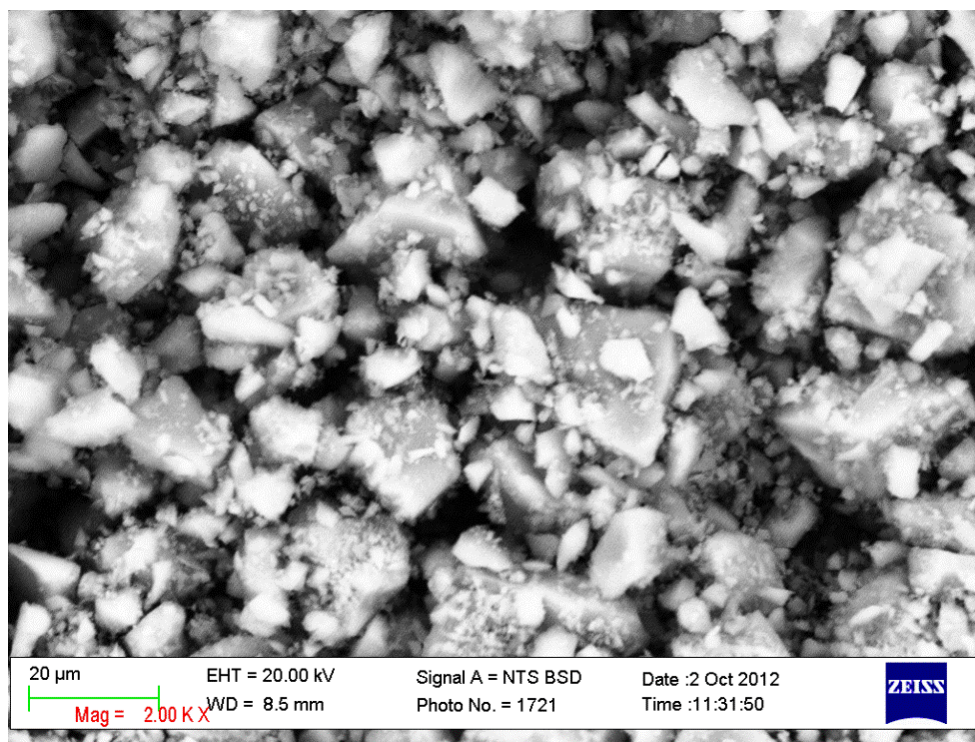
Figure 2.23. SEM image demonstrating homogeneity of Sample B1.

2.3.10.2 Solid-State NMR

The ^{29}Si NMR of B1 showed one sharp peak at -92 ppm. This indicates that the silica present is in the form of $[Si(OSi)_2(OR)_2]$.[52] Coupled with the EDX, this information gives a molecular formula of $[Cu_3BTC_2] \supset [SiO_3H_2]_{0.7}$.

2.3.11 Sample B2

The preparation of sample B2 differed from B1 due to the use of partial activation prior to the addition of TMOS. In order to determine if time dependent loading occurred with the silication procedure, EDX values were used to measure the ratio of Cu to Si. As seen in Table 2.9, it is clear that between one and 7 days, the amount of silica loaded remained un-changed

within error. This is indicative of a rapid uptake of the TMOS by the MOF. The results, however, indicate that less silica was loaded into sample B2 than sample B1. This could be due to the residual copper acetate found in sample B2, discussed in sections 2.2.8.2 and 2.3.12.2.

Table 2.9. Atomic % ratios of Cu to Si in sample B2, determined using EDX mapping.

	Cu	Si
Average 1 day	71.8232	28.1768
Average 3 days	67.63006	32.36994
Average 7 days	72.335	27.665

2.3.12 HKUST-1 Sample Comparison

The two silication methods resulted in equally homogeneous silication. Neither sample had external surface defects or indication of excess silica on the framework. Sample B2, however, resulted in a lower loading of silica, which is likely due to the presence of residual copper acetate as an impurity.

2.3.12.1 Crystallinity

All samples retained their crystallinity post-silication, as shown in Figure 2.24. This indicates that the silica does not have a preferential orientation within the HKUST-1, similar to the results seen in MOF-74. This also demonstrates that the samples are chemically stable to the silication process.
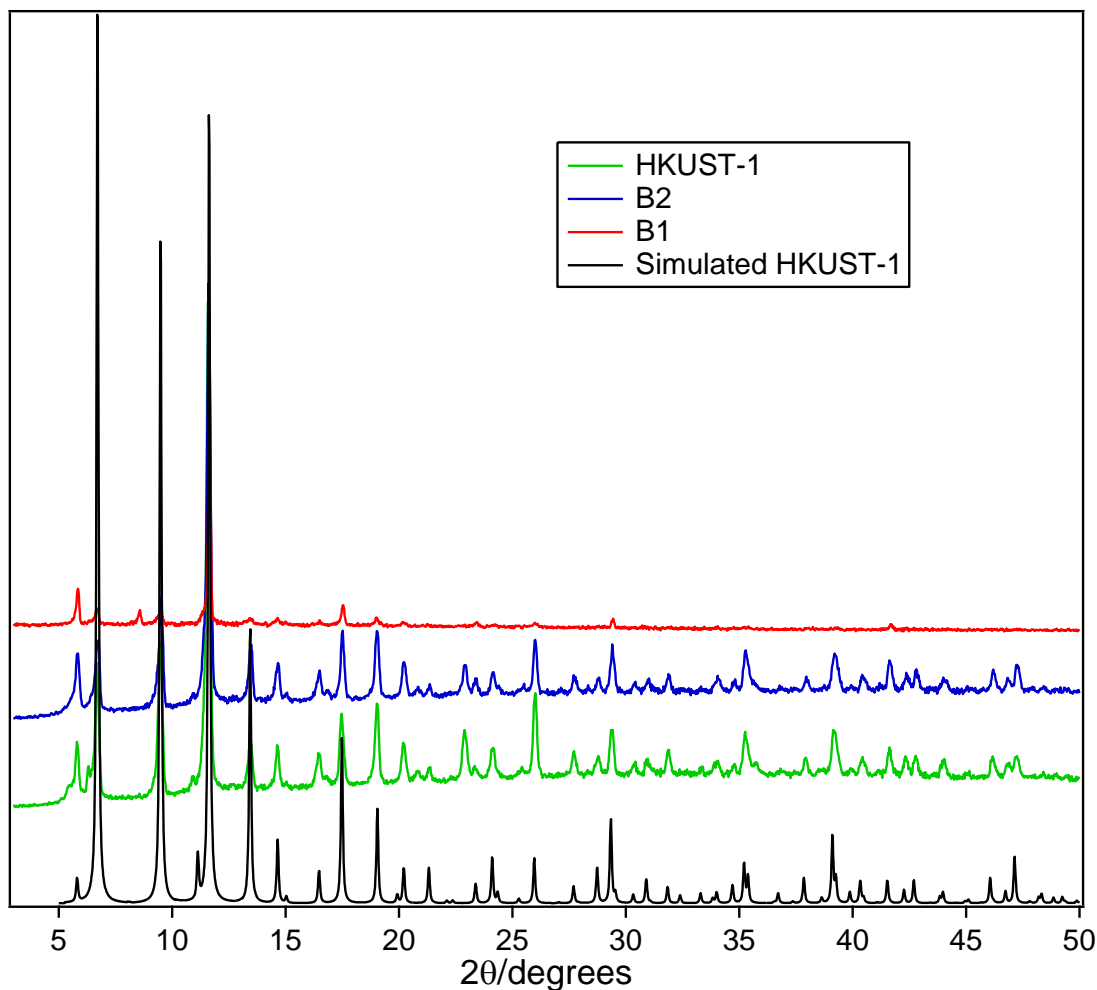
Figure 2.24. PXRD comparison of HKUST-1 to Samples B1 and A2. Simulated pattern obtained from literature crystal structure.[16]

2.3.12.2 Thermal Stability

The comparison of TGAs of B2 to HKUST-1 in Figure 2.25 shows an increase in thermal stability by 50°C. This result differs from that of MOF-74, which slightly decreased in thermal stability upon silication. This result points to the nature of the three-dimensional pore system in HKUST-1, which would allow for more even distribution of the silica. It appears that the silica

acts as a structural support for the HKUST-1. Conversely, in the MOF-74, the silica is more

likely to be localized close to the entrance of the pore due to the pore dimensionality and would

not be able to aid the MOF structurally. Blocked pores in MOF-74 would contain small amounts

of trapped water and methanol from the silication, which could pose a threat to the thermal

stability of the framework. Solvent within the blocked pores would be unable to escape from the

from the framework without partial degradation of the framework, and may be driven to react

with the metal-oxide bond. Notably, the sample used to make B2 contained a small amount (5%

by weight) impurity of $Cu(OAc)_2$. This impurity can be removed by rinsing with hot ethanol, as

discussed in section 2.2.7.
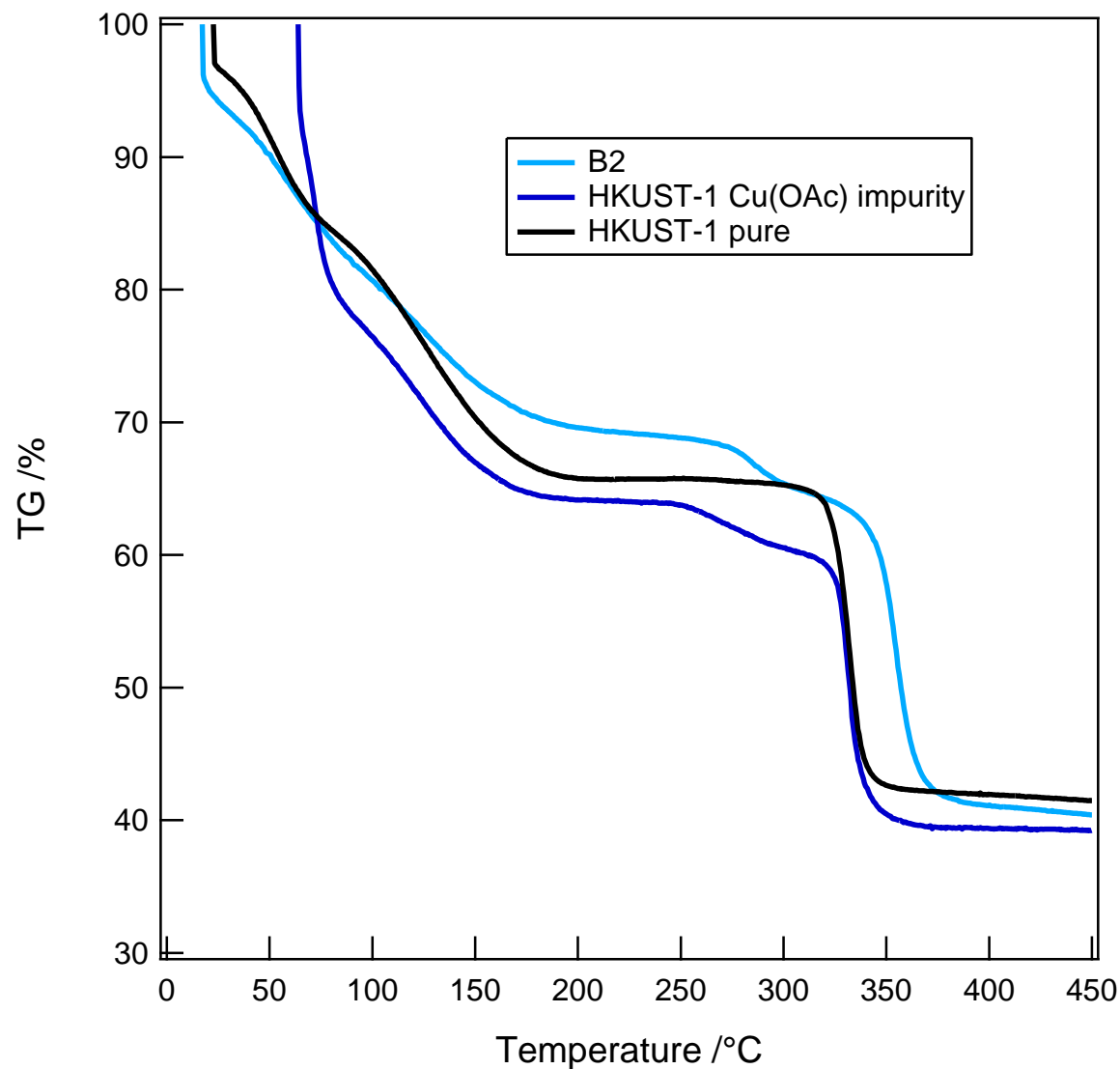
Figure 2.25. Thermal stability of HKUST-1 compared to B1, B2, and the HKUST-1 used in the synthesis of B2.

2.3.12.3 Nitrogen Adsorption

Nitrogen adsorption isotherms of B1 and B2 relative to HKUST-1 Figure 2.26 and Figure 2.27 show an equal decrease in uptake at both before and after the knee of the isotherm. This indicates that there is no preferential orientation of the silica relative to the bare metal sites, and

thus the silication follows a similar mechanism as discussed in section 2.3.9.3. The pore size distribution of the HKUST-1 in Figure 2.28 shows the presence of bimodal pores; the dip in distribution at 10.5 Å is due to the limits of the calculation selected, which is a non-linear density functional theory model designed for cylindrical pillared clays, as opposed to MOFs. Based on the distribution of B1 and B2, it is clear that B2 retains more of its porosity relative to B1 post silication. This indicates that B1 does, in fact, contain more silica than B2, which would justify the discrepancy in the obtained Cu:Si ratios between the two samples.
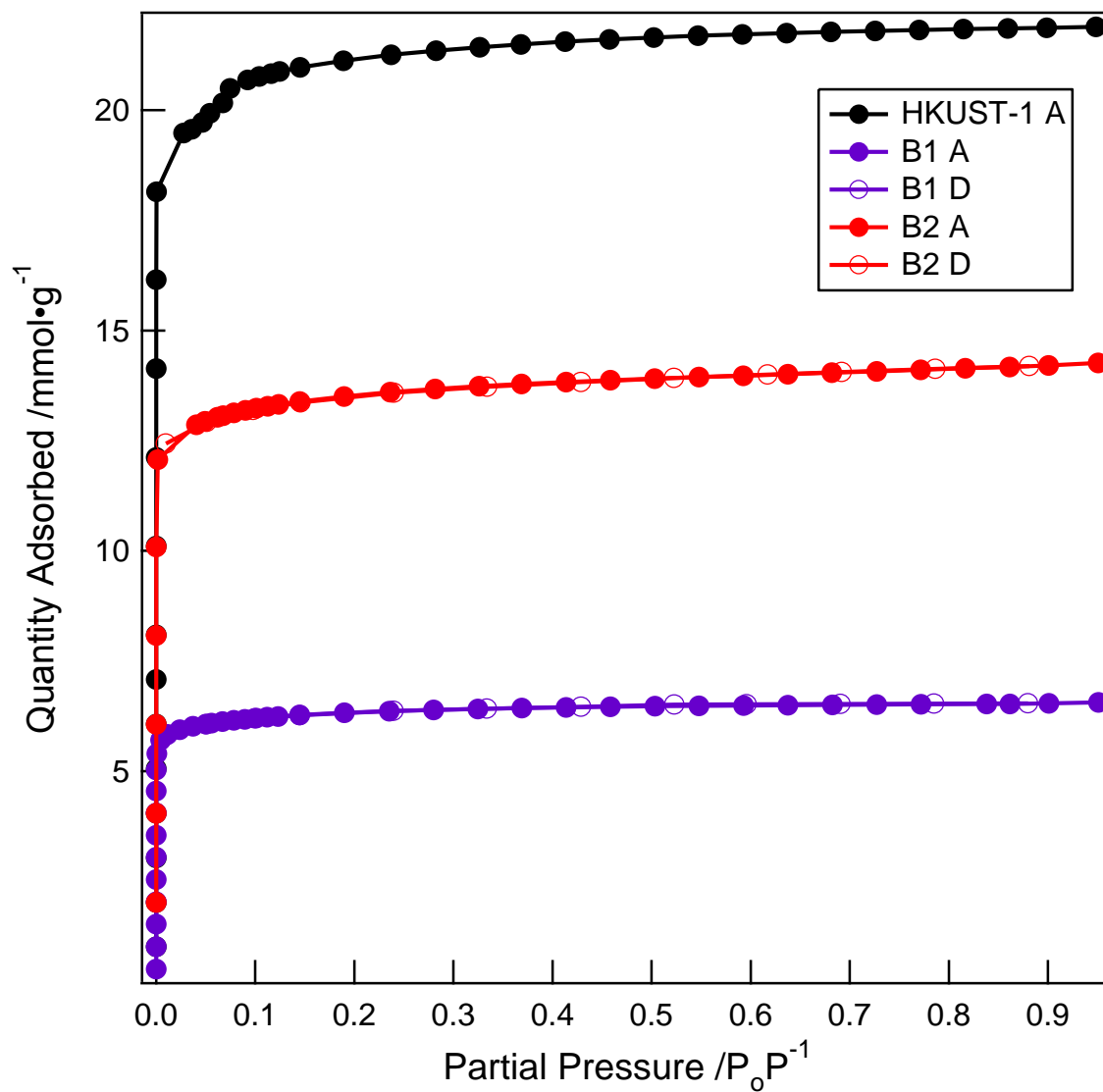
Figure 2.26. Linear nitrogen adsorption isotherm plot at 77 K comparing HKUST-1 to samples B1 and B2. A – adsorption; D – desorption.
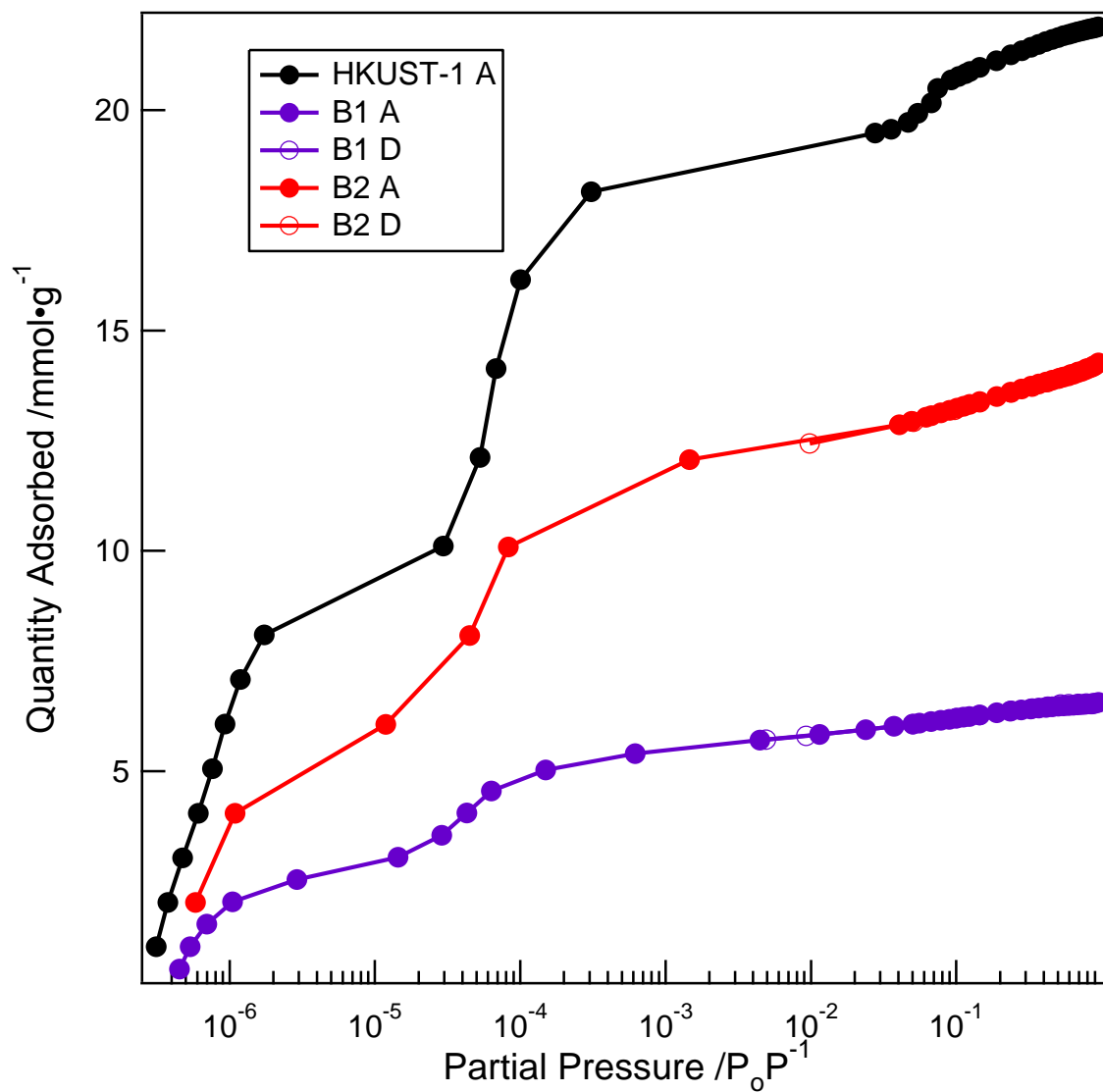
Figure 2.27. Linear nitrogen adsorption isotherm plot at 77 K comparing HKUST-1 to samples B1 and B2. A – adsorption; D – desorption.
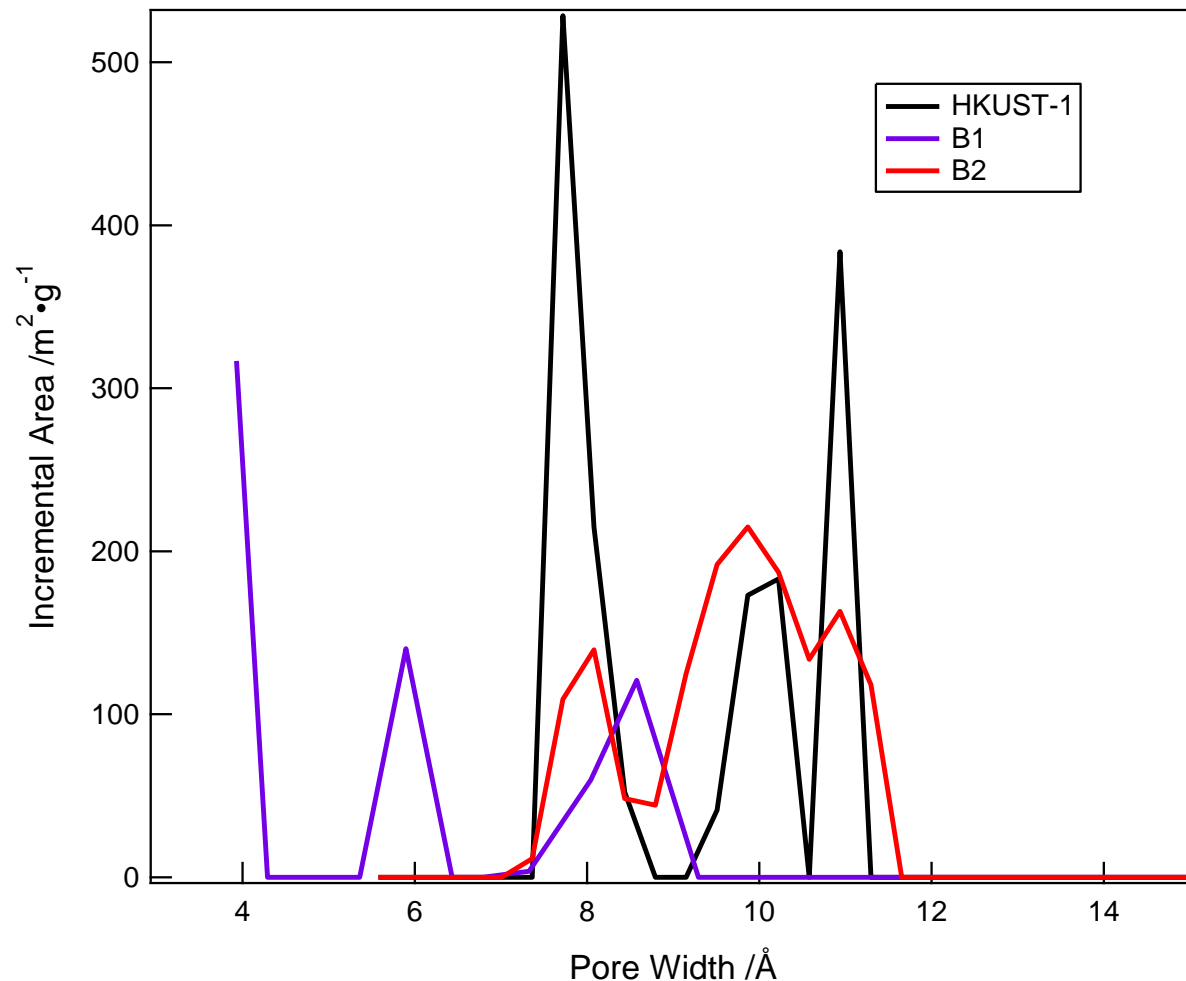
Figure 2.28. Calculated pore size distribution plot, comparing HKUST-1 to samples B1 and B2.

2.3.12.4 Carbon Dioxide Adsorption

Carbon dioxide adsorption isotherms were collected for sample B1 at temperatures 263 K and 273 K, which were used to calculate the heat of adsorption. As shown in Figure 2.29, the sample has a high $-Q_{st}$ value (32.2 kJ/mol) similar to the literature value of HKUST-1.[46] The

heat of adsorption drops off over the course of the isotherm, due to filling of high energy sites of the sample. The calculated adsorption coincided well with the measured values.
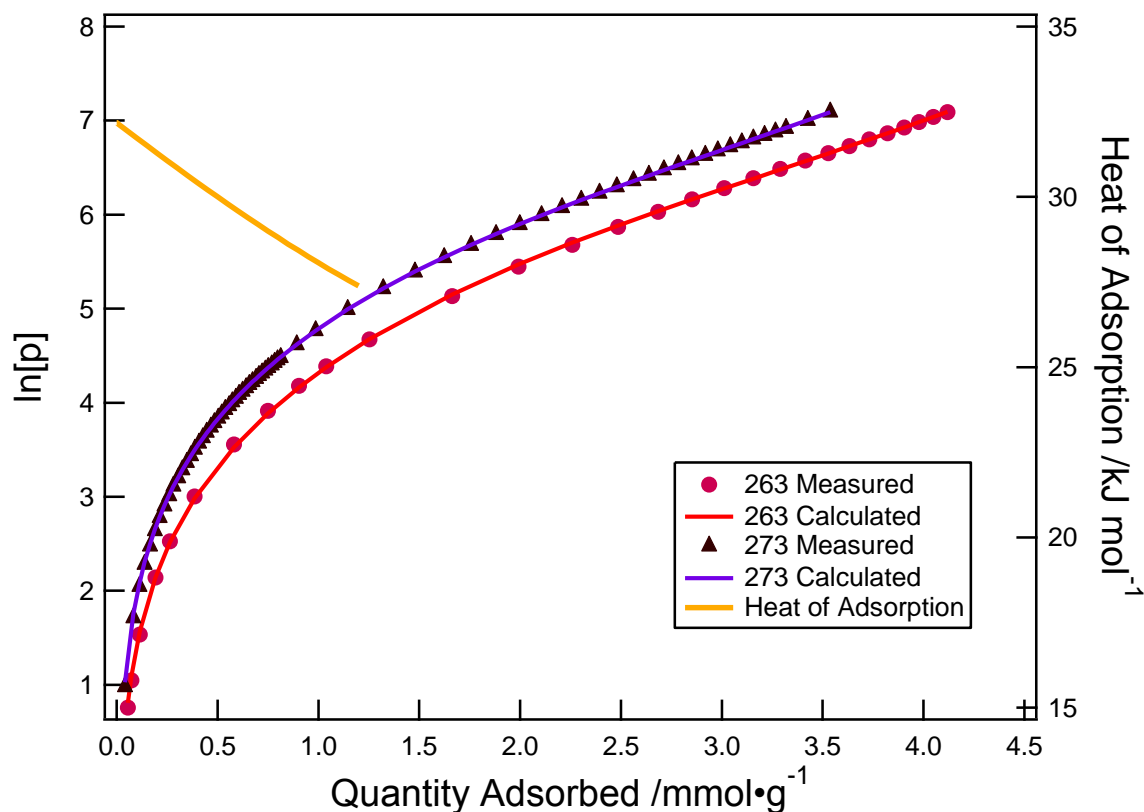
Figure 2.29. Carbon dioxide adsorption isotherms of sample B2 at 263 K (red) and 273 K (violet) and the HOA (orange), fitted using a virial model.

2.3.12.5 Water Stability Experiment

Over the course of the water stability experiment, PXRDs of both the tested B2 and HKUST-1 matched initial powder patterns. Notably, both samples changed colour to a lighter blue over the course of the experiment, which has been suggested by Cychosz and coworkers to

indicate the breakage of metal-ligand bonds in the framework.[35] Unlike Cychosz and coworkers, however, there was no indication of new peak formation over the course of the experiment.
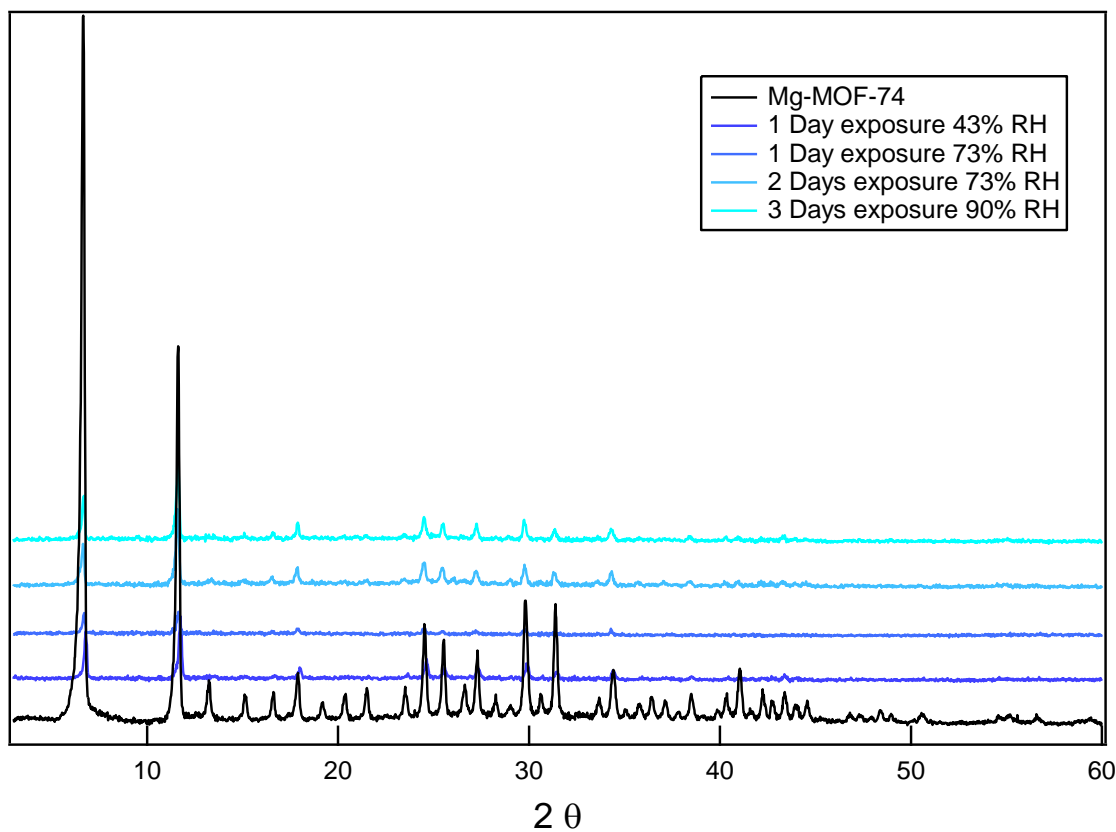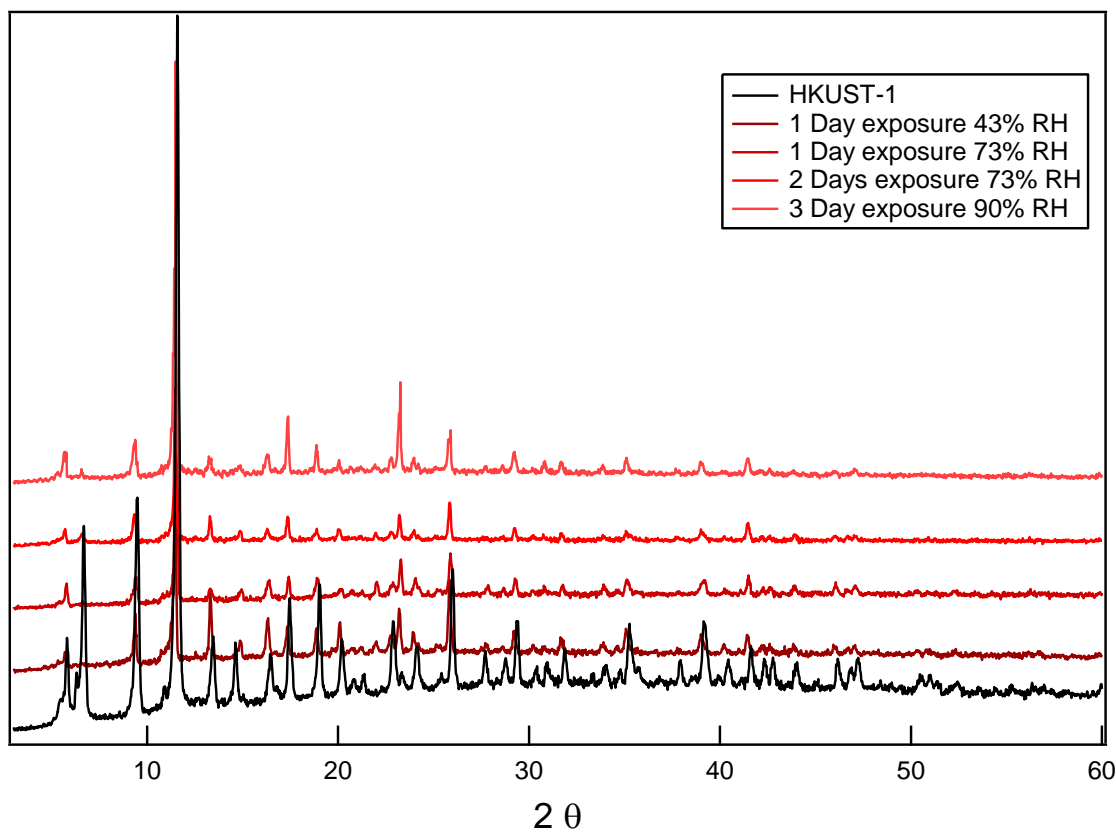

Figure 2.30. PXRD patterns comparing HKUST-1 over the course of the water stability experiment.
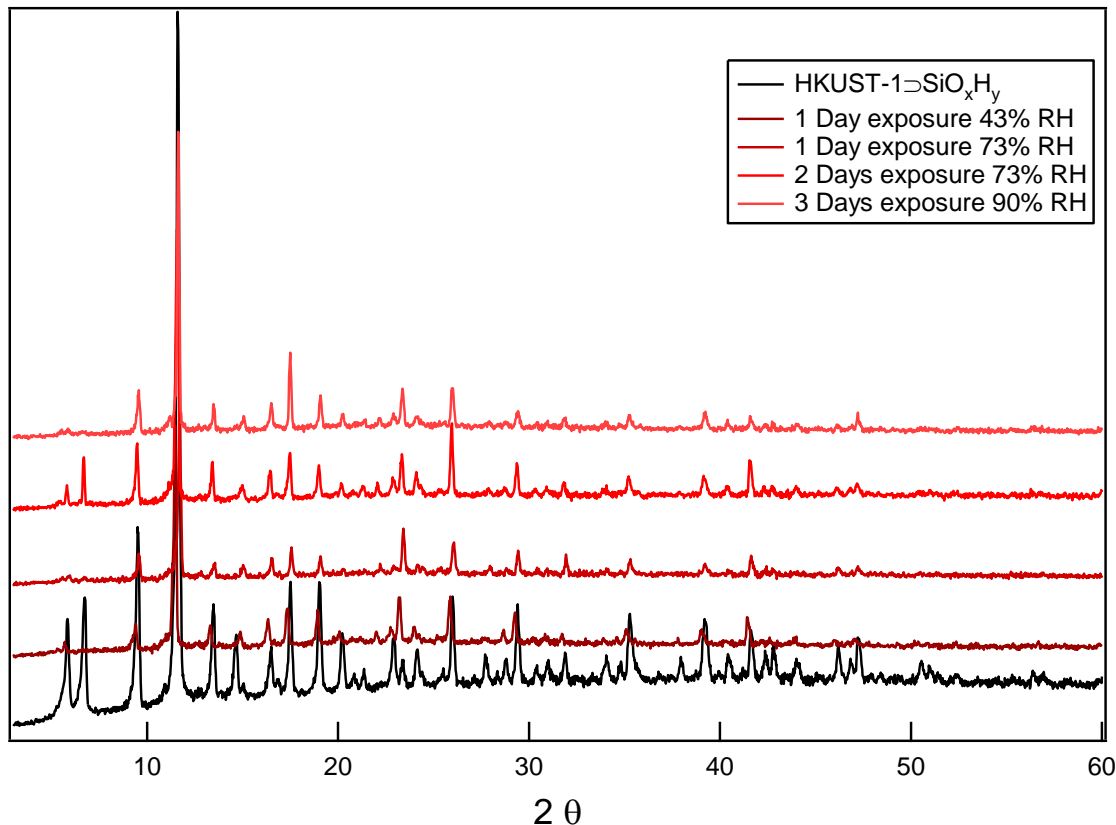
Figure 2.31. PXRD patterns comparing sample B2 over the course of the water stability experiment.

In order to better understand the system, nitrogen adsorption isotherms were taken post water stability experiment, shown in Figure 2.32. A comparison between the pre- and post-water treated B2 sample indicates that 100% of the porous structure was retained. The water-treated sample did, however, release two different sublimate bands, one of which was copper acetate, which collected as a thin film on the side of the ASAP tube. The second band, which collected in the cold trap of the ASAP 2020, can be attributed to the release of 1,3,5-benzenetricarboxylic acid upon framework decomposition.[20] Unfortunately, the comparison sample of water-treated HKUST-1 also released a small amount of sublimate, despite rinses with

hot ethanol as an attempt to mitigate sublimation. The data from the HKUST-1 was, thus, not

collected for comparison.
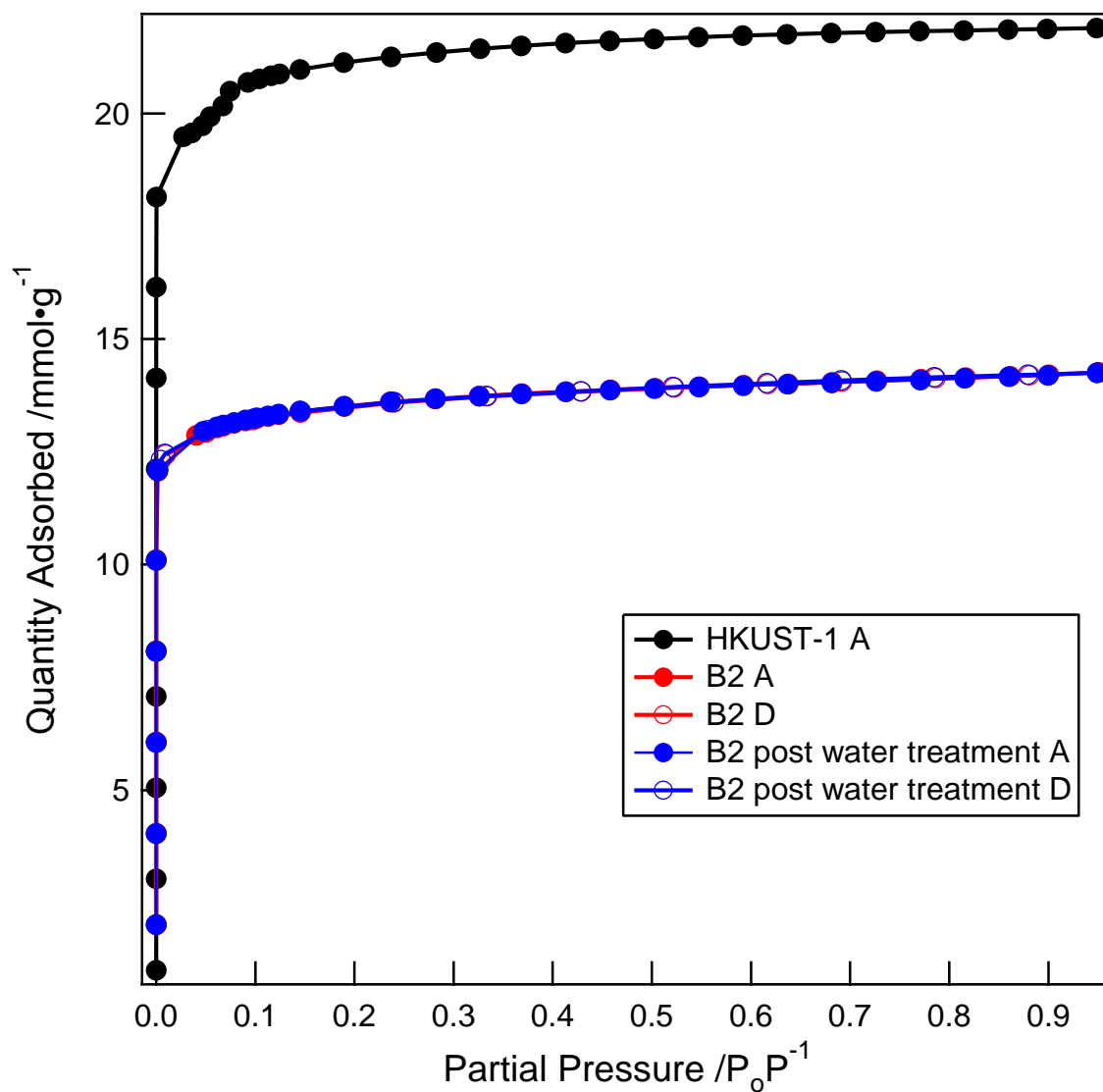
Figure 2.32. Linear Nitrogen isotherm plot comparing HKUST-1 and sample B2 to post water treated B2. A – adsorption; D – desorption.
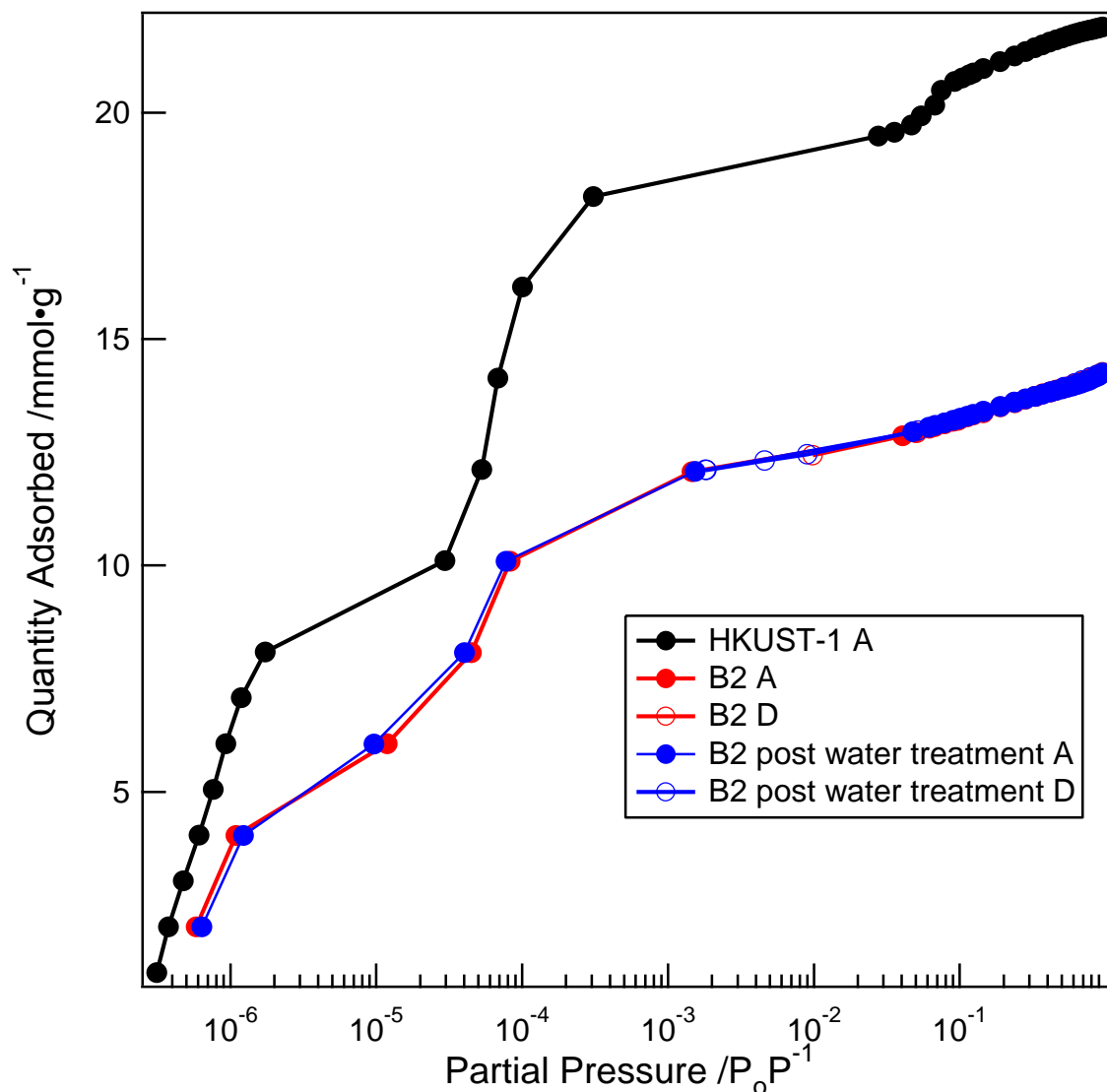
Figure 2.33. Logarithmic Nitrogen isotherm plot comparing HKUST-1 and sample B2 to post water treated B2. A – Adsorption; D – desorption.

2.3.13 Comparison between Silicated Materials

2.3.13.1 Reproducibility of Silication

In both MOF systems, a reproducible method of silication is evident. Samples produced by the TMOS immersion method resulted in fairly even loadings of silica, which functionalized

the materials at the molecular level in all cases, save for A1. It appears that the silica is randomly oriented within the MOF pores in both the Mg-MOF-74 and the HKUST-1, and thus does not negatively influence the heat of adsorption in either case. The state of the silica within the MOFs was also found to be fairly reproducible. In all cases, the silica was partially cross-linked, which indicates that the Lewis acidity of the MOF pores in both cases is enough to catalyze the reaction of TMOS with water.

2.3.13.2 Time Dependence of Silication

In sample B2, it was determined that a maximum loading of silica could be obtained after 1 day of synthesis. Sample A5, on the other hand, requires a greater amount of time for silica loading to occur, due to the kinetics of a one-dimensional porous system, though it is plausible that an even distribution is not obtained in A5.

2.3.13.3 Water Stability Experiment

The water stability experiments yielded extremely interesting results. There was a large contrast in behaviour between the samples A5 and B2, in which the former completely lost its porosity after water treatment, whereas the latter was virtually unaffected by the water treatment. The main difference between the two frameworks is their dimensionality. Although both MOF-74 and HKUST-1 decompose by cleavage of the M-O linkages within the framework, there are slight differences in their response to water treatment. In the case of MOF-74, pore blocking can rapidly decrease the accessible inner surface area, with only the cleavage of surface molecules. On the other hand, when HKUST-1 decomposes, its inner surface remains accessible until total

pore collapse, due to the inherent nature of a three-dimensional porous system. HKUST-1 is known to decompose via a ligand displacement reaction, shown in Figure 2.34.
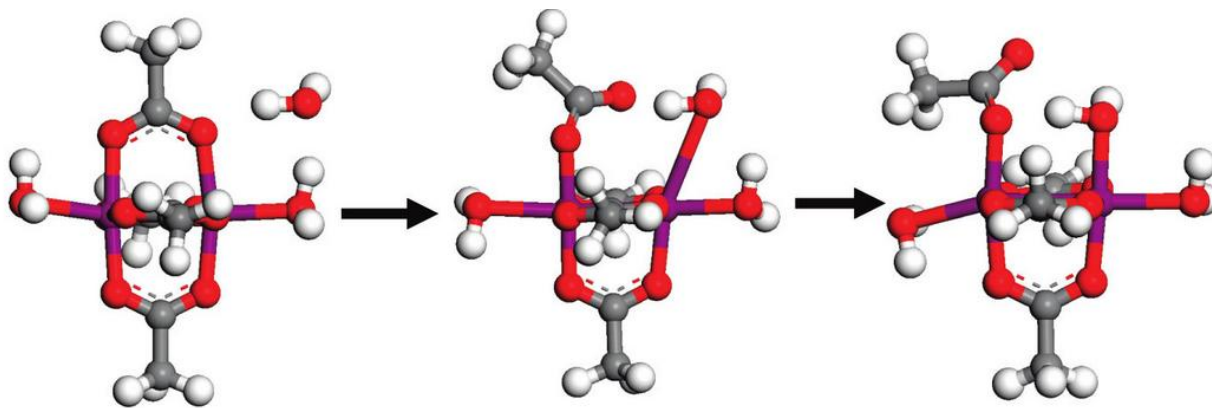
Figure 2.34. Modelled ligand displacement within the Cu-paddlewheel cluster of HKUST-1. Reprinted with permission from (Low, J.; Benin, A.; Jakubczak; *et. al*. *J. Am. Chem. Soc.* **2009,** *131***, 15834-15842). Copyright (2009) American Chemical Society** [20]

This decomposition is initiated by the hydrogen bonding interactions between water and the metal cluster. In order for the silica to have an effect on the structural stability, it would have to either (a) offer a competing site of hydrogen bonding to prevent water from accessing the metal sites, or (b) act as a structural pillar, again through hydrogen bonding interactions, to keep decomposed clusters from producing a collapsed structure. The experimental results do not provide an indication towards which mechanism takes place, however. Future modelling experiments and comparisons to different MOFs that contain the copper paddlewheel structure are needed in order to determine the process of silica framework stabilization.

2.4 Conclusions

The two different carboxylate MOFs, Mg-MOF-74 and HKUST-1 were functionalized with silica in order to increase water stability. In the case of Mg-MOF-74, the high heat of adsorption of 65.4 kJ/mol was retained, determined by carbon dioxide sorption at two different temperatures. This value was higher than literature (43 kJ/mol),[46] due to the fit used on the isotherm. The nitrogen sorption isotherms after a water stability experiment indicated that the silicated Mg-MOF-74 was not water stable.

In regards to the HKUST-1, the sample also retained its high heat of adsorption, at 32.2 kJ/mol.

Adsorption isotherms were used to confirm the presence of silica within MOF pores, while EDX was used to confirm sample homogeneity and reproducibility of the silication reactions. Rough molecular formulas were determined through a combination of EDX and solid-state Si-NMR. When exposed to water, both the silicated HKUST and Mg-MOF-74 retained their crystallinity. Nitrogen adsorption data was used to determine that silicated sample of MOF-74 lost its porosity, whereas silicated HKUST-1 retained porosity. Two mechanisms of silica stabilization were postulated, in which silica could either prevent water from coordinating to the metal centre, or could act as a structural pillar to a partially decomposed framework.

Chapter Three: **Phosphonate Hollow Spheres**

3.1 Introduction

3.1.1 Metal-Organic Polyhedra (MOPs)

Spherical MOPs have been produced with a variety of rigid ligands that undergo

predictable coordination to various metals. Ligands used to form discrete cluster assemblies

have similarities to the design principles used in MOFs. The formation of discrete clusters can

take two different approaches. Firstly, one can use a capped metal to introduce a bend in the

overall coordination shape, such as the example mentioned in section 1.2. Another approach is

to make use of bent ligands. A study conducted by Furukawa and coworkers demonstrated the

difference between such ligands by comparing the reactivity of bent and linear dicarboxylates

with copper(II). All of the ligands reacted with the copper to form a characteristic copper

paddlewheel metal cluster, pictured in Figure 1.2. In the case of ligands with a 120° bend, the

resulting structures were clusters composed of 12 metal clusters, such as MOP-1 shown in Figure

3.1.
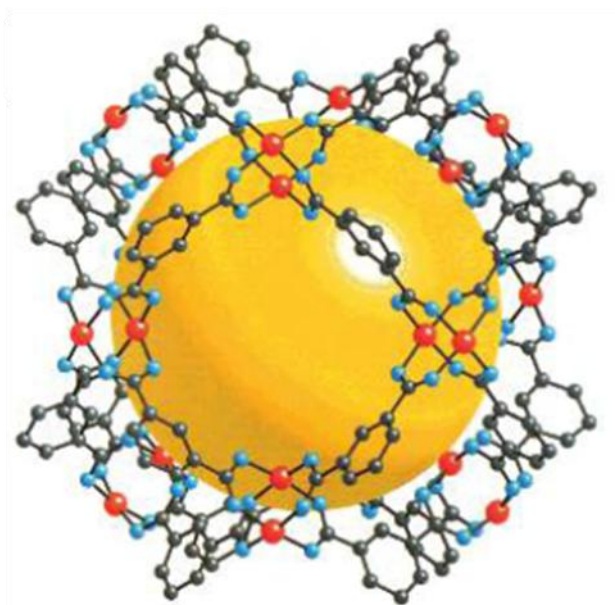
Figure 3.1. MOP-1. Cu – red, O – blue, C – black. Reprinted with permission from (Eddaoudi, M.; Kim, J.; Wachter, J. B.; Chae, H. K.; Yaghi, O. M. *J. Am. Chem. Soc*. 2001 *123*, 4368–4369). Copyright (2001) American Chemical Society.[62]

On the other hand, the use of ligands with a 90° bend caused the formation of a truncated cuboctahedron, a structure with 9 verticies.[63] Another example of the role of the linker angle was demonstrated by Bunzen and coworkers.[3] Ligands of angles varying between 127° and 149°, such as the two pictured in Figure 3.2**Error! Reference source not found.**, were produced and complexed to investigate the formation of the $M_{24}L_{48}$ polyhedron, pictured in Figure 3.3. Theoretical calculations indicated that this polyhedron is favoured when linkers are between 134° and 149°. Experimentally, this was proven to be the case. Even ligand (**5**), with an angle of 135°, formed exclusively the $M_{24}L_{48}$ cluster, demonstrating that the clusters are a supramolecular assembly. On the other hand, ligand (**4**) formed exclusively $M_{12}L_{24}$.
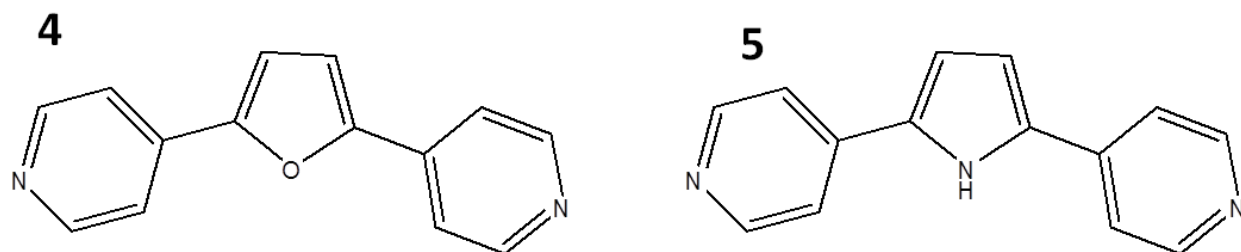
Figure 3.2. Ligands 4 (127°) and 5 (135°) used to form M$_{12}$L$_{24}$ and M$_{24}$L$_{48}$, respectively.[3]
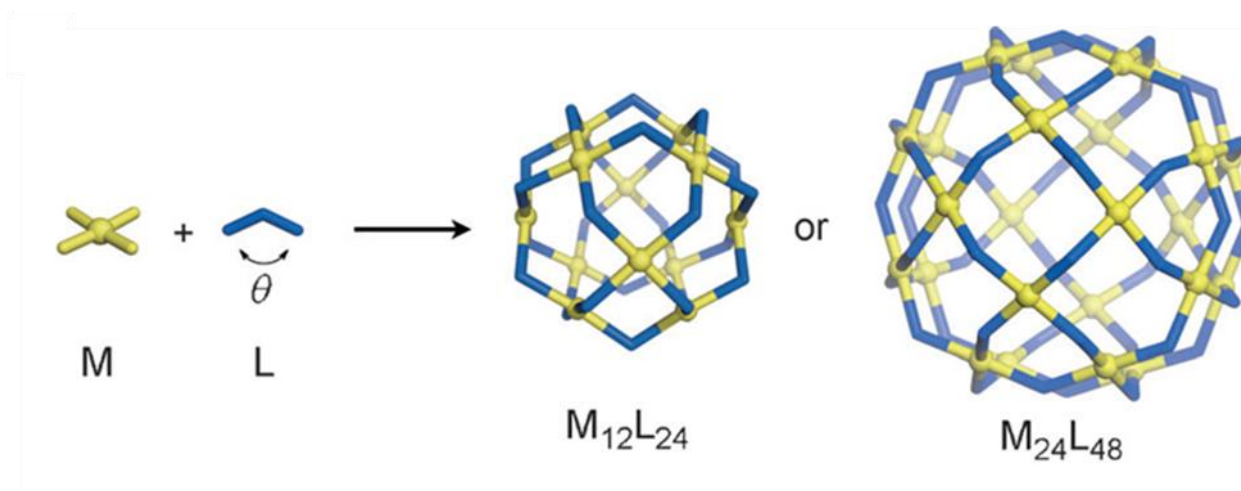
Figure 3.3. Angle-dependent synthesis of M$_{12}$L$_{24}$ and M$_{24}$L$_{48}$. Reprinted with permission from (Bunzen. J.; Iwasa, J.; Bonakdarzadeh, P.; *et al.; Angew. Chemie. Int. Ed.* **2012,** *51,* **3161–3163). Copyright (2012) John Wiley and Sons.**[3]

The potential applications of MOPs are limited by their size, which falls in the nanometre range. The small size is advantageous for small molecule encapsulation, and for catalytic activity, however larger hollow spheres are necessary to encapsulate larger systems.

3.1.2 MOF Microspheres

MOF microspheres are hollow spheres made up of MOF nanocrystals that are templated or directed into a spherical growth that would otherwise not be thermodynamically favoured.

These spheres are of interest as the intrinsic porosity of the MOF with the added hollow inner surface can create a highly functional semi-permeable membrane. There are, however, only a handful of examples of these materials in the literature, as they are challenging to produce. There are three main methods of directing the formation of hollow spheres in MOFs: the use of a spherical template, interfacial synthesis, and finally spray-drying.

3.1.2.1 Templating

Templating is one of the most common methods used to make hollow metal-oxide spheres, as it can produce structures which are highly uniform in size, however the templates themselves require added synthetic steps to produce which can drive up the cost[64] and the templates must be excised from the spheres. In the case of MOF microspheres, there is an added problem of the template removal conditions degrading the MOF itself. This problem has plagued the synthesis of hollow spheres of Prussian blue analogues which are frameworks made up of cyano-bridged metals.[65] A block-copolymer template used by Roy and coworkers was inseparable from hollow spheres produced, resulting in hollow hybrid spheres. On the other hand, Lee and coworkers were able to use a carboxylate-terminated polystyrene template to grow ZIF-8 hollow spheres.[66] The template in the latter example was removed by dissolution in DMF.

3.1.2.2 Interfacial Synthesis

Interfacial synthesis was first employed by Ameloot and coworkers to successfully obtain HKUST-1 hollow spheres.[67] Interfacial synthesis involves the use of two immiscible liquids, one with dissolved metal and the other with dissolved ligand. These liquids are combined in such a way that droplets of one liquid form in the other, while the reaction occurs at the interface

of the liquids. The advantage of this technique is that the resulting spheres can be large in size, such as the 400 μm spheres formed in the above example. Ameloot and coworkers used a syringe-pump to properly control droplet size within the emulsion. The major synthetic challenge to this technique, however, is the need for immiscible solutions, thus the solubility properties of metal and ligand must be different.

3.1.2.3 Spray Drying

Spray-drying is a technique that was recently developed to construct MOF microspheres with a variety of MOFs.[68] Spray-drying involves mixing a metal and a ligand solution immediately prior to ejection via an atomizer, to produce microdroplets of the MOF reagents. As the microdroplets fly through the air, they partially evaporate causing an increase in surface concentration. With increasing surface concentration, a thin layer of solidified reagents forms, which acts as a nucleation site during further evaporation of the particle. Upon complete reaction, hollow microspheres are formed. The major drawback with this method of hollow sphere formation is the resulting stability of the microspheres. Upon sonication, it was reported that the HKUST-1 sphere broke into its nanocrystalline components and lost its macrostructure. It remains unclear whether all MOF microspheres have the potential to degrade with sonication or just spheres produced by spray-drying.

3.1.3 Phosphonate MOFs

MOFs produced with phosphonate ligands are of interest due to their high chemical and water stability. Phosphonic acid is a three-dimensional acid group with two potential sites of deprotonation, with a pK_{a1} and pK_{a2} of < 2 and 2.6, respectively.[69] The potential dianionic

nature of phosphonic acids produces a stronger bond to metals than carboxylic acids, which is the key factor behind the robust frameworks produced with these ligands. The three-dimensional nature of phosphonates, however, favours the production of metal-phosphonate layers in which the phosphonate bridges two or more metal centres. The first examples of porous phosphonate frameworks involved the use of methylphosphonates, in which the methyl groups direct formation of the pores as they are too small to pillar layers.[70–72] An example, shown in Figure 3.4, is a copper (II) methylphosphonate that contains one-dimensional channels of approximately 3 Å in size.[70] In the case of linear bisphosphonate ligands, the phosphonate groups typically form layers that are propped apart by the pillaring organic backbone of the ligand.[73]
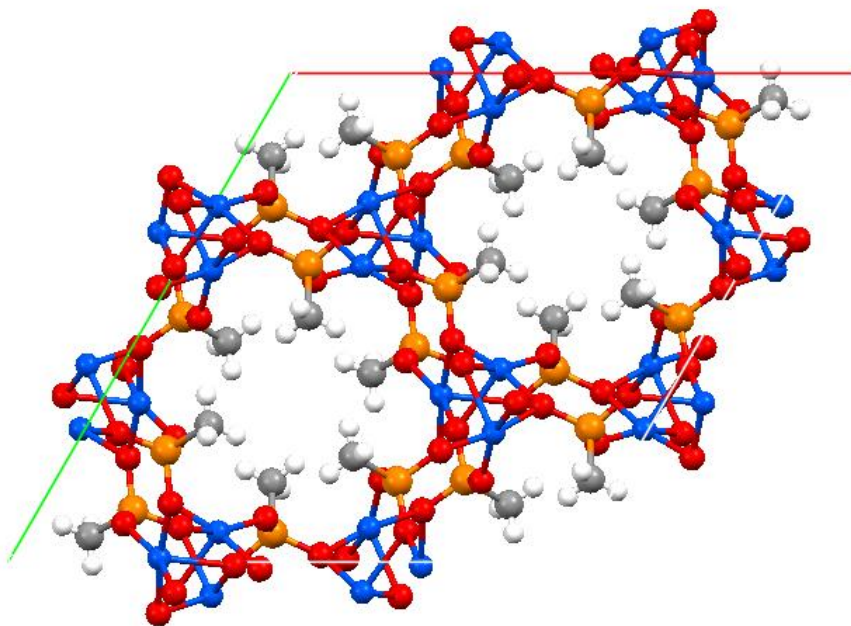
Figure 3.4. Crystal structure of β-Cu(CH$_3$PO$_3$).[70] Cu – blue, P – orange, O – red, C – grey, H – white.

In this chapter, the correlation between shape and structure will be investigated. A new ligand introduced in this chapter, (6) 2,7-fluorene(bisphosphonic acid) (Et$_2$H$_2$BPF), shown in Figure 3.5, has been used to see if the bent nature will disfavour the pillared-layered topology that is common among linear bisphosphonate ligands. The original hypothesis was that the angle of the ligand would favour either a one-dimensional large-pore system or a densely packed framework with interesting coordination. This ligand instead resulted in micrometre-sized hollow spheres, which is a unique morphology for a phosphonate material and has many potential applications.
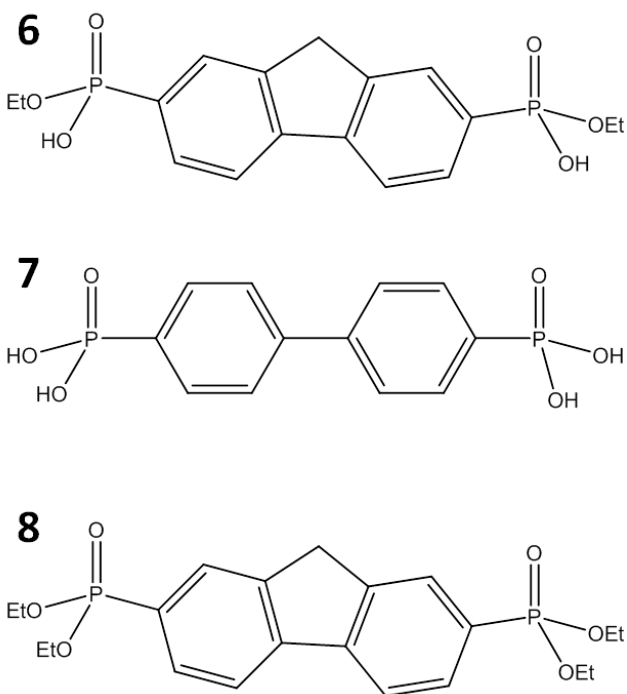
Figure 3.5. Ligands (6) Et$_2$H$_2$BPF, (7) H$_4$BPF, and (8) Et$_4$BPF, used to form hollow phosphonate CALF balls

3.2 Experimental

3.2.1 Instrumentation

All reagents were obtained from Sigma-Aldrich and used without further purification. Instrumentation was used as described in section 2.2.1 Instrumentation with the addition of the following instruments:

UV-vis: a UV-visible spectrum was obtained of the solid CALF-B1 using a Carey 500 UV-Vis spectrometer. Sample was placed between two glass microscope slide covers, and the covers were then taped together. Two separate slide covers were taped together to serve as a blank. A background correction was run on the glass slides, and then a spectra was collected between 800 and 300 nm of the spheres. The background was subtracted from the spectra separately.

Single-crystal X-ray diffraction patterns were obtained at 173 K using a Bruker SMART APEX II CCD x-ray diffractometer with CuKα radiation.

Microscopy: spheres were analyzed visually using a LEICA MS 5 optical light microscope, with a field of view of 5.5 mm at the highest level of magnification. Colour images of spheres were obtained using an 8.0 mp Cannon PowerShot A590IS. Pictures were acquired using a macro focus setting at 4.0x optical zoom, aligned into the microscope.

3.2.2 Synthesis of 2,7-dibromofluorene

Synthesis was modified based on a literature procedure.[74] To a clean, two-neck round-bottomed flask, fluorene (15.775 g, 91 mmol) and a stir bar were added. A condenser and an addition funnel were attached to the flask then set up over an oil bath. Chloroform (82 mL) was added through the addition flask and the mixture was stirred to dissolve the fluorene. To the addition funnel, a mixture of chloroform (20 mL) and bromine (18 mL, 113 mmol) was added.

Prior to addition, the apparatus was covered in foil. The bromine mixture was added dropwise, and the reaction was carried out for a total of 19 hours. The reaction mixture was vacuum filtered over an aqueous $Na_2S_2O_3$ solution (0.05 g/mL), rinsing with 95% EtOH. A solid white product was collected (6.360 g, 19.6 mmol) with a percent yield of 20.7%. Purity was confirmed by GC-MS (m/z = 324). ^{1}H NMR (400 MHz in CDCl$_3$) chemical shifts in ppm: δ: 7.67 (2H s), 7.60 (2H d), 7.50 (2H d), 3.87 (2H, s).

3.2.3 Synthesis of 2,7-bis(diethylphosphono)fluorene (Et₄BPF)

A stir bar and NiBr$_2$ (1.325 g, 6 mmol) were activated under vacuum by heating with a heat gun. The flask was cooled, exposed to argon atmosphere, and 2,7-dibromofluorene (5.006 g, 15.4 mmol) was then added to the flask. The flask was equipped with a condenser and an addition funnel, to which 1,3-diisopropyl benzene (50.0 mL) was added. Enough solvent was added to the reaction mixture to cover the solids (approximately 10 mL), then the reaction mixture was brought to reflux while stirring. Triethyl phosphite (10.0 mL, 60.1 mmol) was then added to the remaining liquid in the dropping funnel, and the solution was added to the reaction at a rate of one drop per three seconds. The reaction was refluxed overnight, then was removed from heat and vacuum filtered, rinsing with chloroform. The filtrate was distilled under vacuum to remove solvent. Solid was dissolved in minimal chloroform, and filtered through a silica plug. The silica was rinsed with chloroform and acetone, and the solvents were evaporated. Solid was purified by recrystallization in ether, and was cooled then vacuum filtered to obtain a pure white product (5.144 g, 11.7 mmol) with a percent yield of 75.9%. NMR spectra were acquired in DMSO-d6 with a TMP internal standard. ^{31}P NMR (400 MHz in DMSO-d6) chemical shifts in ppm: δ 19.58. ^{1}H NMR (400 MHz in DMSO-d6) chemical shifts in ppm: δ 8.16 (2H q), 7.97 (2H

d), 7.77 (2H q), 4.12 (2H, s), 4.04 (8H, m), 1.25 (12H, t). Analytical calculated based on the molecular formula of $C_{21}H_{28}O_6P_2$, 438.14 g/mol: C 57.53%, H 6.40%. Actual: C 57.7%, H 6.28%.

3.2.4 Accidental Synthesis of 2,7-bis(ethylphosphono)fluorene, (Et₂H₂BPF)

A sample of monoester was accidentally obtained as a major reaction product of an incomplete acidification. Tetraethyl-2,7-fluorenebisphosphonate ester (4.269 g, 9.7 mmol) was refluxed in 6 M HCl (51.0 mL) overnight. The reaction was then removed from heat and the majority of solvent was removed by rotary evaporator. The wet product was filtered, rinsing with water (approx. 50 mL), leaving overnight to dry. A white powdery solid was obtained (2.901 g, 7.6 mmol, 77.9 % yield based on monoester).   Impurities in the NMR indicated a partial hydrolysis, however, the product was used as-is. ^{31}P NMR (400 MHz, DMSO-D6) chemical shifts in ppm: δ 19.48, 16.53, 14.27. The first peak listed corresponds to the full ester, and was only a very small impurity. The latter two peaks correspond to the monoester and the full acid, respectively, and were found in approximately a 2:1 ratio of monoester to acid. Analytical calculated based on the molecular formula of $C_{17}H_{20}O_6P_2$, 382.28 g/mol: C 53.4%, H 5.27%. Actual: C 51.53%, H 4.76%. The discrepancy corresponds to the presence of the full acid in the product.

3.2.5 Synthesis of 2,7-bis(ethylphosphono)fluorene, (Et₂H₂BPF)

Pure monoester was produced to verify results in the CALF-B2 synthesis. Tetraethyl-2,7-fluorenebisphosphonate ester (0.567 g, 1.2 mmol) was refluxed in NaOH (6 eq, 0.288 g, 7.2

mmol) in water (50 mL) overnight. The reaction was then removed from heat and acidified

using 10% $HCl_{(aq)}$ until the solution reached a pH of approx. 1.0. The solution was evaporated

using an air flow overnight, yielding a yellow solid residue. The solid was dissolved in

isopropanol and filtered to remove salt impurities. The isopropanol solution was removed by

rotary evaporator, yielding a white solid (0.133 g, 26.9% yield). ^{31}P NMR (400 MHz in DMSO-

d6) chemical shifts in ppm: δ 16.58. ^{1}H NMR (400 MHz in DMSO-d6) chemical shifts in ppm: δ

8.08 (2H q), 7.93 (2H d), 7.74 (2H q), 4.07 (2H, s), 3.91 (4H, m), 1.20 (6H, t), 1.04 (2H, d).

Analytical calculated based on the molecular formula of $C_{17}H_{20}O_6P_2$, 382.28 g/mol: C 53.4%, H

5.27%. Actual: C 51.38%, H 5.00%.

3.2.6 Synthesis of 2,7-fluorene(bisphosphonic acid, (H₄BPF)

Tetraethyl-2,7-fluorenebisphosphonate ester (2.787 g, 6.4 mmol) was refluxed in 6 M

HCl (51.0 mL) overnight. The reaction was then removed from heat and the solvent was

removed by rotary evaporator. The wet product was filtered, rinsing with 6M HCl (approx. 50

mL), leaving to dryness. Product was recrystallized in MeOH, yielding a white solid (1.555 g,

4.7 mmol) with a percent yield of 75%. ^{31}P NMR (400 MHz in DMSO-d6) chemical shifts in

ppm: δ 14.53. ^{1}H NMR (400 MHz in DMSO-d6) chemical shifts in ppm: δ 8.02 (2H q), 7.91 (2H

d), 7.73 (2H q), 4.03 (2H, s), 4.04 (8H, m), 1.25 (12H, t). Analytical calculated based on the

molecular formula of $C_{13}H_{12}O_6P_2$, 326.18 g/mol: C 47.7%, H 3.7%. Actual: C 48.85%, H 4.16%.

3.2.7 4,4'-bis(ethylphosphono)biphenyl (Et₂H₂BPDP)

A sample of Et₂H₂BPDP was obtained from Benjamin Gelfand.[75] The preparation is described

as follows:

3.2.7.1 Synthesis of 4,4'-bis(diethylphosphono)biphenyl (Et$_2$H$_2$BPDP)

A stir bar and NiBr$_2$ (12.5177 g, 57.29 mmol) were activated in a 1L round-bottomed flask under vacuum by heating with a heat gun. The flask was cooled, exposed to argon atmosphere, and 4,4'-dibromobiphenyl (33.1027g, 106.10 mmol) was then added to the flask. The flask was equipped with a condenser and an addition funnel, to which diisopropyl benzene (150 mL) was added to the solution via the addition funnel and the flask was brought to reflux at 213°C. While under heat, a solution of diisopropyl benzene (36 mL) and triethyl phosphite (36mL, 209.94 mmol) was added to the addition funnel and added dropwise at a rate of one drop per three seconds, and allowed to reflux for 20 hours. Another solution of triethyl phosphite (36mL, 209.94 mmol) was added to the addition funnel and added dropwise (1drop/~5sec, adjusted as needed), and the reaction was continued for another 24 hours. The reaction mixture was removed from heat and then filtered twice on #2 filter paper. The solvent was then removed via short-neck distillation, heating up to 150°C. The sample was cooled, dissolved in acetone, and filtered in portions through a silica plug. Excess solvent was removed by rotary evaporator. The sample was then re-distilled, heating up to 170°C, yielding a brown oil. The brown oil was purified by stirring overnight in hexanes, yielding a brown solid. Further purification of the solid was conducted by dissolving it in chloroform and passing the solution through a silica plug, rinsing with acetone. This yielded a yellow solid, which was purified by stirring overnight in hexanes. A white, powdery solid (24.2869 g, 56.96 mmol, 53.7% yield) was collected.

3.2.7.2 Synthesis of 4,4'-bis(ethylphosphono) biphenyl (Et$_2$H$_2$BPDP)

       To a large acid digestion vessel, Et$_4$BPDP was added (1.0784 g, 2.53 mmol), followed by MeOH (10 mL) and then NH4OH (20%, 6 mL). The vessel was then sealed and heated in the oven at 120°C for 48 hours. The product was transferred to a round bottomed flask, rinsing with MeOH, and solvent was removed by rotary evaporator. The compound was then dissolved in H$_2$O and put through an ion exchange column (Na$^+$ form), which was eluted with pure water in 20 mL portions. The first five portions were combined, based on fluorescence, and the water was removed by rotary evaporator followed by heating under high vacuum. A white powdery solid was obtained (1.0755 g, 2.60 mmol, 103% yield). The high yield was most likely due to remaining water.

3.2.8 Crystallization of Co$_2$(Et$_2$BPDP)

       To a 20 mL glass vial, Et$_2$H$_2$BPDP (12.8 mg, 0.035 mmol) and ethylene glycol (2.0 mL) were added and sonicated for 5 minutes. A separate stock solution of Co(NO$_3$)$_2$ in water (0.15 M) was prepared. The stock solution (2.0 mL, 30 mmol) was then layered on top of the glycol and the vial was sealed. The vial was heated at 120°C for 48 hours with a 2 hour ramp up and a 12 hour cool down. Dark blue crystals were obtained. The crystal structure was solved by Jian-Bin Lin.[76]

3.2.9 Synthesis of 4,4'-biphenylbis(phosphonic acid) (H$_4$BPDP)

       A sample of H$_4$BPDP was obtained from Benjamin Gelfand.[75]

3.2.10 1,4-bis(isopropylphosphono)biphenyl (iPr₂H₂BDP)

A sample of pure iPr$_2$H$_2$BDP was obtained from Benjamin Gelfand.[75]

3.2.11 Synthesis of Co(H₂BPF), (CALF-B1)

Pink spheres were obtained through a reaction of Et$_2$H$_2$BPF and Co(NO$_3$)$_2$. Separate solutions of Et$_2$H$_2$BPF in ethylene glycol (0.022 M, 4.0 mL) and Co(NO$_3$)$_2$ in water (0.075 M, 3.0 mL) were prepared. The glycol solution was added to a 32 mL Teflon-lined acid digestion vessel. 95% Ethanol (1.0 mL) and the cobalt solution were then added on top of the glycol. The acid digestion vessel was then heated to 180°C for 48 hours. Product was filtered and rinsed with 95% EtOH, yielding a pink powder (macroscopically) and tiny pink spheres visible under an optical light microscope (19.1 mg, 0.05 mmol, 56.4%). The most uniform sample was obtained by heating the vessels at 180°C for 48 h, however spheres were also obtained with 24 h and 72 h runs at the same temperature. Analytical calculated based on the molecular formula of CoC$_{13}$H$_{12}$O$_6$P$_2$, 385.11: C 40.5%, H 3.14%. Actual: C 32.39%, H 1.75%. The discrepancy in values is likely due to a secondary phase with a greater concentration of cobalt.

3.2.12 Synthesis of Co(Et₂BPF), (CALF-B2)

Purple spheres were obtained through a reaction of Et$_2$H$_2$BPF and Co(NO$_3$)$_2$. A separate stock solution of Co(NO$_3$)$_2$ in water (0.15 M) was prepared. Et$_2$H$_2$BPF (13 mg, 0.034 mmol) was weighed out and placed in a glass vial, to which ethylene glycol (2.0 mL) was then added. Water (1.0 mL) and the cobalt solution (1.0 mL, 0.15 mmol) were then layered on top of the glycol. The glass vial was then heated to 120°C for 24 hours. Product was isolated by vacuum filtration, rinsing with 95% EtOH. A purple solid was obtained (4.4 mg, 0.01 mmol, 31.3%).

The most uniform sample was obtained by heating the vessels at 120°C for 24 h, however

spheres were also obtained with 48 h and 72 h runs at the same temperature. Analytical

calculated based on the molecular formula of $CoC_{17}H_{20}O_6P_2$, 413.16: C 43.6%, H 3.90%. Actual:

C 36.69%, H 2.36%. The discrepancy in values is likely due to a secondary phase in the

synthesis with a greater concentration of cobalt.

3.2.13 Trends in Synthesis of Spheres

A variety of reaction conditions similar to the two procedures listed above were

employed to test for conditions favouring formation of the hollow spheres. The procedures were

the same as those shown in either Section 3.2.11 for synthesis at 180°C or Section 3.2.12 for

syntheis at 120°C. The variables changed included the solvent, types and concentrations of

metals and ligands, as well as the heating time. The order of addition, reaction vessels and

generic method matches those described above. The critical experiments are shown in Table 3.1.

Spheres were initially characterized by optical microscope.

Table 3.1. Summary of varying conditions attempted for spheres synthesis, with results determined by visual approximation.

Expt No.	Metal	Amount (mmol)	Ligand	Amount (mmol)	Glycol	Amount (mL)	Water (mL)	Other Solvent	Amount (mL)	T (^{o}C)	Time (h)	Spheres (Y/N)
111-5	Co(NO$_3$)$_2$	0.30	Et$_2$H$_2$BPF	0.07	Ethylene	0.0	5.0			180	72	Y
113-1	Co(NO$_3$)$_2$	0.23	Et$_2$H$_2$BPF	0.06	Ethylene	3.0	3.0	EtOH	1.0	180	48	Y
113-2	Co(NO$_3$)$_2$	0.23	Et$_2$H$_2$BPF	0.06	Ethylene	3.0	3.0	EtOH	2.0	180	48	Y
113-3	Co(NO$_3$)$_2$	0.23	Et$_2$H$_2$BPF	0.06	Ethylene	3.0	3.0	MeOH	1.0	180	48	Y
113-4	Co(NO$_3$)$_2$	0.23	Et$_2$H$_2$BPF	0.06	Ethylene	3.0	3.0	MeOH	2.0	180	48	Y
113-5	CoCO$_3$	0.25	Et$_2$H$_2$BPF	0.06	Ethylene	3.0	4.0			180	48	Y
113B-1	Cu(NO$_3$)$_2$	0.30	Et$_2$H$_2$BPF	0.08	Ethylene	4.0	4.0			180	72	N
113B-2	Zn(NO$_3$)$_2$	0.32	Et$_2$H$_2$BPF	0.08	Ethylene	4.0	4.0			180	72	N
113B-3	Co(NO$_3$)$_2$	0.32	Et$_2$H$_2$BPF	0.08	Ethylene	8.0	0.0			180	72	N
113B-4	Co(NO$_3$)$_2$	0.33	Et$_2$H$_2$BPF	0.08	Ethylene	4.0	0.0	EtOH	4.0	180	72	N
113B-5	Co(NO$_3$)$_2$	0.31	Et$_2$H$_2$BPF	0.07	Ethylene	0.0	0.0	EtOH	4.0	180	72	N
114-1	Co(NO$_3$)$_2$	0.15	Et$_2$H$_2$BPF	0.04	Ethylene	2.0	2.0			120	24	Y
114-2	Co(NO$_3$)$_2$	0.45	Et$_2$H$_2$BPF	0.04	Ethylene	4.0	0.0			120	24	N
114-3	Co(NO$_3$)$_2$	0.41	Et$_2$H$_2$BPF	0.04	Ethylene	2.0	0.0	EtOH	2.0	120	24	N
114-4	Co(NO$_3$)$_2$	0.38	Et$_2$H$_2$BPF	0.04	Ethylene	2.0	0.0	MeOH	2.0	120	24	N
115-1	Co(NO$_3$)$_2$	0.77	PhPO$_3$H$_2$	0.10	Ethylene	4.0	4.0			180	72	N
115-2	Co(NO$_3$)$_2$	0.75	H$_4$BPDP	0.08	Ethylene	4.0	4.0			180	72	N
115-3	Co(NO$_3$)$_2$	0.77	None		Ethylene	4.0	4.0			180	72	N
115-4	None		Et$_2$H$_2$BPF	0.07	Ethylene	4.0	4.0			180	72	N
115-5	Co(NO$_3$)$_2$	0.75	Et$_2$H$_2$BPF	0.07	Ethylene	6.0	2.0			180	72	Y

Expt No.	Metal	Amount (mmol)	Ligand	Amount (mmol)	Glycol	Amount (mL)	Water (mL)	Other Solvent	Amount (mL)	T (^{o}C)	Time (h)	Spheres (Y/N)
116-1	$Co(NO_3)_2$	0.15	$PhPO_3H_2$	0.09	Ethylene	2.0	2.0			120	24	N
116-2	$Co(NO_3)_2$	0.15	$PhPO_3H_2$	0.09	1,2-Propylene	2.0	2.0			120	24	N
116-3	$Co(NO_3)_2$	0.15	$PhPO_3H_2$	0.09	1,3-Propylene	2.0	2.0			120	24	N
116-4	$Co(NO_3)_2$	0.15	H_4BPDP	0.04	Ethylene	2.0	2.0			120	24	N
116-5	$Co(NO_3)_2$	0.15	H_4BPDP	0.04	1,2-Propylene	2.0	2.0			120	24	N
116-6	$Co(NO_3)_2$	0.15	H_4BPDP	0.04	1,3-Propylene	2.0	2.0			120	24	N
116-7	$Co(NO_3)_2$	0.15	Et_2H_2BPF	0.03	Ethylene	2.0	2.0			120	24	Y
116-8	$Co(NO_3)_2$	0.15	Et_2H_2BPF	0.03	1,2-Propylene	2.0	2.0			120	24	Y
116-9	$Co(NO_3)_2$	0.15	Et_2H_2BPF	0.03	1,3-Propylene	2.0	2.0			120	24	Y
116-10	$Co(NO_3)_2$	0.15	Et_2H_2BPF	0.03	Ethylene	2.0	2.0			120	24	Y
116-11	$Co(NO_3)_2$	0.15	None		Ethylene	2.0	2.0			120	24	N
116-12	$Co(NO_3)_2$	0.15	Et_2H_2BPF	0.03	Ethylene	3.0	1.0			120	24	Y
116-13	$Co(NO_3)_2$	0.15	Et_2H_2BPF	0.03	1,2-Propylene	3.0	1.0			120	24	Y
116-14	$Co(NO_3)_2$	0.15	Et_2H_2BPF	0.03	1,3-Propylene	3.0	1.0			120	24	Y
116-15	$Co(NO_3)_2$	0.15	H_4BPDP	0.04	Ethylene	3.0	1.0			120	24	N
116-16	$Co(NO_3)_2$	0.15	H_4BPDP	0.04	1,2-Propylene	3.0	1.0			120	24	N
116-17	$Co(NO_3)_2$	0.15	H_4BPDP	0.04	1,3-Propylene	3.0	1.0			120	24	N
116-18	$Co(NO_3)_2$	0.15	Et_2H_2BPF	0.04	Ethylene	1.0	3.0			120	24	Y
116-19	$Co(NO_3)_2$	0.15	Et_2H_2BPF	0.04	1,2-Propylene	1.0	3.0			120	24	Y
116-20	$Co(NO_3)_2$	0.15	Et_2H_2BPF	0.03	1,3-Propylene	1.0	3.0			120	24	Y
116-21	$Co(NO_3)_2$	0.15	H_4BPDP	0.04	Ethylene	1.0	3.0			120	24	N
116-22	$Co(NO_3)_2$	0.15	H_4BPDP	0.05	1,2-Propylene	1.0	3.0			120	24	N
116-23	$Co(NO_3)_2$	0.15	H_4BPDP	0.04	1,3-Propylene	1.0	3.0			120	24	N
116-24	$Co(NO_3)_2$	0.15	$PhPO_3H_2$	0.10	Ethylene	3.0	1.0			120	24	N
116-25	$Co(NO_3)_2$	0.15	$PhPO_3H_2$	0.10	Ethylene	1.0	3.0			120	24	N
116-26	$Co(NO_3)_2$	0.15	$PhPO_3H_2$	0.31	Ethylene	2.0	2.0			120	24	N

Expt No.	Metal	Amount (mmol)	Ligand	Amount (mmol)	Glycol	Amount (mL)	Water (mL)	Other Solvent	Amount (mL)	T (^{o}C)	Time (h)	Spheres (Y/N)
116-27	$Co(NO_3)_2$	0.15	H_4BPDP	0.16	Ethylene	2.0	2.0			120	24	N
116-28	$Co(NO_3)_2$	0.15	H_4BPDP	0.16	1,2-Propylene	2.0	2.0			120	24	N
116-29	$Co(NO_3)_2$	0.15	H_4BPDP	0.16	1,3-Propylene	2.0	2.0			120	24	N
116-30	$Co(NO_3)_2$	0.15	Et_2H_2BPF	0.13	Ethylene	2.0	2.0			120	24	N
116-31	$Co(NO_3)_2$	0.15	Et_2H_2BPF	0.13	1,2-Propylene	2.0	2.0			120	24	Y
116-32	$Co(NO_3)_2$	0.15	Et_2H_2BPF	0.13	1,3-Propylene	2.0	2.0			120	24	Y
116-33	none		Et_2H_2BPF	0.03	Ethylene	2.0	2.0			120	24	N
120-1	$Co(NO_3)_2$	0.15	Et_2H_2BPF	0.04	Ethylene	2.0	2.0			120	48	Y
120-2	$Co(NO_3)_2$	0.15	Et_2H_2BPF	0.04	Ethylene	2.0	2.0			120	48	Y
120-3	$Co(NO_3)_2$	0.15	Et_2H_2BPF	0.04	Ethylene	2.0	2.0			120	48	Y
120-4	$Co(NO_3)_2$	0.15	Et_2H_2BPF	0.04	Ethylene	2.0	2.0			120	48	Y
120-5	$Co(NO_3)_2$	0.15	Et_2H_2BPF	0.04	Ethylene	2.0	2.0			120	48	Y
120-6	$Co(NO_3)_2$	0.15	Et_2H_2BPF	0.04	Ethylene	2.0	2.0			120	48	Y
120-7	$Co(NO_3)_2$	0.30	Et_2H_2BPF	0.08	Ethylene	4.0	4.0			120	48	Y
120-8	$Co(NO_3)_2$	0.30	Et_2H_2BPF	0.08	Ethylene	4.0	4.0			120	48	Y
120-9	$Co(NO_3)_2$	0.30	Et_2H_2BPF	0.08	Ethylene	4.0	4.0			120	48	Y
120-10	$Co(NO_3)_2$	0.30	Et_2H_2BPF	0.08	Ethylene	4.0	4.0			120	48	Y
120-11	$Co(NO_3)_2$	0.30	Et_2H_2BPF	0.08	Ethylene	4.0	4.0			120	48	Y
120-12	$Co(NO_3)_2$	0.30	Et_2H_2BPF	0.08	Ethylene	4.0	4.0			120	48	Y
120-13	$Co(NO_3)_2$	0.30	Et_2H_2BPF	0.08	Ethylene	4.0	4.0			120	48	Y
120-14	$Co(NO_3)_2$	0.15	Et_2H_2BPF	0.04	Ethylene	2.0	2.0			120	48	Y
120-15	$Co(NO_3)_2$	0.15	H_2-BDP-ip$_2$	0.04	Ethylene	2.0	2.0			120	48	N
120-16	$Co(NO_3)_2$	0.15	H_2-BDP-ip$_2$	0.04	Ethylene	2.0	2.0			120	48	N
120-17	$Co(NO_3)_2$	0.15	H_2-BPDP-Et$_2$	0.04	Ethylene	2.0	2.0			120	48	N
120-18	$Co(NO_3)_2$	0.15	H_2-BPDP-Et$_2$	0.04	Ethylene	2.0	2.0			120	48	N
130-1	$Co(NO_3)_2$	0.30	Et_2H_2BPF	0.03	Ethylene	2.0	2.0			120	72	N

Expt No.	Metal	Amount (mmol)	Ligand	Amount (mmol)	Glycol	Amount (mL)	Water (mL)	Other Solvent	Amount (mL)	T (^{o}C)	Time (h)	Spheres (Y/N)
130-2	Co(NO$_3$)$_2$	0.30	Et$_2$H$_2$BPF	0.03	1,3-Propylene	2.0	2.0			120	72	Y
130-3	Co(NO$_3$)$_2$	0.30	Et$_2$H$_2$BPF	0.05	Ethylene	3.0	2.0			120	72	Y
130-4	Co(NO$_3$)$_2$	0.30	Et$_2$H$_2$BPF	0.04	1,3-Propylene	3.0	2.0			120	72	Y
130-5	Co(NO$_3$)$_2$	0.22	Et$_2$H$_2$BPF	0.04	Ethylene	4.0	0.0			120	72	N
130-6	Co(NO$_3$)$_2$	0.17	Et$_2$H$_2$BPF	0.04	1,3-Propylene	4.0	0.0			120	72	N
130-7	Co(NO$_3$)$_2$	0.30	Et$_2$H$_2$BPF	0.13	Ethylene	2.0	2.0			120	72	Y
130-8	Co(NO$_3$)$_2$	0.30	Et$_2$H$_2$BPF	0.13	1,3-Propylene	2.0	2.0			120	72	N
130-9	Co(NO$_3$)$_2$	0.72	Et$_2$H$_2$BPF	0.13	Ethylene	4.0	0.0			120	72	N
130-10	Co(NO$_3$)$_2$	0.69	Et$_2$H$_2$BPF	0.13	1,3-Propylene	4.0	0.0			120	72	N
130-11	Co(NO$_3$)$_2$	0.30	Et$_2$H$_2$BPF	0.04	Ethylene	3.0	1.0			120	72	Y
130-12	Co(NO$_3$)$_2$	0.30	Et$_2$H$_2$BPF	0.04	1,3-Propylene	3.0	1.0			120	72	Y
131-1	Co(NO$_3$)$_2$	0.15	Et$_2$H$_2$BPF	0.04	Ethylene	2.0	2.0	Ethylene diamine	0.01	120	24	N
131-2	Co(NO$_3$)$_2$	0.15	Et$_2$H$_2$BPF	0.04	Ethylene	2.0	2.0	Ethylene diamine	0.02	120	24	N
131-3	Co(NO$_3$)$_2$	0.15	Et$_2$H$_2$BPF	0.04	Ethylene	2.0	2.0			120	24	Y
131-4	Co(NO$_3$)$_2$	0.15	Et$_2$H$_2$BPF	0.04	Ethylene	2.0	2.0			120	24	Y
131-5	Ni(NO$_3$)$_2$		Et$_2$H$_2$BPF	0.04	Ethylene	2.0	2.0			120	24	Y
131-6	Mn(NO$_3$)$_2$		Et$_2$H$_2$BPF	0.04	Ethylene	2.0	2.0			120	24	N
131-7	Fe(NO$_3$)$_2$		Et$_2$H$_2$BPF	0.04	Ethylene	2.0	2.0			120	24	N
131-8	Co(NO$_3$)$_2$	0.15	Et$_2$H$_2$BPF	0.04	Ethylene	2.0	2.0	Ethylene diamine	0.1	120	24	N
131-9	Ni(NO$_3$)$_2$		Et$_2$H$_2$BPF	0.04	Ethylene	2.0	2.0			120	24	Y
132-1	Co(NO$_3$)$_2$	0.30	Et$_2$H$_2$BPF	0.08	Ethylene	4.0	4.0			180	24	Y
132-2	Co(NO$_3$)$_2$	0.30	Et$_2$H$_2$BPF	0.07	Ethylene	4.0	4.0			180	24	Y
132-3	Co(NO$_3$)$_2$	0.30	Et$_2$H$_2$BPF	0.06	Ethylene	4.0	4.0			180	24	Y
132-4	Co(NO$_3$)$_2$	0.30	Et$_2$H$_2$BPF	0.07	Ethylene	4.0	4.0			180	24	Y

Expt No.	Metal	Amount (mmol)	Ligand	Amount (mmol)	Glycol	Amount (mL)	Water (mL)	Other Solvent	Amount (mL)	T (^{o}C)	Time (h)	Spheres (Y/N)
132-5	$Co(NO_3)_2$	0.30	Et_2H_2BPF	0.07	None		4.0	EtOH	4.0	180	24	Y
135-1	$Co(NO_3)_2$	0.15	Et_4BPF	0.04	Ethylene	2.0	2.0			120	24	N
135-2	$Co(NO_3)_2$	0.15	Et_2H_2BPF	0.04	Ethylene	2.0	2.0			120	24	Y
135-3	$Co(NO_3)_2$	0.15	H_4BPF	0.04	Ethylene	2.0	2.0			120	24	N
135-4	$Ni(NO_3)_2$	0.16	Et_2H_2BPF	0.03	Ethylene	2.0	2.0			120	24	Y
135-5	$Ni(NO_3)_2$	0.16	H_4BPF	0.04	Ethylene	2.0	2.0			120	24	N
135-6	$Ni(NO_3)_2$	0.16	H_4BPF	0.04	Ethylene	2.0	2.0			120	24	N
136-1	$Co(NO_3)_2$	0.30	Et_4BPF	0.08	Ethylene	4.0	4.0			180	24	Y
136-2	$Co(NO_3)_2$	0.30	Et_2H_2BPF	0.07	Ethylene	6.0	4.0			180	24	Y
136-3	$Co(NO_3)_2$	0.30	H_4BPF	0.08	Ethylene	4.0	4.0			180	24	Y
136-4	$Ni(NO_3)_2$	0.32	H_4BPF	0.08	Ethylene	4.0	4.0			180	24	Y
136-5	$Ni(NO_3)_2$	0.32	H_4BPF	0.08	Ethylene	4.0	4.0			180	24	Y

3.2.14 Reactions with CALF-B1 and CALF-B2

Samples of CALF-B1 and CALF-B2 were divided into vials and tested with different reagents for reactivity. A few drops of each reagent were placed on the sample, and changes in colour were monitored visibly via microscope. Reagents tested include water, 10% $HCl_{(aq)}$, 10% $NH_4OH_{(aq)}$, 1 M $NaOH_{(aq)}$, xylene, pyridine, and ethylenediamine.

3.2.15 Acid Digestion NMR Experiment

A sample of CALF-B2 was dissolved in 35% DCl in D_2O, yielding a blue solution with a white precipitate. In order to run NMR, oxidation of the cobalt in solution from cobalt (II) to cobalt (III) was necessary. Thus, a saturated solution of NaOH in D_2O was added drop wise until solution was basic. Separately, the white precipitate was collected and dissolved via drop wise addition of the NaOH/D_2O solution, then diluted in D_2O to yield a slightly cloudy yellow solution.

3.3 Results and Discussion

3.3.1 Effect of Temperature on Synthesis

Two different colours of spheres were observed, depending on the temperature of the solvothermal synthesis. The CALF-B1 synthesis resulted in pink, uniform hollow spheres, which were visible by optical microscope, shown in Figure 3.6. The CALF-B2 synthesis, on the other hand, resulted in purple, uniform hollow spheres.

96
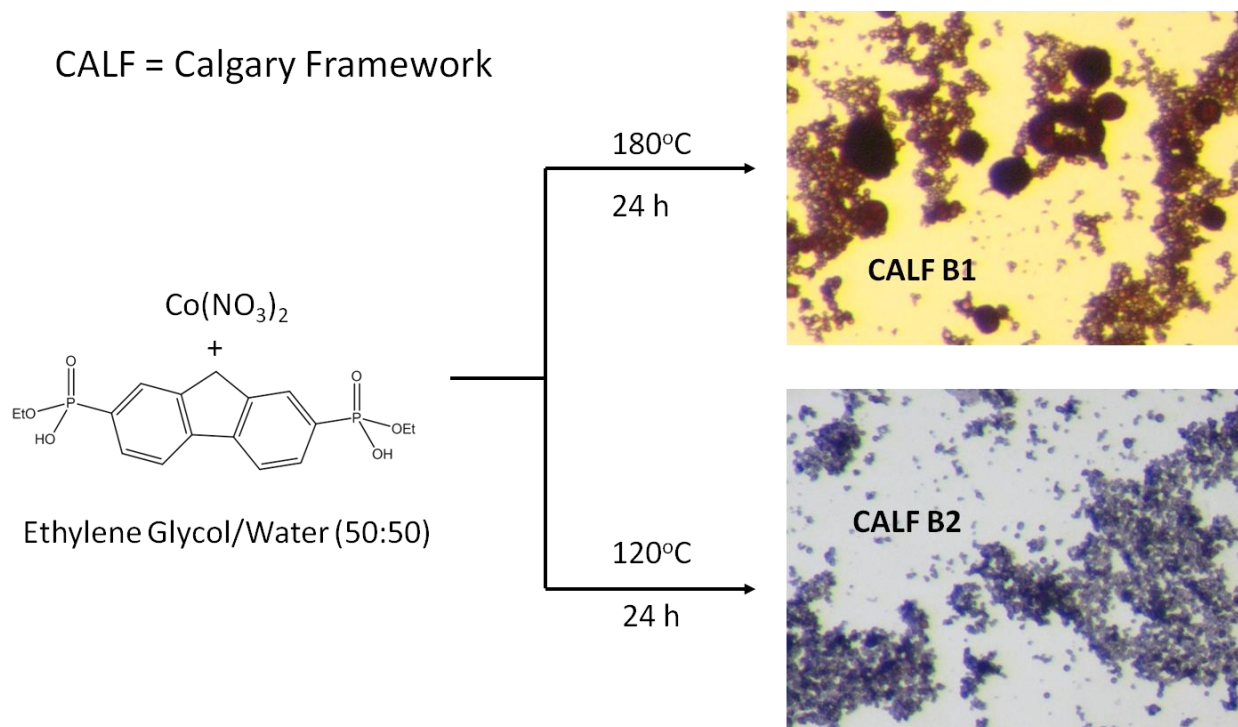
Figure 3.6. Reaction scheme and optical microscope images depicting differences between syntheses of CALF-B1 and CALF-B2.

The pink spheres, obtained with a higher temperature reaction, were hypothesized to be a more hydrated form of cobalt and involve a fully acidified phosphonate. The purple spheres, on the other hand, were believed to contain a monoester group on the ligand, as typical in-situ monoester removal does not occur until greater temperatures with phosphonates.[77] With respect to the difference in colour, we hypothesized that the purple spheres were less hydrated than the pink spheres. Upon heating CALF-B1 under vacuum at 100°C overnight, the colour changed from purple to pink, whereas CALF-B2 remained unchanged. This further augmented the hypothesis that the pink spheres have a greater amount of hydration in the cobalt coordination sphere. This is also supported by literature observations of the colours of crystalline cobalt (II) phosphonates which indicate that purple and pink complexes were indicative of an octahedral

coordination to the cobalt, while pink coloured phosphonates have a greater amount of hydration.[78–81] Rehydration was attempted by placing the spheres in a 90% RH stream (preparation description in section 2.2.10) for two days, however no further colour change occurred. Both CALF-B1 and CALF-B2 were stable to the high vacuum conditions required to dry the spheres for imaging with SEM.

3.3.2 Imaging

SEM images of CALF-B1, shown in Figure 3.7, demonstrate the diversity in size in a given sample. Spheres ranged from 1 to 25 µm in size, however the spheres that appeared hollow were found to be between 1 and 4 µm from two different samples. This indicates that the samples tested may have been a mixed phase, or possibly some spheres had developed larger shells. Images depicting hollowed cavities in the spheres were obtained by lightly crushing parts of the sample with the tip of a spatula. Close images of the larger (ca. 25 µm) spheres indicated that they were not all perfectly round, and crushed clumps of powder were also visible, likely pertaining to the larger particles.
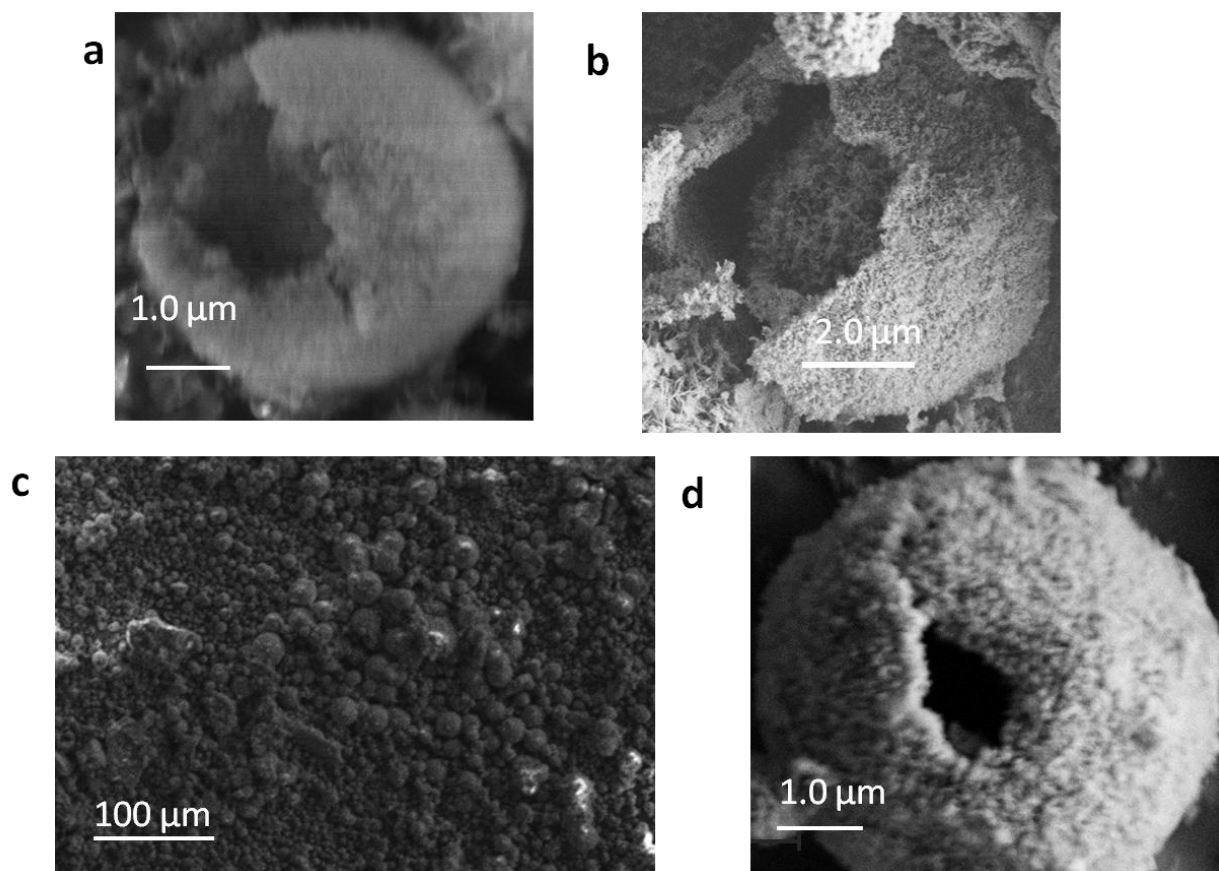
Figure 3.7. SEM images of CALF-B1 depicting hollow spheres.

In the case of CALF-B2, a true hollow sphere has yet to be found by SEM. Two separate samples were imaged, both from 48 h reactions. The first sample imaged, sample 120-12 from Table 3.1, was very diverse, both microscopically and under the SEM. Spheres, seen in Figure 3.8, appear to range in size from approximately 5 to 30 µm. The larger 30 µm spheres appeared to be a powder phase, as they did not transmit light under the optical microscope. Under the SEM, particles of crushed powder appeared irregular in shape. Sample 120-2 from Table 3.1 was also imaged using SEM. The image shown in Figure 3.9 (**c**) depicts a uniform sample with spheres that are 20 µm in size. These spheres were a transparent dark purple under the microscope, indicating they were not likely a powder. In reality, however, many of the spheres

in the sample appeared to be solid in the centre. These spheres were also much larger in size than the CALF-B2 obtained from 24 h syntheses, indicating that time could play a role in the sphere size.
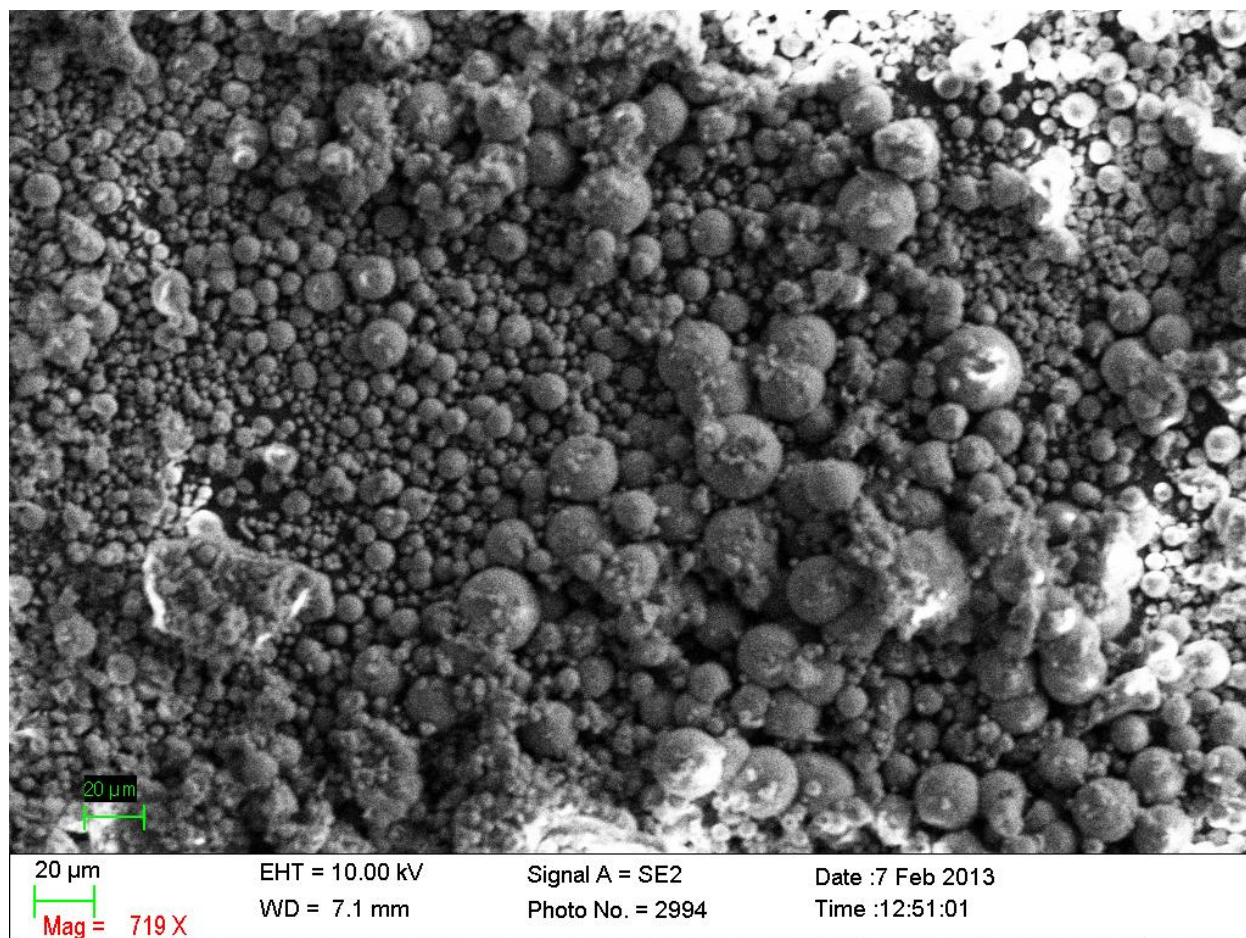
Figure 3.8. SEM image of CALF-B2 spheres obtained from synthesis 120-12.
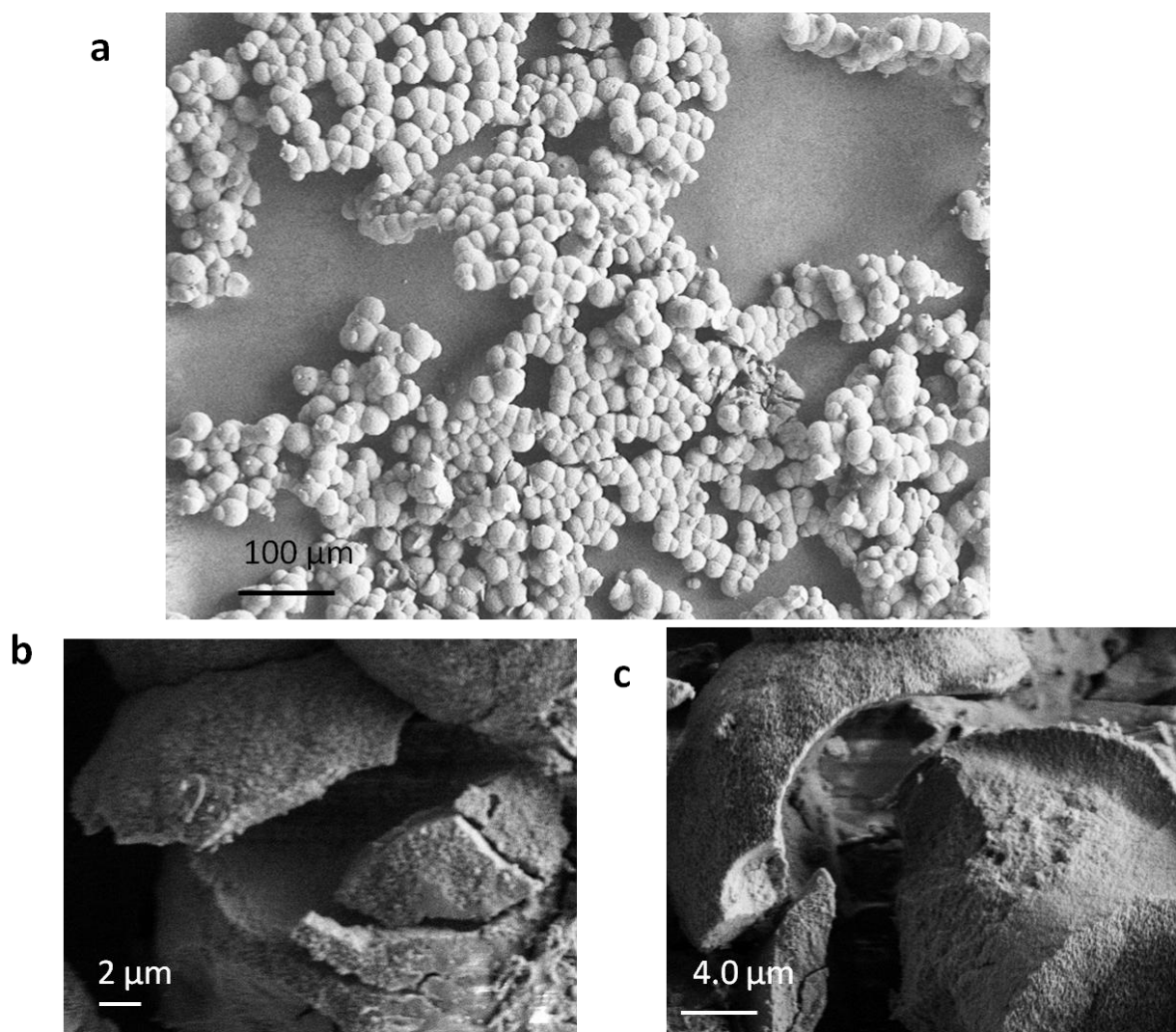
Figure 3.9. SEM images of CALF-B2 depicting solid spheres from synthesis 120-2.

3.3.3 Thermal Stability

CALF-B1 and CALF-B2 were examined by TGA for their thermal stability. The results, shown in Figure 3.10, indicate both to be thermally stable past 405 $^\text{o}$C. In the case of CALF-B1 there is an initial mass loss of 7.05%, which corresponds to the loss of 1.62 molecules of water per cobalt from the framework. A major source of mass loss that likely corresponds to the decomposition temperature occurs at 500$^\text{o}$C.
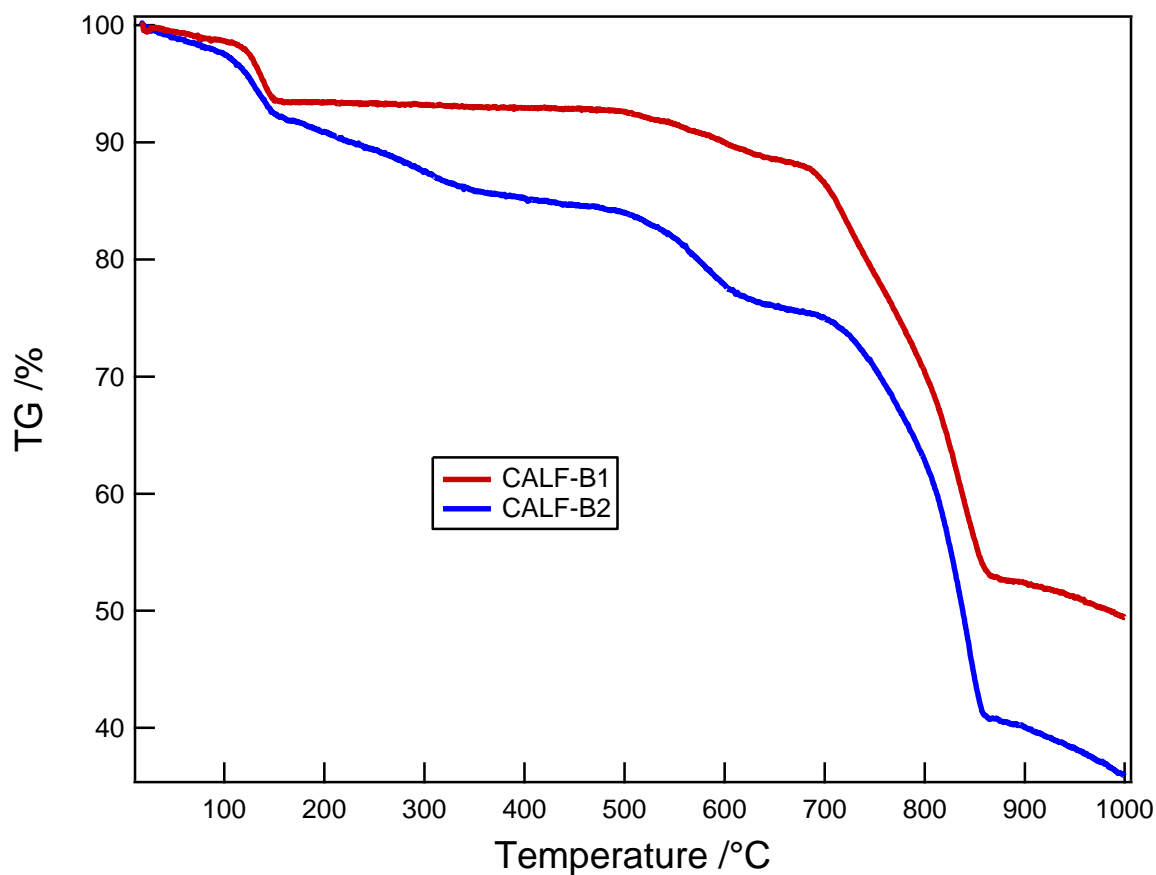
Figure 3.10. TGA traces of CALF-B1 and CALF-B2.

The overall mass loss of CALF-B2 occurs in two steps. The first step is a mass loss of 6.38%, which corresponds to a calculated 1.56 molecules of water per cobalt, calculated from the TGA based on a theoretical molecular weight of 413.16. The second mass loss of 8.29% can be attributed to the ester groups from the BPF ligand itself. The overall 15% mass loss up to 450°C indicates that CALF-B2 has a very high thermal stability. A major source of mass loss that likely corresponds to the decomposition temperature occurs at 500°C.

3.3.4 Crystallinity

PXRD powder patterns of all samples were indicative of amorphous materials. As can be seen in Figure 3.11, a small broad peak with a maximum at approximately 6° 2θ indicates there may be a small amount of crystallinity in each sample. It is difficult to conclusively attribute this peak to the spheres, due to the presence of powder impurities in each sample. Most importantly, this indicates that unlike MOF microspheres, which are highly crystalline, the CALF balls produced are not made up of nanocrystalline material. Hypothetically, it may be possible for the reported CALF balls to be ordered, however the large size of each sphere limits the ability to obtain a crystalline product. It is thus possible that the residual low angle broad peak corresponds to short-range order, such as a local ordering of Co-BPF.
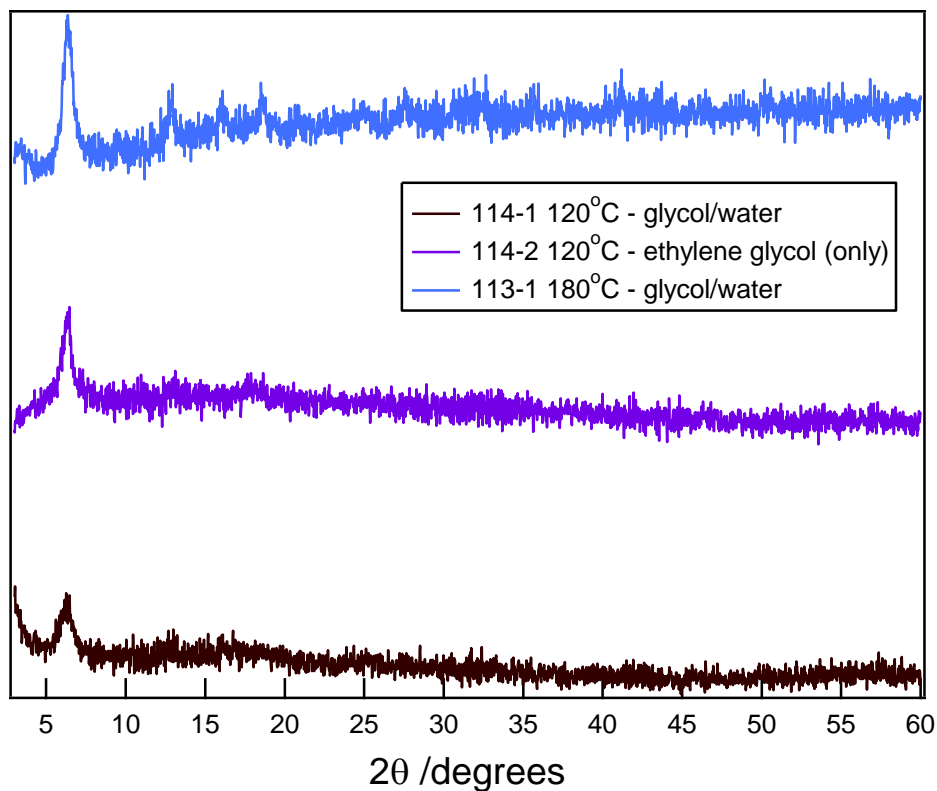
Figure 3.11. PXRD patterns of reaction products from 114-1, 114-2, and 113-1.

The angle of the ligand was crystallographically determined to be $162.20(1)^{o}$, based on a crystal structure obtained through the reaction of [Co(1,10-phenanthroline)$_2$](NO$_3$)$_{2(aq)}$ at 120°C in a water/methanol solution.[82]

3.3.5 Chemical Stability

A variety of chemical stability tests were conducted on the CALF balls. The results, summarized in Table 3.2, give important clues to the composition of the spheres. These results were obtained from visual observation under an optical microscope. Samples were observed for 10 minutes after the addition of each solvent, unless otherwise indicated.

As demonstrated by the above results, the spheres are extremely stable to water and ammonium hydroxide. Notably, when CALF-B2 was tested with ammonium hydroxide, a visible colour change from purple to blue in the powder phase indicated that a reaction occurred between the ammonium hydroxide and the powder. Remarkably, however, the spheres themselves are ammonium-stable. On the other hand, the spheres turned blue in the presence of sodium hydroxide. This corresponds to the coordination of the hydroxide ion to cobalt, which then changes colour to a yellow powder, indicative of the dissociation of the ligand and possible oxidation of cobalt.[83] In the presence of HCl acid, the spheres decompose immediately, releasing the ligand as a white, acid-insoluble precipitate. The blue colour that appears over time corresponds to the formation of the [CoCl$_4$]$^{2-}$ anion.[84]

Table 3.2. List of chemical stability tests conducted on spheres and results.

Reagent Added	CALF-B1 Results	CALF-B2 Results
Water	No change in appearance	No change in appearance
10% $HCl_{(aq)}$	White precipitate formed; blue solution appeared after 5 min	White precipitate formed; blue solution appeared after 5 min
1 M $NaOH_{(aq)}$	Turned clear blue; decomposed to a yellow powder after 5 minutes	Turned clear blue; decomposed to a yellow powder after 5 minutes
10% $NH_4OH_{(aq)}$	No change in appearance; Sample turned reddish-orange after 2 weeks, spheres appear to be intact	No change in appearance of spheres; powder phase in same sample turned blue; Sample turned reddish-orange after 2 weeks, spheres appear to be intact
Pyridine		No change in appearance
Water – sonication for 5 min	No change in appearance	No change in appearance
10% $NH_4OH_{(aq)}$ – sonication for 5 min	No change in appearance of spheres; slightly yellow solution	No change in appearance; slightly yellow solution
DMSO – sonication for 5 min		No change in appearance

With respect to time, the aforementioned colour changes occur very slowly, such that intermediate colours are visible. This indicates that there is a strong coordination between cobalt and the BPF ligand. Rather than dissociating immediately in acid, for example, the reaction between CALF-B and HCl takes approximately 30 seconds before a white precipitate is observed. The reaction with NaOH occurs in a similar fashion. Relative to the sodium hydroxide, the ammonium appears to react very slowly with the spheres. No change in colour was visible initially; however, over the course of two weeks, a colour change had occurred. The reddish-brown colour of the product suggests that an oxidation reaction takes place. This method may be a route to slow oxidation of the spheres.

3.3.6 Acid Digestion Experiment

The acid digestion of CALF-B2 confirmed the presence of the ligand and indicated the ligand remained a monoester upon reaction. A phosphorous NMR in D2O indicated the presence of three phosphorous peaks. Chemical shifts in ppm: $\delta 17.98, 13.62, 7.58$, which do not match the ligand ^{31}P NMR chemical shifts described in section 3.2.4. This discrepancy was primarily due to the use of D_2O as a solvent. A secondary reason for this is the fact that the solution was base-titrated to remove the cobalt, thus the ligand would no longer be in the form of an acid. Rough peak height ratios between the latter two peaks appear to match the monoester to full acid ratio from the impure monoester discussed in 3.2.4, however, integration in the digested sample is less accurate due to the large signal-to-noise ratio from the spectra. The presence of a small monoester peak is a good indication overall that there may be some unreacted ligand trapped in the spheres since the full ester cannot coordinate.

3.3.7 Role of the Solvent

Varying solvents were tested, the results of which are shown in Table 3.3. Results indicated that spheres synthesis was only possible with a combination of water with either a glycol or ethanol. When synthesis was attempted with only water or only glycol, a fine powder was the resulting product, as was the case of a 50:50 ethanol:ethylene glycol synthesis tested. The H_4BPF ligand is insoluble in water, while soluble in ethanol, methanol and glycols. Thus, this is an indication of potential solvent effects driving the synthesis of the CALF balls.

Table 3.3. A list of the different solvent combinations tested and their results. N/A indicates that the given solvent combination was not tested.

	H_2O	Ethylene Glycol	Ethanol	1,2-Propanediol	1,3-Propanediol
H_2O	Powder	Ethylene Glycol			
Ethylene Glycol	Spheres	Powder	Ethanol		
Ethanol	Spheres	Powder	N/A	1,2-Propanediol	
1,2-Propanediol	Spheres	N/A	N/A	Powder	1,3-Propanediol
1,3-Propanediol	Spheres	N/A	N/A	N/A	Powder

Different ratios of solvents to water were tested with all of the glycols at 120°C. In all cases, spheres were produced. Sizes of spheres were found to vary slightly with different glycols tested. The type of glycol used was found to influence the size of the spheres and the range of

sizes found in a sample. The use of ethylene glycol was found to promote more uniform sphere

formation, while both propane diols resulted in samples with larger sphere size variations.

Approximate sizes obtained are tiny (< 10 µm), small (ca. 10 µm), medium (20 µm, verified by

SEM), and large (ca. 40 µm). These sizes, however, are an approximation due to the limitations

of the optical microscope. Tiny spheres, notably, were barely visible. A change in the

glycol:water ratio from 1:1 to 3:1 or 1:3 lead to samples with visibly smaller spheres (< 10 µm)

in almost all cases. In the case of the ethanol:water reaction at 180°C, uniform CALF-B1

spheres were formed, but some powder was also present in the synthesis.

3.3.8 Dependence on Reaction Time

As mentioned previously, the reaction time was found to contribute to the size of the

spheres at 120°C, however, was not found to contribute to the size of the spheres at 180°C.

Reactions conducted for longer periods of time at 120°C resulted in larger spheres ($\geq$ 40 µm in

size), while more uniform samples were obtained from 24 h reactions. In the case of reaction

130-7, the reaction was attempted for 72 h with a larger concentration of reagents in solution.

The resulting spheres were approximately 80 µm in size, and were composed of two distinctly

coloured layers, as seen in the cross-section shown in Figure 3.12. As time progresses in the

reaction, it is evident that the spheres contain unreacted ligand which can nucleate to form a

thicker shell as well as a second inner phase. Although it is unclear which phase is contained in

each, it may be concentration-dependant, as the spheres made with the 4x concentration were the

only ones where this effect was obvious. Notably, the yolk-shelled sphere shown in Figure 3.12

is from a CALF-B1 synthesis and is shown to indicate the yolk-shelled morphology is possible

and has not been disproven in CALF-B2.
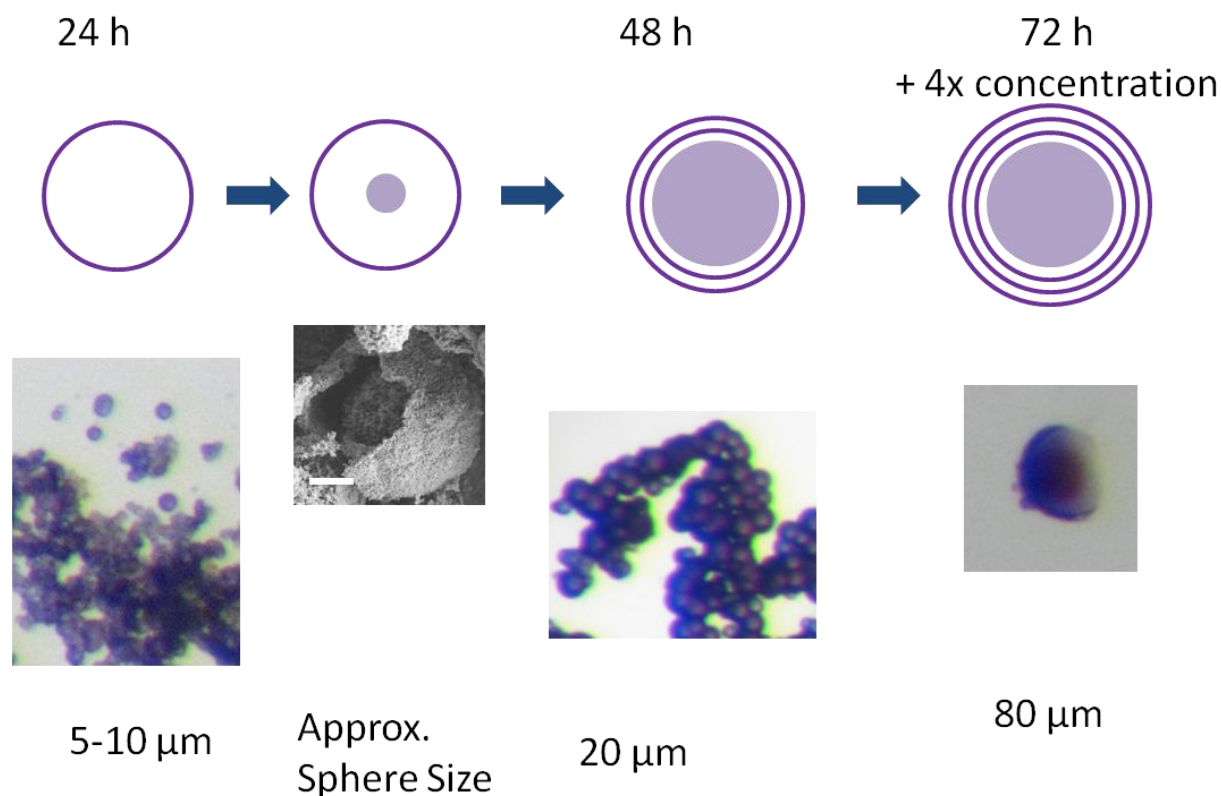
Figure 3.12. An illustration of the effect of increased time on the sphere size. Sizes were visually approximated, aside from the size of the 20 μm sample, which was verified by SEM.

3.3.9 Role of the Anion and Cation

Different metals were tested to determine the role of the metal in sphere formation. The results, summarized in Table 3.4, indicate that spheres could be formed using nickel(II). Nickel(II), similar to cobalt(II), favours an octahedral coordination.[85–88] Iron (II) could not be tested as it oxidizes readily in water, thus iron (III) was tested as an alternate. The coordination of the metal appears to play a crucial role, possibly directing the coordinated ligand and influencing the formation of spheres. In order to verify the overall structure was neutral, cobalt

(II) carbonate was tested in the synthesis of CALF-B1. A change in structure with changing

anion would indicate that the anion was present in the spheres. The resulting synthesis, however,

yielded spheres similar to those formed with cobalt (II) nitrate, which indicates that spheres form

independent of the anion present.

Table 3.4. Summary of results for reactions with Et$_2$H$_2$BPF and varying metals.

Metal Tested	Results
Cu(NO$_3$)$_2$	Green powder, multiple phases visible
Zn(NO$_3$)$_2$	White powder
Ni(NO$_3$)$_2$	Light green spheres
Mn(NO$_3$)$_2$	White powder
Fe(NO$_3$)$_3$	Orange gel and white powder phase

3.3.10 Role of the Ligand Shape

Four different phosphonate ligands were tested under the CALF-B2 synthetic conditions

in order to determine whether sphere formation is unique to a bent bis-phosphonate ligand. The

ligands tested, shown in Figure 3.13, were selected based on some similarity to the BPF.

Ligands (**9**) and (**10**) resulted in pink crystalline plates, while ligand (**12**) resulted in a minute

amount of a very fine light pink precipitate that could not be isolated. Ligand (**11**) resulted in

large, deep-blue, rectangular prismatic crystals. The solved crystal structure of Co$_2$(Et$_2$BPDP),

shown in Figure 3.14, has a tetrahedrally-coordinated cobalt centre attached to four different

ligands, which is a stark contrast in colour to the other samples obtained.
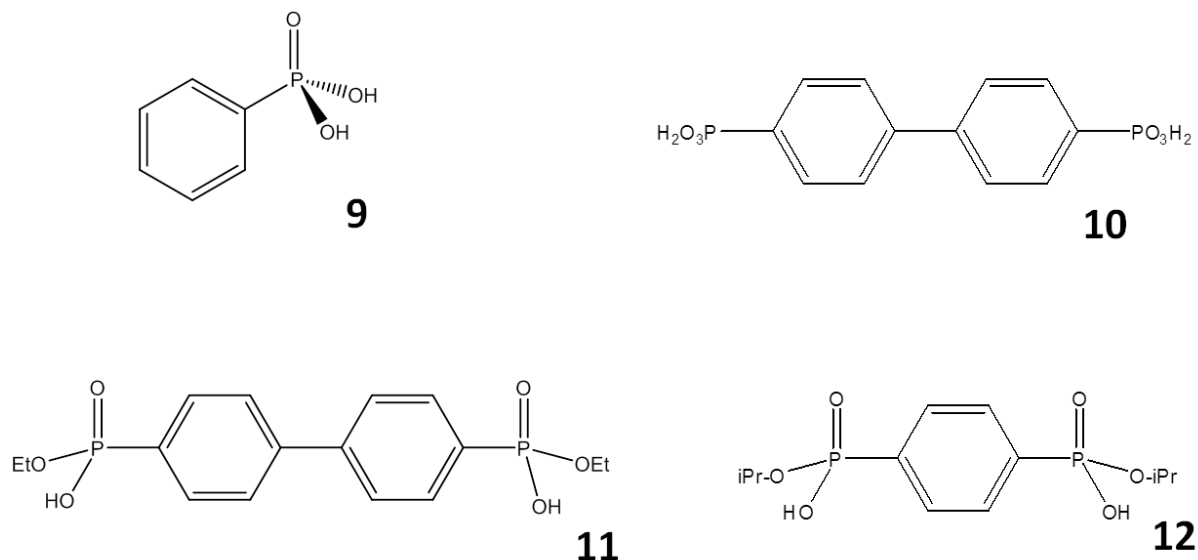
Figure 3.13. Structures of the different ligands tested for sphere formation. (9) PhPO₃H₂;

(10) H₄BPDP; (11) Et₂H₂BPDP; and (12) iPr₂H₂BDP.
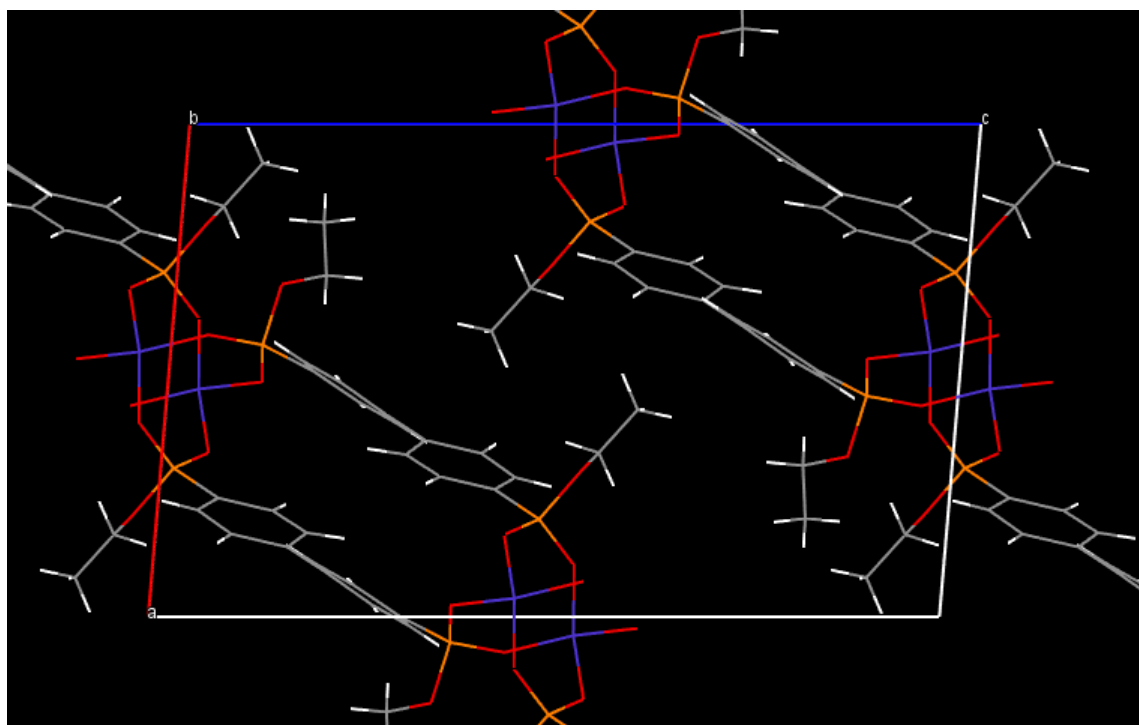
Figure 3.14. Crystal structure of $Co_2(Et_2BPDP)$. Co – blue, P – orange, O – red, C – grey, and H – white.

A comparison of PXRD patterns of the resulting materials, shown in Figure 3.15, demonstrates the difference in crystallinity between the obtained spheres and both the linear bisphosphonate ligands as well as phenylphosphonic acid. The powder patterns also demonstrate the difference in coordination between the blue $Co_2(Et_2BPDP)$ and the pink plates obtained with the two acid ligands, H_4BPDP and PhO_3H_2. The similarity between H4BPDP, PhO3H2 and CALF-B1 samples points toward a possible similarity between the short-range connectivity in the molecules.
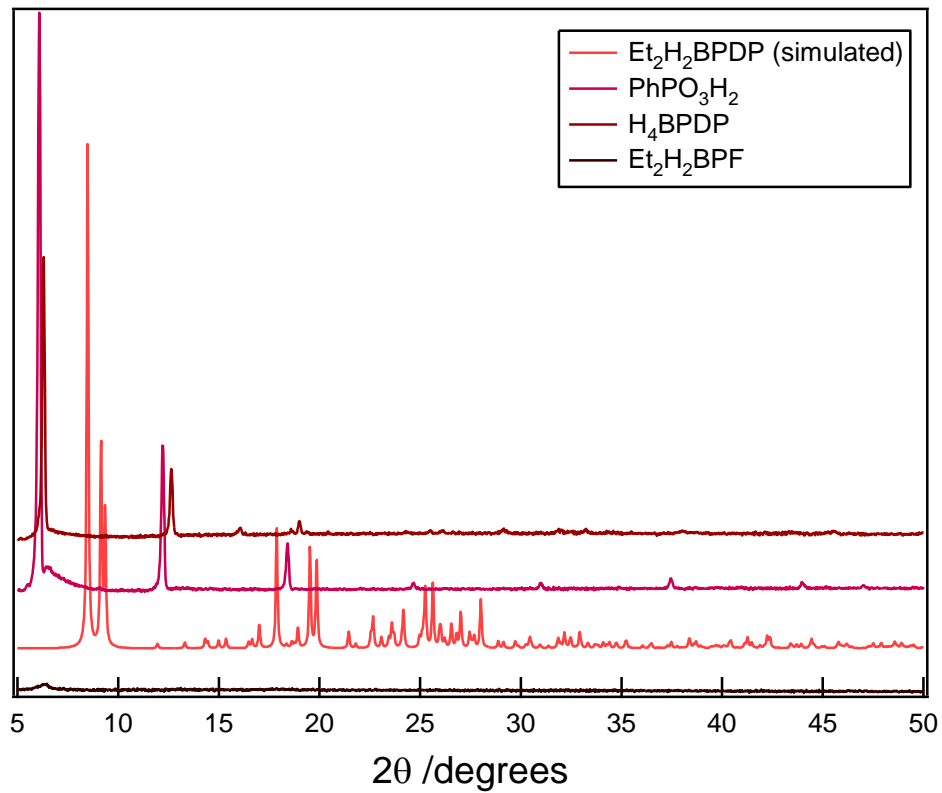
Figure 3.15. PXRD comparison of results with PhPO₃H₂, H₄BPDP, Et₂H₂BPDP, and Et₂H₂BPF.

3.3.11 Role of the Ester

Reactions with the full acid, monoester and diester forms of the fluorene were tested at both 120°C and 180°C. The results are summarized in Table 3.5.

Table 3.5. Comparison of reactivity of Et$_4$BPF, Et$_2$H$_2$BPF, and H$_4$BPF.

	120$^{\text{o}}$C	180$^{\text{o}}$C
Et$_4$BPF	Clear pink solution	Pink spheres
Et$_2$H$_2$BPF	Deep purple spheres	Pink spheres
H$_4$BPF	Light pink powder and solids	Pink spheres mixed with powder and crystallites

Firstly, the reactions with the full diester indicate that in-situ deesterification is only possible at 180$^{\text{o}}$C, based on the lack of a reaction at the lower temperature. Reactions with the monoester proceeded as predicted, with sphere formation at both 120$^{\text{o}}$C and 180$^{\text{o}}$C. The reactions with the full acid, however, resulted in drastically different results at the lower temperature. The pink powder formed by the acid is indicative of the importance of the ester towards the low-temperature reaction. The reaction at 180$^{\text{o}}$C is more reversible, thus the formation of spheres by the acid at this temperature indicates that the spheres are a thermodynamically favoured structure.

3.3.12 Mechanism of Formation

Comparing the results, it is clear that the solubility, shape and esterification of the ligand are all important factors in the formation of phosphonate hollow spheres. Based on the aforementioned results, it is theorized that formation of the spheres occurs due the hydrophobic nature of the phosphonic acid, which promotes the formation of cage-like morphologies in

solution. In the case of the CALF-B2 reaction at 120°C, the monoester is crucial to the sphere formation.

Chemically, the phosphonate monoester appears to aid in the orientation of the ligand to form spheres. This can be attributed to the ester group acting to shield the acid from the aqueous phase, as phosphonate esters are much more hydrophobic in nature. A second factor in the monoester reactivity is that it decreases the number of possible coordination modes in a phosphonate.[6] This could potentially create a favourable environment for certain metals to react more quickly, forming an initial layer. Once the initial layer is formed, it can potentially act as a nucleation site for further layer formation.

In the case of the acid, the formation of a pink powder with the 120°C synthesis indicates that a kinetic product is formed at 120°C, which is not spherical in nature. This is due to the stronger ligating ability of the acid, which causes it to react more rapidly in solution with more degrees of freedom in terms of coordination direction.

3.3.13 Comparison to MOF Microspheres and MOPs

There are clear differences between CALF balls and previously reported MOF spheres and cages. Firstly, the formation of CALF-B1 and CALF-B2 is driven by a unique mechanism that involves the use of a bent ligand, which is similar to the synthetic techniques used to form MOPs. Conversely, the CALF balls are much larger in scale than the MOPs demonstrated in literature. On top of this, the templating mechanism allows for a multilayer shell growth, as witnessed with 72 hour reactions, discussed in section 3.3.8.

Relative to MOF microspheres, the CALF balls produced are highly thermally stable. For example, the decomposition temperature of HKUST-1, used in two of the literature MOF

microspheres discussed, occurs at around 325°C, as demonstrated in the previous chapter. The other major advantage is the chemical and thermal stability of this material, which could be used to encapsulate reagents that would otherwise decompose a MOF sphere. The colour changes within these materials also pose a potential for the CALF-B materials to be used as sensors, or perhaps filled with a sensing agent that will augment the colour changes found in the cobalt-based materials.

3.4 Conclusions

The new phosphonate hollow spheres presented in this chapter demonstrate a new use of bisphosphonate ligands. Rather than forming a pillared-layered structure that is typical of linear bisphosphonates, the 2,7-bis(ethylphosphono)fluorene ligand resulted in the formation of homogeneous, hollow spherical structures. Although other examples of hollow MOF balls have been shown,[66–68] the work presented in this thesis is the first recorded example of hollow MOF balls made from phosphonate ligands. Unlike the examples reported in literature, the CALF balls presented demonstrate excellent chemical, thermal, and water stability.

The spheres are stable to sonication in both water and 10% ammonium hydroxide, and react slowly with 10% HCl and 10% NaOH, which are good properties for industrial applications. The stability in ammonium hydroxide could lead to oxidation of the spheres to increase the chemical stability.

The mechanism of formation of CALF-B1 and CALF-B2 are unique to the bent phosphonate ligand and was shown to not be successful with other linear phosphonate systems. It was determined that the esterification played a large role in directing the production of the spherical products at a reaction temperature of 120°C, which is indicative of a possible protection

by the ester group of the hydrophobic acid. Hollow spheres were formed independent of esterification at 180°C, which has lead us to conclude that the spheres are thermodynamically favourable due to the bent nature of the ligand. Assuming this mechanism is correct, this knowledge can be applied to other bent phosphonate systems in the future.

Overall, this work demonstrates that higher-ordered structures are possible using bisphosphonate ligands. It is also demonstrated that the shape of the bisphosphonate ligand can be used to control the structure in order to form higher-ordered materials.

3.5 Future Work

There are many possibilities with these materials that have yet to be explored. The most critical next step in this project is to test different bent bisphosphonic acids to determine the influence of the angle on the sphere size and sample crystallinity. It may be possible to use ligands with a deeper bend to produce smaller phosphonate clusters similar to MOPs, given careful solvent control is used.

One experiment that would be crucial to the development of phosphonate hollow spheres would be the synthesis of small, crystalline phosphonate polyhedra. A test of the ligand 1,3-bis(ethylphosphono)benzene. Assuming this ligand behaves similarly to 2,7-bis(ethylphosphono)fluorene, it may be possible to yield a structure similar to the MOP-1 with an appropriate solvent system.

References

1. M. Fujita, M. Tominaga, A. Hori, B. Therrien, *Accounts of chemical research* **38**, 369–378 (2005).

2. W.-Y. Sun, M. Yoshizawa, T. Kusukawa, M. Fujita, *Current Opinion in Chemical Biology* **6**, 757–764 (2002).

3. J. Bunzen *et al.*, *Angew. Chemie. Int. Ed.* **51**, 3161–3163 (2012).

4. M. Fujita, D. Oguro, M. Miyazawa, H. Oka, *Nature* **378**, 469 – 471 (1995).

5. P. D. C. Dietzel, R. Blom, H. Fjellvåg, *European Journal of Inorganic Chemistry* **2008**, 3624–3632 (2008).

6. J. M. Taylor, R. Vaidhyanathan, S. S. Iremonger, G. K. H. Shimizu, *J. Am. Chem. Soc* **134**, 14338–14340 (2012).

7. J. a. Hurd *et al.*, *Nature Chemistry* **1**, 705–710 (2009).

8. W. Gao *et al.*, *Chemical Comm.* **48**, 8898–8900 (2012).

9. N. L. Rosi *et al.*, *Science* **300**, 1127–1129 (2003).

10. Z. R. Herm, J. A. Swisher, B. Smit, R. Krishna, J. R. Long, *J. Am. Chem. Soc* **133**, 5664–5667 (2011).

11. A. P. Nelson, O. K. Farha, K. L. Mulfort, J. T. Hupp, *J. Am. Chem. Soc.* **131**, 458–460 (2009).

12. H. Furukawa *et al.*, *Science* **329**, 424–428 (2010).

13. R. F. Bruinsma *et al.*, *Nature* **427**, 523-527 (2004)

14. S. Kirumakki *et al.*, *Journal of Materials Chemistry* **19**, 2593 (2009).

15. K. J. Gagnon, H. P. Perry, A. Clearfield, *Chemical reviews* **112**, 1034–1054 (2012).

16. S. S. Chui, S. Lo, J. P. H. Charmant, A. G. Orpen, I. D. Williams, *Science* **283**, 1148–1150 (1999).

17. D. Feng *et al.*, *Angew. Chemie Int. Ed.* **51**, 10307–10310 (2012).

18. H. Jasuja, N. C. Burtch, Y.-G. Huang, Y. Cai, K. S. Walton, *Langmuir* **29**, 633–642 (2013).

19. H. Jasuja, Y. Huang, K. S. Walton, *Langmuir* **28**, 16874–16880 (2012).

20. J. J. Low *et al.*, *Journal of the American Chemical Society* **131**, 15834–15842 (2009).

21. J. M. Taylor, K. W. Dawson, G. K. H. Shimizu, *J. Am Chem. Soc.* **135**, 1193–1196 (2013).

22. P. Nugent *et al.*, *Nature* **101**, 1–5 (2013).

23. H. Deng *et al.*, *Science* **336**, 1018–1023 (2012).

24. A. Clearfield, in *Metal Phosphonate Chemistry: from Synthesis to Applications*, (2012), pp. 1–44.

25. R. Murugavel, S. Shanmugan, *Dalton Transactions* **2008**, 5358–5367 (2008).

26. R. Murugavel, M. G. Walawalkar, M. Dan, H. Roesky, C. Rao, *Acc. Chem. Res* **37**, 763–774 (2004).

27. J. M. Taylor, A. H. Mahmoudkhani, G. K. H. Shimizu, C. Framework, *Angew. Chimie Int. Ed.* **46**, 795–8 (2007).

28. R. Vaidhyanathan, A. H. Mahmoudkhani, G. K. H. Shimizu, *Canadian Journal of Chemistry* **253**, 247–253 (2009).

29. J. Zon, P. Garczarek, M. Bialek, in *Metal Phosphonate Chemistry: from Synthesis to Applications*, (2012), pp. 170–191.

30. A. U. Czaja, N. Trukhan, U. Müller, *Chem. Soc. Rev.* **38**, 1284–1293 (2009).

31. S. Kim, K. W. Dawson, B. S. Gelfand, J. M. Taylor, G. K. H. Shimizu, *J. Am. Chem. Soc* **135**, 963–6 (2013).

32. X. Kong *et al.*, *J. Am. Chem. Soc.* **134**, 14341–4 (2012).

33. D. M. D'Alessandro, B. Smit, J. R. Long, D. M. D'Alessandro, *Angewandte Chemie (International ed. in English)* **49**, 6058–6082 (2010).

34. P. Schoenecker, C. Carson, H. Jasuja, C. J. Flemming, K. S. Walton, *Industrial & Engineering Chemistry Research* **51**, 6513–6519 (2012).

35. K. a Cychosz, A. J. Matzger, *Langmuir* **26**, 17198–202 (2010).

36. A. Huang, N. Wang, C. Kong, J. Caro, *Angew. Chimie Int. Ed.* **51**, 10551–10555 (2012).

37. T. M. McDonald *et al.*, *J. Am. Chem. Soc.* **134**, 7056–7065 (2012).

38. T. K. Prasad, D. H. Hong, M. P. Suh, *Chem. Eur. J.* **16**, 14043–14050 (2010).

39. H. Fei, D. L. Rogow, S. R. J. Oliver, *J. Am. Chem. Soc.* **132**, 7202–7209 (2010).

40. S. Jae, J. Hyun, K. Suk, C. Rae, *International Journal of Hydrogen Energy* **35**, 13062–13067 (2010).

41. T. Uemura *et al.*, *Chemistry of Materials* **23**, 1736–1741 (2011).

42. K. Wan, Q. Liu, C. Zhang, *Materials Letters* **57**, 3839–3842 (2003).

43. S. R. Caskey, A. G. Wong-Foy, A. J. Matzger, *Journal of the American Chemical Society* **130**, 10870–108071 (2008).

44. J. a. Mason, K. Sumida, Z. R. Herm, R. Krishna, J. R. Long, *Energy Environ. Sci.* **4**, 3030–3040 (2011).

45. P. Küsgens *et al.*, *Microporous and Mesoporous Materials* **120**, 325–330 (2009).

46. Q. M. Wang *et al.*, *Microporous and Mesoporous Materials* **55**, 217–230 (2002).

47. P. D. C. Dietzel *et al.*, *Chem. Comm.* **46**, 4962–4 (2010).

48. K. Deakin, Unpublished Work.

49. Y. Wu *et al.*, *Angew. Chimie Int. Ed.* **47**, 8929–8932 (2008).

50. S. Lahsasni, M. Kouhila, M. Mahrouz, M. Fliyou, *Energy Conversion and Management* **44**, 923–936 (2003).

51. E. D. Bloch *et al.*, *Science* **335**, 1606–1010 (2012).

52. C. Corminbœuf, C. Corminb, J. Weber, *Chemical Physics Letters* **357**, 1–7 (2002).

53. J.-B. d'Espinose de la Caillerie, M. Kermarec, O. Clause, *The Journal of Physical Chemistry* **99**, 17273–17281 (1995).

54. G. Kowalczyk, J. E. Roberts, *Analytica Chimica Acta* **286**, 25–35 (1994).

55. A. J. Rossini *et al.*, *Chemical Science* **3**, 108 (2012).

56. K. Awazu, H. Kawazoe, *Journal of Applied Physics* **94**, 6243 (2003).

57. A. Soleimani Dorcheh, M. H. M. Abbasi, A. Soleimanidorcheh, A. S. Dorcheh, M. H. M. Abbasi, *Journal of Materials Processing Technology* **9**, 10–26 (2008).

58. S. Sutha, R. Yuvakkumar, V. Rajendran, R. Palanivelu, *Materials Letters* **90**, 68–71 (2013).

59. F. Rouquérol, J. Rouquérol, K. S. W. Sing, *Adsorption by powders and porous solids* (Academic Press, 1999), p. 467.

60. O. K. Farha *et al.*, *J. Am. Chem. Soc.* **134**, 15016–15021 (2012).

61. Y. He, N. a Seaton, *Langmuir* **22**, 1150–1155 (2006).

62. M. Eddaoudi *et al.*, *J. Am. Chem. Soc.* **123**, 4368–4369 (2001).

63. H. Furukawa, J. Kim, N. W. Ockwig, M. O'Keeffe, O. M. Yaghi, *J. Am. Chem. Soc.* **130**, 11650–11661 (2008).

64. J. Hu, M. Chen, X. Fang, L. Wu, *Chem. Soc. Rev.* **40**, 5472–5491 (2011).

65. X. Roy, J. Hui, M. Rabnawaz, *J. Am. Chem. Soc.* **133**, 8420–8423 (2011).

66. H. J. Lee, W. Cho, M. Oh, *Chem* **48**, 221–223 (2012).

67. R. Ameloot *et al.*, *Nature Chem.* **3**, 382–387 (2011).

68. A. Carné-Sánchez, I. Imaz, M. Cano-Sarabia, D. Maspoch, *Nature Chem.* **5**, 203–211 (2013).

69. L. Freedman, G. Doak, *Chemical Reviews* **57**, 479–523 (1957).

70. J. Le Bideau, C. Payen, P. Palvadeau, B. Bujoli, *Inorg. Chem.* **33**, 4885–4890 (1994).

71. K. Maeda, J. Akimoto, Y. Kiyozumi, F. Mizukarni, *J. Chem. Soc., Chem. Commun.* **1995**, 1033–1034 (1995).

72. K. Maeda, Y. Kiyozumi, F. Mizukami, *Angew. Chemie. Int. Ed.* **33**, 2335–2337 (1993).

73. B. G. Alberti, M. Casciola, U. Costantino, *Advanced Materials* **8**, 291–303 (1996).

74. M. Ghaemy, M. Barghamadi, *Journal of Applied Polymer Science* **114**, 3364–3471 (2009).

75. B. S. Gelfand, Unpublished Work.

76. J.-B. Lin, Unpublished Work.

77. T. Yamada, H. Kitagawa, *CrystEngComm* **14**, 4148–4152 (2012).

78. A. Distler *et al.*, *J. Chem. Soc., Dalton Trans.* , 1805–1812 (1999).

79. A. Turner *et al.*, *Dalton Trans.* **2003**, 1314–1319 (2003).

80. E. M. Bauer *et al.*, *Journal of Solid State Chemistry* **179**, 389–397 (2006).

81. R.-B. Fu *et al.*, *Polyhedron* **22**, 2739–2744 (2003).

82. M. E. Reid, Unpublished Work.

83. G. Svehla, *Vogel's Qualitative Inorganic Analysis* (ed. 7th, 1996), pp. 128–129.

84. O. O. R. Howell, *Journal of the Chemical Society (Resumed)* **1927**, 2039–2051 (1927).

85. C. Bellitto, E. M. Bauer, S. A. Ibrahim, M. R. Mahmoud, G. Righini, *Chem. Eur. J.* **9**, 1324–1331 (2003).

86. S. R. Miller *et al.*, *J. Am. Chem. Soc.* **130**, 15967–81 (2008).

87. P. O. Adelani, A. G. Oliver, T. E. Albrecht-Schmitt, *Inorg. Chem.* **51**, 4885–4887 (2012).

88. K. D. Demadis, N. Stavgianoudaki, in *Metal Phosphonate Chemistry: from Synthesis to Applications*, (2012), pp. 438–492.